TIME-DEPENDENT ENHANCED HEAT TRANSFER IN OSCILLATING PIPE FLOW

By

GUO-JIE ZHANG

A DISSERTATION PRESENTED TO THE GRADUATE SCHOOL OF
THE UNIVERSITY OF FLORIDA
IN PARTIAL FULFILLMENT OF THE REQUIREMENTS FOR THE
DEGREE OF DOCTOR OF PHILOSOPHY

UNIVERSITY OF FLORIDA

1988

To my beloved motherland

ACKNOWLEDGEMENTS

TABLE OF CONTENTS

iv

LIST OF FIGURES

LIST OF TABLES

KEY TO SYMBOLS

x	x coordinate
r	radial coordinate
t	time
ξ	coordinate (x) in transformed plane
η	coordinate (r) in transformed plane
τ	transformed time
L	pipe length
R_1	pipe inner radius
R_2	pipe outer radius
ω	oscillating frequency
δ	boundary layer thickness
P	pressure
ρ	density
c	specific heat
ν	Kinematic viscosity
μ	dynamic viscosity
κ	thermal diffusivity
k	thermal conductivity
K_e	coefficient of enhanced heat diffusivity
Pr	Prandtl number
$A = 1/\rho \, |\partial p/\partial x|$	a measure of the maximum axial pressure gradient (cm/sec^2)

α	Wormersley number $\alpha = \sqrt{\omega/\nu}$
T	Temperature
γ	$\gamma = \partial T/\partial x$ time-averaged axial temperature gradient
ζ	$\zeta = r/R_1$ dimensionless radial distance
g	radial temperature distribution function
U	velocity
U_O	representative velocity
f	velocity shape function
χ	Lagrangian displacement
DX	dimensionless tidal displacement
Δx	dimensional tidal displacement
Q_{total}	time averaged total enhanced axial heat flow over pipe cross-section
ϕ	axial heat flux

Subscript

f	fluid
w	wall
h	hot
c	cold
th	thermal
eq	equivalent
adj	adjacent

Abstract of Dissertation Presented to the Graduate School
of the University of Florida in Partial Fulfillment of the
Requirements for the Degree of Doctor of Philosophy

TIME-DEPENDENT ENHANCED HEAT TRANSFER
IN OSCILLATING PIPE FLOW

By

Guo-jie Zhang

April 1988

Chairman: Ulrich H. Kurzweg
Major Department: Aerospace Engineering, Mechanics,
                 and Engineering Science

The problem of time-dependent enhanced heat transfer
in an incompressible viscous laminar fluid subjected to
sinusoidal oscillations in circular pipes which are
connected to a hot reservoir at one end and a cold reservoir
at the other end has been examined numerically in detail.
Three models were designed for the investigation of such an
enhanced thermal pumping process and a computer code (ETP)
was developed to implement all the numerical calculations.

To increase the understanding of the mechanism of
thermal pumping, the periodic velocity profiles and
Lagrangian displacements as well as tidal displacements at
various Wormersley numbers (from α = 0.1 to 1000) were
studied. Some transient problems of enhanced axial heat
transfer in oscillating pipe flow such as the periodic final
temperature build-up process in oscillating pipe flow were
also examined. The time-dependent temperature distribution

in the different models was numerically studied in detail. The enhanced axial heat flux magnitude versus different tidal displacements with water and mercury as the working fluids bounded by pipe walls of different material were observed and the quadratic coefficients found. The influence of the variation of water properties on the enhanced axial heat flux was numerically examined and the results show that the enhanced axial heat flux can vary about 150 percent even within the temperature range from 0°C to 100°C. The effects of wall thickness and pipe diameter in enhanced thermal pumping were also studied and the optimum wall thickness was found to be about 20 percent of the pipe radius in the water-glass combination. The tuning effect in the water-steel and the mercury-steel cases was examined and the results show good agreement with analytic predictions. A comparison of the enhanced axial heat flux with the axial heat flow due to heat conduction at various tidal displacement and Wormersley numbers shows that the latter is quite small and negligible provided the tuning condition is satisfied.

This study has shown that the enhanced thermal pump is indeed a very effective tool for those problems where large amounts of heat must be transported without an accompanying convective mass exchange. The investigation also indicates that turbulent flow in the reservoirs is preferable to laminar conditions and should receive more attention in future studies.

CHAPTER I
INTRODUCTION

Enhanced heat transport in a viscous laminar fluid subjected to sinusoidal oscillations in a very long pipe which connects a hot fluid reservoir at one end and a cold fluid reservoir at the other end (Fig. 2-1) has been recognized and studied recently by Kurzweg [15, 16, 17, 22]. The results obtained show that with this oscillatory pipe flow the heat transferred axially from the hot end to the cold end can be orders of magnitude larger than that obtained by pure molecular conduction in the absence of oscillations. In addition, the more important thing of interest is that this heat transfer process involves no net convective mass transport. Major assumptions made in the above cited studies on enhanced heat diffusion are that a constant time-averaged non-zero axial temperature gradient is always present in the oscillating flow and that the axial molecular conduction along the wall and in the oscillating fluid is negligible.

Discovery of this enhanced heat transport phenomenon was made possible by earlier studies on axial dispersion of contaminants within steady laminar flows through capillary tubes by Taylor in 1953 [32], and Aris in 1956 [4]. These

1

earlier studies show that when a small quantity of a contaminant is introduced into a circular pipe, the dispersion of the resultant contaminant cloud is greatly enhanced by the flow of the fluid. Bowden's 1965 results show that similar dispersion effects occur in oscillatory flow [8]. This enhanced axial dispersion of contaminants in the presence of laminar oscillatory flow within capillary tubes was studied in 1975 by Chatwin who suggested that the assumption of constant time-averaged axial contaminant gradient can be made [10]. Recently, Bohn et al. extended this work to the study of gas component transfer in binary gas mixtures when these are confined to single tubes and a sinusoidal pressure variation is applied [7]. Further studies in 1983 by Watson [38] show that the effective diffusion of contaminants is proportional to the square of the tidal displacement. This has been experimentally verified by Joshi et al. [13] and by Jaeger [12], both in 1983, and most recently by Kurzweg and Jaeger [19], in 1987. All these results show that the contaminant would spread axially in both steady and oscillatory laminar pipe flow at rates as much as five orders of magnitude higher than in the absence of fluid motion.

The first significant research work extending these enhanced axially diffusion studies to the heat transfer problem in oscillatory flow within very slender pipes or flat plate channels is due to Kurzweg [15, 16, 22]. In

early 1983 Kurzweg suggested that a similar dispersion process should occur in the heat transfer area because of the similarity in both the governing diffusion and heat transfer equations [16], and the first preliminary theory was formulated in 1985 [15, 16], in which, referring to Chatwin's idea, a time averaged constant axial temperature gradient assumption was used. The instantaneous temperature distribution was taken to be of the form [15, 22].

$$T = \gamma[x + R_1 \, g(\varsigma) e^{i\omega t}] \qquad (1-1)$$

where $\gamma = \partial T/\partial x$ is the time-averaged axial temperature gradient, R_1 is the tube radius, x is the axial distance along the capillaries (with $x = L/2$ and $x = -L/2$ denoting the ends), L is the pipe length under consideration, ω is the oscillating frequency of fluid, $g(\varsigma)$ is a radial temperature distribution, and $\varsigma = r/R_1$ is the dimensionless radial distance. The theoretical analysis shows that under certain conditions such enhanced axial heat diffusivity can indeed be significantly larger than the axial molecular conduction [15, 16] and this has been verified by some experimental measurements by Kurzweg and Zhao [22].

In order to better understand the physical mechanisms of this interesting and potentially useful heat transfer technique, we shall examine in greater detail the thermal pumping model shown in Fig. 2-1. It is assumed that a bundle of very thin and long tubes is connected to a

4

reservoir which supplies unlimited hot liquid at one end to a second reservoir which supplies unlimited cold liquid at the other end. The liquid in the pipes is oscillating axially with an amplitude such that none of the liquid which is originally in the middle portion of pipes ever runs into either reservoir. That is, there is no net convective mass exchange between two reservoirs. The largest axial fluid dimensionless displacement (when cross-section averaged) is referred to as the nondimensional tidal displacement and is denoted by "ΔX" (it should not be confused with the dimensional tidal displacement "Δx" frequently used in the present study). At time t = 0, the fluid within the pipes is set into axial oscillations at angular frequency ω and tidal displacement Δx. After a short transient, this oscillatory motion will lead to very large axial heat flows which can be readily made to exceed those possible with heat pipes.

Before exploring the mechanisms of this enhanced heat transport, it is necessary to introduce some new concepts which are commonly used in the study of this type of oscillatory motion.

As is well known [36], for high frequency viscous laminar axial oscillations within fluid flow along rigid pipes, the non-slip boundary condition creates a very thin Stokes' viscous boundary layer of thickness

$$\delta = \sqrt{2\nu/\omega} \qquad (1-2)$$

where ν is the fluid kinematic viscosity. For room temperature water at a frequency of 10 Hz, this viscous boundary layer is approximately $1.7 \cdot 10^{-2}$ cm. The corresponding thermal boundary layer thickness is about

$$\delta_{th} = \delta/\sqrt{Pr} \tag{1-3}$$

where Pr is the Prandtl number. Note that both δ and δ_{th} decrease in thickness as the oscillating frequency ω increases.

In the theoretical analysis, it is always assumed that a fully developed velocity profile of the oscillating flow exists within the pipes. At high frequency ω, this flow consists essentially of a slug flow over most of the fluid core bounded by a thin boundary layer of width δ as discussed by Uchida [36]. Neglecting end effects, the fully developed oscillating laminar velocity profile in pipes, due to a periodic axial pressure gradient, is found to be [19]

$$U(\varsigma,t) = U_0 f(\varsigma) e^{i\omega t} \tag{1-4}$$

where U_0 is a representative velocity, $\varsigma = r/R_1$ is again the dimensionless radial distance, $f(\varsigma)$ the velocity shape function, and ω the angular velocity of the oscillatory flow. The explicit form of $f(\varsigma)$ is

$$f(\varsigma) = \frac{-i\Lambda}{\alpha^2} \left(1 - \frac{J_0(\sqrt{-i\alpha\varsigma})}{J_0(\sqrt{-i\alpha})} \right) \tag{1-5}$$

where $\Lambda = R_1^2 |\partial p/\partial x|/\rho \nu U_O$ is the nondimensional pressure gradient maximum acting along the capillaries, $\alpha = R_1\sqrt{\omega/\nu}$ is the Wormersley number measuring the ratio of inertia to viscous forces, ν is the fluid kinematic viscosity of the carrier liquid, and ρ is the fluid density. This velocity profile will reduce to the familiar Poiseuille parabolic shape as the angular frequency ω becomes small, while at moderate frequency, $f(\zeta)$ has the shape demonstrated by Uchida [36].

Another new term commonly used when dealing with oscillating flow is the cross-stream averaged dimensionless tidal displacement ΔX which can be mathematically defined as

$$\Delta X = \frac{4U_O}{\omega} \left| \int_0^1 \zeta f(\zeta) d\zeta \right| \qquad (1-6)$$

and on integration, yields [18]

$$\Delta X = \frac{|\partial p/\partial x|}{1/2 \ \rho\omega^2} \left| 1 + \frac{2}{\alpha} F(\alpha) \right| \qquad (1-7)$$

where the complex function $F(\alpha)$ has the form

$$F(\alpha) = i \ \frac{J_O'(\sqrt{-i\alpha})}{J_O(\sqrt{-i\alpha})}$$

with the prime denoting differentiation. Using the definition of Kelvin function: $J_O(\sqrt{-i\alpha}) = \text{ber } \alpha + i \text{ bei } \alpha$

α	$F(\alpha)$
1	$-0.4899 + i\ 0.06076$
2	$-0.7738 + i\ 0.3449$
3	$-0.7485 + i\ 0.5399$
4	$-0.7141 + i\ 0.5842$
5	$-0.7101 + i\ 0.6040$

$F_I(\alpha)$

$F_R(\alpha)$

$\alpha = a\sqrt{\omega/\nu}$
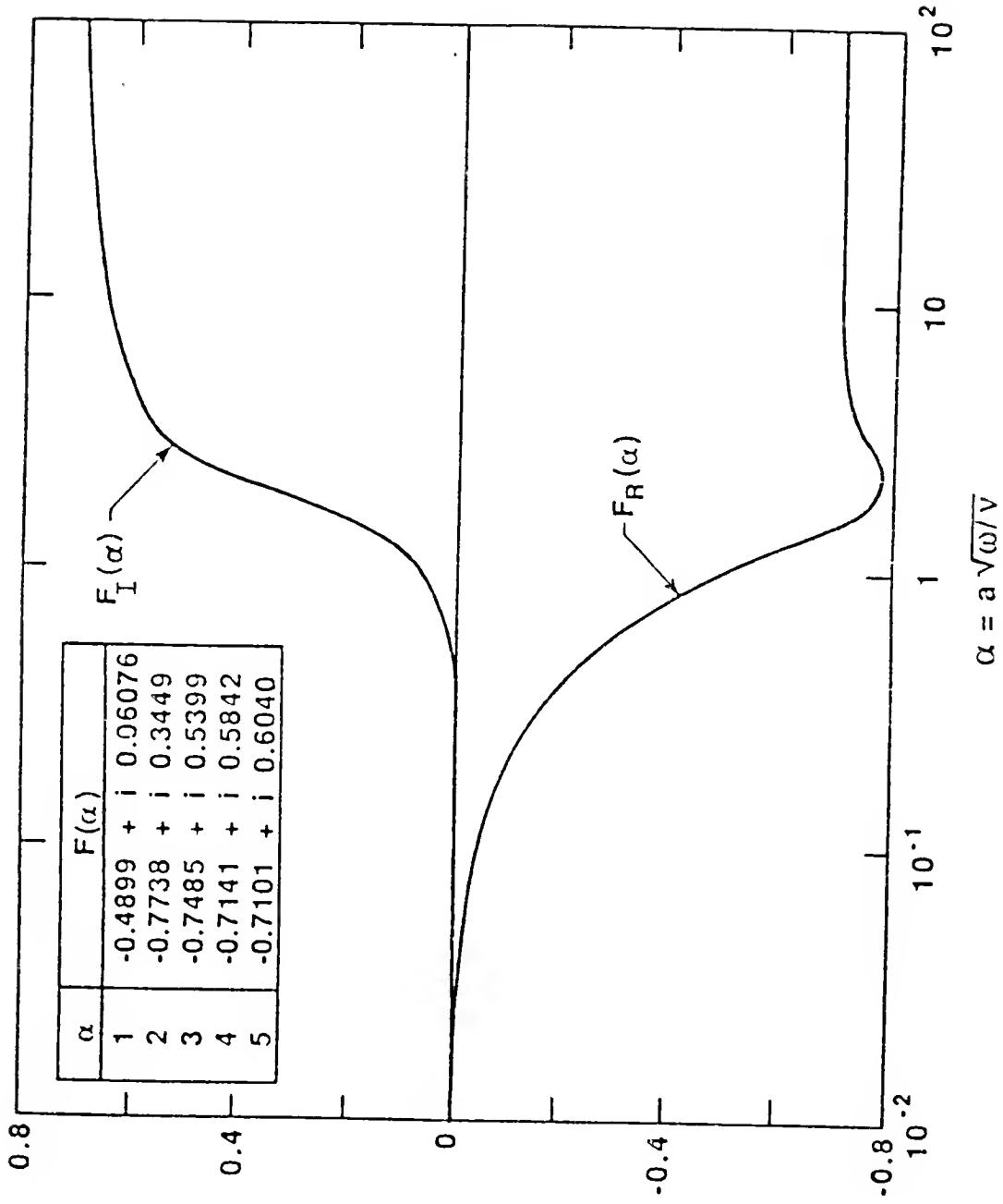
Fig 1-1   F(α) Curve [18]

[1], the complex function F(α) (Fig. 1-1) can be further written as:

$$F(\alpha) = F_r(\alpha) + i\ F_i(\alpha) = i\left(\frac{ber'\alpha + i\ bei'\alpha}{ber\ \alpha + i\ bei\ \alpha}\right) \quad (1-8)$$

This dimensionless tidal displacement is related to the maximum of the periodic pressure gradient via [18]

$$\Delta X = \frac{|\partial p/\partial x|}{1/2\ \rho\omega^2} \begin{cases} \frac{1}{8}\ \alpha^2 & \alpha \ll 1 \\ 1 - \frac{\sqrt{2}}{\alpha} & \alpha \gg 1 \end{cases} \quad (1-9)$$

Apparently, for any fixed tidal displacement Δx and oscillating frequency ω, the axial pressure gradient required is proportional to the inverse square of the Wormersley number when α is small; however, it is independent of α when α is very large. This also implies that the exciting axial pressure gradient $|\partial p/\partial x|$ is approximately proportional to the fluid kinematic viscosity ν and inversely proportional to the square of the pipe radius R_1 when Wormersley number is very small (it happens only at low ω, small R_1, and large ν, for example, oil), while it is almost independent of the fluid kinematic viscosity and the pipe radius when the Wormersley is very large (it happens only at very large R_1, high ω, small ν,

for instance, a liquid metal). Note, if the tidal displacement ΔX is fixed, while allowing the oscillating frequency to change, the axial pressure gradient $|\partial p/\partial x|$ can become very large when the oscillating frequency becomes large. This is mainly due to inertial effects and not so much due to viscous drag forces which dominate the oscillatory flow at small Wormersley number.

With the definition of the above quantities, we are now in a position to explore the details of the enhanced axial heat transfer in oscillatory flow within pipes. It is assumed that a constant temperature gradient exists along the pipe in the axial direction and that a very large time-dependent radial temperature gradient variation is superimposed. When the fluid moves towards the cooler side (we term this the positive stroke), the hotter fluid within the pipe core which is initially brought into the pipe from the hot reservoir produces a large radial heat flow via conduction to the cooler portions of the fluid within the Stokes' boundary layer and to the cooler pipe wall; while during the negative (or reverse) stroke, i.e., when the fluid moves towards the hotter side, the higher temperature in the boundary layer and the pipe wall conducts the heat back into the cooler fluid core. This coupled radial heat conduction with an axial convective transport leads to an enhanced axial heat flux along the entire length of the pipes.

Further, from the system point of view, the heated fluid near the cold reservoir will eventually be ejected into the cold reservoir and mixed there with the lower temperature liquid. Contrarily, near the hot reservoir side the fluid within the pipes which has been cooled during each positive stroke is pushed out into the hot reservoir and mixes with the higher temperature liquid. This process of thermal pumping is what leads to a time-averaged heat flow from the hot reservoir into the cold reservoir. It differs essentially from the working principle of a normal pump. For a normal pump one can draw the analogy with transport of a one-way vehicle which transports passengers as well as the carrier from one point to another. For the thermal pump one can draw the analogy with a two-way busline which periodically loads and unloads the passengers (heat) from the hot reservoir to the cold reservoir, heat can be continually transferred, and the carrier, in the time-averaged sense, does not move. This property is particularly important for those systems where a large amount of heat transfer is needed while the working fluid is required to remain in the system (as in nuclear reactors). Note that the axial heat conduction, in general, is assumed to be very small in this thermal pumping process compared with the enhanced axial heat flow [16].

Apparently, the heat transport rate in thermal pumping is governed by both the thermal properties of the

working medium and pipe wall and the characteristics of the oscillatory motion of the fluid. The enhanced axial heat flow does increase with increasing oscillating frequency as this thins out the boundary layer and leads to an accompanying increase in the radial temperature gradient. This observation holds only as long as the thermal properties of the liquid and the wall are compatible. If the molecular conduction of the fluid in the radial direction is very small, then even high frequency oscillatory motion will not produce a large increase in the rate of enhanced axial heat flow. This is because such a system fails to supply the "passengers" enough time to be loaded onto the "bus" and to be unloaded from the "bus". Obviously, the system just wastes energy. On the other hand, if the molecular conduction of the fluid in the radial direction is very large, but the frequency of the oscillatory motion is low, once again one can not expect that there will be an efficient enhanced axial heat transfer between two reservoirs because the "bus" is now moving too slowly.

The above observation can be confirmed by an analysis of the performance of a water-glass combination (i.e., water is the working fluid medium within a glass tube) and of a mercury-steel combination. For the former, it is necessary to employ rather small diameter tubes and low frequency oscillations with large tidal displacement, for it has

relatively poor heat diffusive properties as compared with the mercury-steel case. This small tube diameter-lower oscillation frequency set-up is necessary in order to ensure that there is sufficient time to transfer the excessive heat content of the bulk water core to the tube wall during the positive stroke of each period and to permit the transfer of excess heat from wall to the cooler core fluid during the negative stroke. Otherwise, the water would just carry a portion of its heat content back and forth in the pipe and the condition for achieving optimum enhanced axial heat transfer could not be met. For the mercury-steel case, one can chose relatively large pipe diameters and higher oscillation frequencies with smaller tidal displacement because of the higher thermal conductivity. This assures that only very short times are needed to exchange the heat between the core of the fluid and the wall. It should be pointed out that the suggestion of using smaller tidal displacement is purely due to the mechanical considerations and that one always tries to keep Δx as large as possible in order to produce large axial heat flows.

From the above discussion, it can be concluded that the process of enhanced heat transfer via oscillatory pumping requires a precise tuning of parameters governing the enhanced heat transport. Indeed there is an expected "tuning effect" as discussed in references [16, 20, 21].

The tuning effect is a very important concept in the study of the presently considered heat transfer process. It shows that there will be an optimum combination between thermal properties of the working medium and wall and the characteristics of the oscillatory motion. The qualitative aspects of the tuning effect have been observed earlier for both the case of a flat channel and that of the cylindrical pipe [15, 16]. From Fig. 4-38, one can see that an optimum for axial heat transfer occurs only at or near the tuning point which depends on the oscillating frequency and the thermodynamic properties of the fluid and wall. As has been pointed out by Kurzweg [20], in order to obtain the optimum enhanced heat transfer one has to carefully select suitable values for the pipe size, the material of pipe and the working medium as well as the manner of oscillatory motion.

The nondimensionalized enhanced heat diffusivity is defined as

$$\lambda = \frac{\kappa_e}{\omega \Delta X^2}$$

(1-10)

where $\kappa_e = \phi/\gamma\rho c$ is the coefficient of enhanced heat diffusivity, ϕ is the axial heat flux, γ is the time-averaged axial temperature gradient, ρ is the density of the fluid, and c is the specific heat. One can show that this nondimensional enhanced heat diffusivity is a function of both the Wormersley number and the Prandtl number [21] and hence that the dimensional axial heat diffusivity κ_e is a

function of the tube radius R_1, the oscillating frequency ω, the kinematic viscosity ν, and the square of the dimensionless tidal displacement ΔX. This can be explained from the fact that the radial heat flow is proportional to the product of the representative radial temperature gradient $\gamma \Delta X / \delta_{th}$ and the surface area per unit depth of $\pi \Delta X$ available for cross-stream heat transport.

The use of large tidal displacement is always beneficial in the enhanced axial heat transfer within oscillating pipe flow. However, in order to avoid the direct convective net mass exchange between the two reservoirs, the tidal displacement must be limited to less than about one half of the pipe length.

As has already been predicted by theoretical studies and will be confirmed by the present numerical simulations, the axial heat transfer will be further enhanced if the rigid surface (part of the rigid wall with finite thickness) has a non-zero thermal diffusivity and hence heat storage capability.

Note that the existing considerations are restricted to laminar flow. Turbulent flow conditions can occur in oscillating pipe flow at higher values of $\omega \Delta x^2 / \nu$ [26, 27] and apparently would destroy the assumptions of the current analytic model of the thermal pumping process. Fortunately, the condition for optimum enhanced heat transfer in such oscillating pipe flow obtained at the tuning point requires

very slender pipes, such that the Reynolds number is usually small enough so that the oscillating motion falls within the laminar range [22].

The theoretical aspects of the oscillatory enhanced axial heat transfer process have been developed much further than its experimental and numerical counterparts. The theoretical predictions are quite limited and consider only cases under certain simplifying assumptions [8]. Numerical work is necessary in order to not only to examine the correctness of the theoretical analysis but also to further the development of advanced enhanced thermal pumping devices. Numerical studies are not only fast, economical and accurate, but they also offer a handy way to access complex geometries which can not be handled analytically.

It is the purpose of this study to extend the analytic work on thermal pumping by a detailed numerical study. We intend first to examine some transient problems of axial heat transfer in oscillatory pipe flow, such as the development of the velocity profile at various Wormersley numbers in contrast with those of reference [36], where only several special cases with intermediate Wormersley number α were discussed, and to examine numerically the relationship between the tidal displacement and the required corresponding strength of the periodic pressure gradient as a function of Wormersley number α and of tidal displacement Δx.

Next, we examine the build-up process of the temperature distribution in a pipe which connects a hot reservoir at one end to a cold reservoir at the other end and see whether there actually exists a constant time-averaged temperature gradient along the pipe axis when the final periodic state is eventually reached. Note that a time-averaged linear temperature distribution along the axial direction is an essential assumption in the existing theoretical studies.

The third part of this investigation which forms the main effort, is a computer-aided numerical simulation of the thermal pumping technique, including an investigation of the variation of the enhanced axial heat flux versus the tidal displacement, the variation of enhanced axial heat flux versus different Wormersley numbers, and a study of the variation of heat flux versus different Prandtl numbers. It also includes a study of the influence of wall thickness and pipe diameter as well as the change of the fluid properties on such an enhanced axial heat flux and an examination of the tuning effect in the conducting wall case. Further, we compare axial heat transfer in oscillating flow with that in the steady flow, and compare quantitatively this enhanced heat flux with that induced by the pure axial molecular conduction under various Wormersley numbers and different fluid-solid wall combinations. Finally, the author examines the phase lag phenomenon in oscillatory flow in order to

further reveal the mechanism whereby this new heat transfer technique functions.

The computational work presented here was completed on the Vax-11/750 electronic computer in the Department of Aerospace Engineering, Mechanics, and Engineering Science, and on Vax-11/780 in the Center for Instructional and Research Computing Activities, University of Florida, Gainesville, Florida. The numerical approach used, for solving the presently considered heat transfer problem, employed a second-order Crank-Nicolson scheme and an Alternating Direction Implicit method (ADI) with Thomas algorithm. A Fortran computer code named ETP (Enhanced Thermal Pumping) was developed to implement all the calculations.

CHAPTER II
FORMULATION OF THE PROBLEM

A single tube with inner radius R_1, outer radius R_2 and length L (such that L >> R_1 and R_2) connects a large reservoir of hot fluid at temperature $T = T_h$ at one end, to another large reservoir of the same fluid at cold temperature $T = T_c$ at the other end (Figs. 2-1 and 2-2). The tidal displacement Δx and the oscillating frequency ω are adjusted to assure that the turbulent flow does not occur. The tube is oriented in such a manner so that the effect of gravity on the oscillatory motion of the fluid in the pipe is negligible. Water and mercury are employed as the working mediums. They are understood to be Newtonian and incompressible fluids. The variations of thermal properties of the fluid with temperature during the heat transport process are assumed to be negligible. With these assumptions the problem of enhanced time-dependent heat transfer induced by a simple harmonic oscillatory laminar fluid motion in a very long circular pipe can then readily be formulated.

Governing Equations

The use of a very slender capillary circular tube with constant cross-sectional area and neglecting end

18
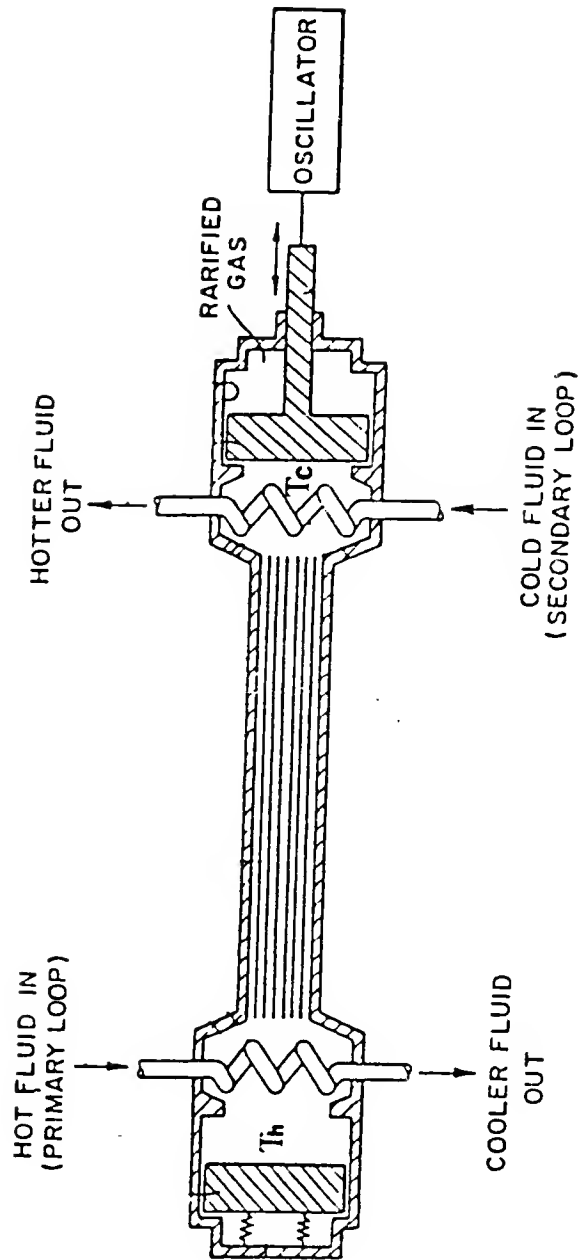
Fig 2-1 Thermal Pumping Device
(after Kurzweg, U.S. Patent, 4,590,993 May 1986)

effects insures a laminar axisymmetrical one-dimensional time-dependent motion. It is convenient to employ cylindrical coordinates for this problem and we denote the coordinate in the axial direction of the tube by x, and the radial direction by r. The axial velocity can be taken to be independent of x and, in order to satisfy the requirements of continuity the other velocity components must vanish. We shall further assume that the pressure gradient induced by moving the piston (Fig. 2-1) is harmonic and has the form [29]

$$- \frac{1}{\rho} \frac{\partial p}{\partial x} = A \cos \omega t \qquad (2-1)$$

where $A = 1/\rho |\partial p/\partial x|$ is a constant which measures the maximum pressure gradient existing along the x-axis. Clearly this equation implies that we are now dealing with a time-dependent sinusoidal pressure gradient which is constant over the pipe cross-section at any instant and the pressure varies linearly along the x-axis. The simplified Navier-Stokes equation for this problem is [36]

$$\frac{\partial U}{\partial t} = A\cos(\omega t) + \frac{\nu}{r} \frac{\partial}{\partial r} \left[r(\frac{\partial U}{\partial r}) \right]$$

$$0 < r < R_1$$

$$(2-2)$$

where $U(r,t)$ is the time and radially dependent axial velocity component.

The corresponding temperature $T(x,r,t)$ of the fluid within the pipe is governed by the heat conduction equation [15]

$$\frac{\partial T}{\partial t} = -U \frac{\partial T}{\partial x} + \kappa_f \left[\frac{1}{r} \frac{\partial}{\partial r} (r \frac{\partial T}{\partial r}) + \frac{\partial^2 T}{\partial x^2} \right]$$

$$0 < r < R_1$$

$$(2-3)$$

where R_1 is the inner radius of the tube and κ_f the fluid thermal diffusivity which is related the thermal conductivity k_f by

$$\kappa_f = \frac{k_f}{\rho c}$$

Here ρ is the fluid density, and c is the specific heat. Note that the viscous heating term has been neglected in equation (2-3) since it is very small for most experimental conditions; this is justified provided one does not deal with very high Prandtl number fluids such as oils. The temperature in the wall can be determined from the solution of

$$\frac{\partial T}{\partial t} = \kappa_w \left[\frac{1}{r} \frac{\partial}{\partial r} (r \frac{\partial T}{\partial r}) + \frac{\partial^2 T}{\partial x^2} \right]$$

$$R_1 < r < R_2$$

$$(2-4)$$

where κ_w is the thermal diffusivity of the conducting wall in $R_1 < r < R_2$ and is defined by

$$\kappa_W = \frac{k_W}{\rho_W c_W}$$

where k_W, ρ_W, and c_W, are the wall conductivity, density, and the specific heat, respectively. By introducing the following non-dimensional terms, equation (2-2), (2-3) and (2-4) can be treated more easily.

$$t^* = \frac{t}{1/\omega} \qquad\qquad x^* = \frac{x}{\delta}$$

$$r^* = \frac{r}{\delta} \qquad\qquad U^* = \frac{U}{A/\omega}$$

$$T^* = \frac{T}{T_h - T_c}$$

where $\delta = \sqrt{2\nu/\omega}$ is again the fluid viscous boundary layer thickness. The dimensionless governing system of equations can then be written as

$$\frac{\partial U^*}{\partial t^*} = \cos(t^*) + \frac{1}{2}\left[\frac{\partial^2 U^*}{\partial r^{*2}} + \frac{1}{r^*}\frac{\partial U^*}{\partial r^*}\right]$$

$$0 < r < R_1$$

$$(2\text{-}5)$$

$$\frac{\partial T^*}{\partial t^*} = CU^*\frac{\partial T^*}{\partial x^*} + \frac{1}{2Pr}\left[\frac{\partial^2 T^*}{\partial r^{*2}} + \frac{1}{r^*}\frac{\partial T^*}{\partial r^*} + \frac{\partial^2 T^*}{\partial x^{*2}}\right]$$

$$0 < r < R_1$$

$$(2\text{-}6)$$

and

$$\frac{\partial T^*}{\partial t^*} = \frac{1}{2S}\left[\frac{\partial^2 T^*}{r^{*2}} + \frac{1}{r^*}\frac{\partial T^*}{\partial r^*} + \frac{\partial^2 T^*}{\partial x^{*2}}\right]$$

$$R_1 < r < R_2$$

$$(2\text{-}7)$$

where

$$Pr = \frac{\mu \ c_f}{\kappa}$$

$$S = \frac{\mu \ c_w}{\kappa_w}$$

and

$$C = \frac{-A}{\omega^2 \delta}$$

This nondimensionalization has some advantages in the computing process to be carried out below. The dimensionless velocity and its distribution over the cross-section found from the momentum equation (2-5) are expected to be universal for any Wormersley number $\alpha = R_1\sqrt{\omega\rho/\mu}$ and any associated quantities, such as the tidal displacement and Lagrangian displacement. Its final periodic form is of the form given by (1-4). The dimensionless temperature in the pipe is only related to the Prantdl number and the dimensionless velocity, while that in the wall is related to the ratio of wall heat diffusivity to the kinematic viscosity, as seen from equation (2-6) and (2-7).

The governing dimensionless equations (2-5), (2-6), and (2-7) are a set of second-order parabolic type of partial differential equations expressed in cylindrical coordinates. To solve this set of simultaneous equations, a corresponding set of boundary conditions and initial conditions are required. Since the velocity is assumed to be a function of r and t only, just two boundary conditions

are needed for solving the momentum equation, while for the temperature $T(x,r,t)$ the heat conduction equations require two boundary conditions in both the r and x directions as well as compatibility conditions along the interface between the fluid and the solid wall. It should be pointed out that the initial conditions are less important than the boundary conditions if one seeks only a final periodic state.

Boundary Conditions

The boundary conditions for the velocity are the usual ones for viscous flow, namely, that the velocity is zero at the inner surface of the wall ($r^* = R_1^*$). Also by symmetry, the normal derivative of velocity at the axis is zero. That is,

$$U^*(R_1^*, t^*) = 0 \qquad\qquad (2-8)$$

and

$$\frac{\partial U^*(0, t^*)}{\partial r^*} = 0 \qquad\qquad (2-9)$$

The boundary conditions for the temperature depend on the particular model investigated.

Model 1

In this model, it is assumed that the temperature at each end of the pipe is equal to that of the connecting fluid filling the reservoirs when the fluid moves into the capillary tube (i.e., during one half of each cycle). The
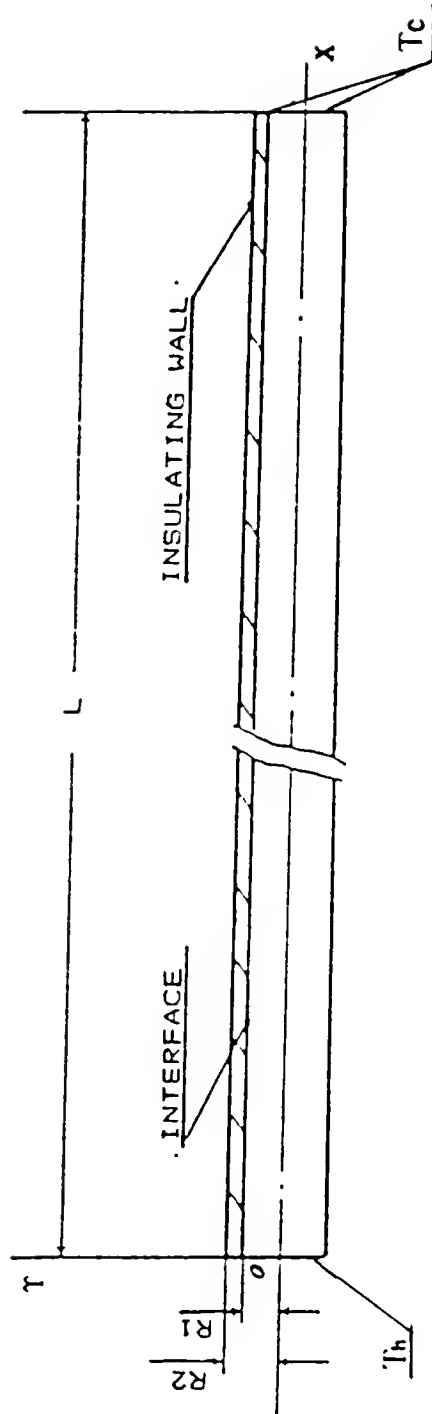
Fig 2-2   Model 1 ——— Fixed End Temperature Model
L=20cm,   R₁=0.1cm,   R₂=0.15cm

end boundary temperature at x = 0 and x = L will take the
values of temperature of the adjacent pipe fluid elements.
With this model, we tried to simulate the real experimental
observations where it can be clearly seen that a fluid jet
exits the pipe during the outstroke, while the elements of
the fluid enter the tube in a funnel pattern during the
instroke. This observation shows that there is enough time
during each oscillating cycle to allow the fluid elements
within the exiting jet to fully mix with the fluid particles
which originally are in the reservoir before the next
instroke, provided the oscillating frequency is not too
high. The end temperature boundary conditions are here
taken as

$$T^*(0, r^*, t^*) = \begin{cases} T^*_h & \text{(when fluid enters pipe)} \\ \\ T^*_{adj} & \text{(when fluid leaves pipe)} \end{cases}$$

(2-10)

$$T^*(L^*, r^*, t^*) = \begin{cases} T^*_c & \text{(when fluid enters pipe)} \\ \\ T^*_{adj} & \text{(when fluid leaves pipe)} \end{cases}$$

(2-11)

where T^*_c, T^*_h are the nondimensional temperatures of cold
and hot reservoirs, respectively. While T^*_{adj} is the

temperature of the fluid elements which are adjacent to the corresponding ends at a particular instant.

The thermal boundary conditions along the outer surface $r^* = R_2$ of the pipe wall are taken to satisfy the insulating wall condition, and along the axis of the tube the temperature is assumed to meet the symmetric boundary requirement, i.e., the radial derivatives of temperature along axis are equal to zero. We thus have

$$\frac{\partial T^*}{\partial r^*}\bigg|_{r^* = R_2^*} = 0 \qquad\qquad (2\text{-}12)$$

and

$$\frac{\partial T^*}{\partial r^*}\bigg|_{r^* = 0} = 0 \qquad\qquad (2\text{-}13)$$

The compatibility conditions along the interface between the fluid and the solid wall are that the radial heat flux and temperature are constant across the interface. That is

$$k_f \frac{\partial T^*}{\partial r^*}\bigg|_{fluid} = k_w \frac{\partial T^*}{\partial r^*}\bigg|_{wall} \qquad \text{at } r = R_1 \qquad (2\text{-}14)$$

and

$$T^*\bigg|_{fluid} = T^*\bigg|_{wall} \qquad\qquad \text{at } r = R_1 \qquad (2\text{-}15)$$

Since numerically the same nodes are chosen along the interface, condition (2-15) will be automatically satisfied.

Model 2

Here it is assumed that a heat source rim of width 2b is directly mounted on the interface between the solid wall and the fluid at x = L/2, while two small cold rim sources of width b each are mounted at x = 0 and x = L (see Fig. 2-3). The wall thickness is assumed to be zero. This model is intended to simulate the enhanced heat transfer process of oscillatory fluid in an infinitely long pipe which is heated and cooled by the alternative evenly distributed heat and cold sources along the outer surface of a very thin wall which possesses infinite heat conductivity. Apparently, this geometry can be well simulated by the present model with periodic boundary conditions. Mathematically the boundary conditions are

$$T^*(x^*, R1^*, t^*) = T^*_h \qquad X2^* \leq x^* \geq X3^* \qquad (2\text{-}14)$$

$$T^*(x^*, R1^*, t^*) = T^*_c \qquad \text{or} \quad \begin{array}{c} 0 \leq x^* \leq X1^* \\ X4^* \leq x^* \leq L^* \end{array} \qquad (2\text{-}15)$$

$$\frac{\partial T^*}{\partial r^*} = 0 \qquad \text{or} \quad \begin{array}{c} X1^* < x^* < X2^* \\ X3^* < x^* < X4^* \end{array} \qquad (2\text{-}16)$$

where $X1^*$, $X2^*$, $X3^*$, $X4^*$, $X5^*$ and $X6^*$ are nondimensional coordinates of points which correspond to X = 0, b, L/2-b, L/2+b, L-b, and L, respectively in Fig. 2-3. The periodic end boundary conditions are given as
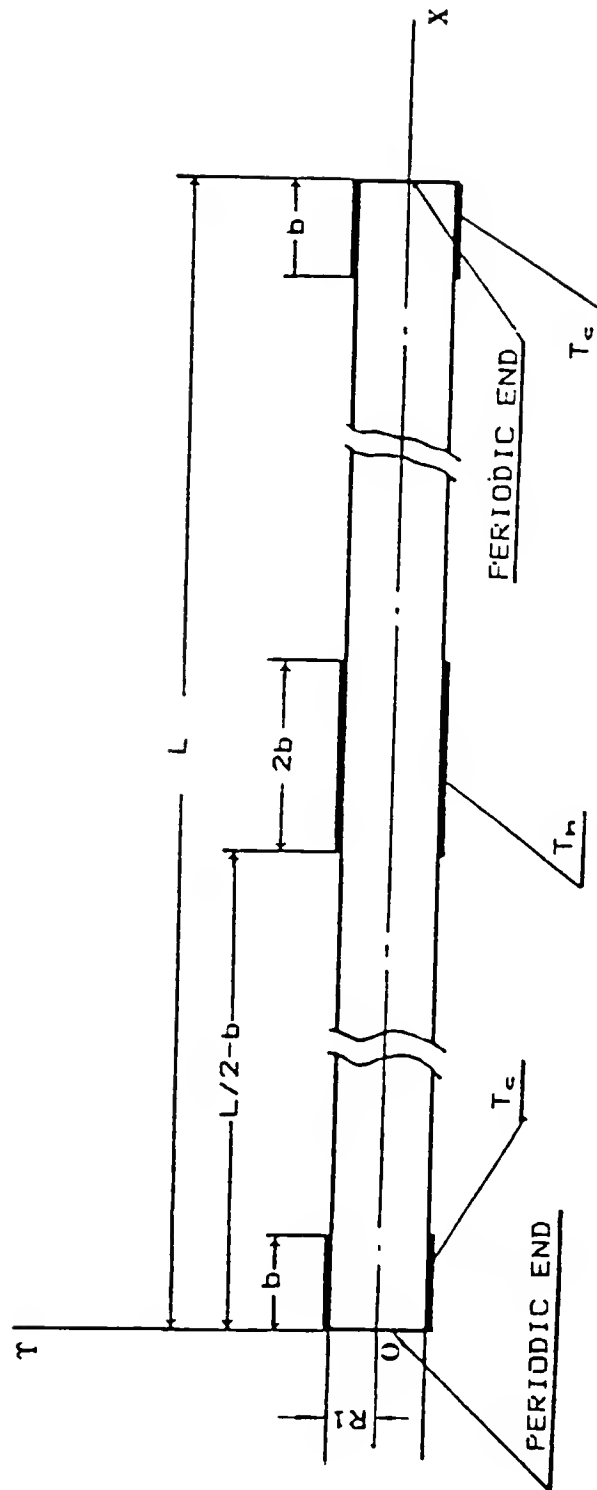
Fig 2-3   Model 2 ――― Periodic Heat And Cold Sources
on Insulated Wall (Except Sources Area)
L=20cm,   R₁=0.1cm,   b=1cm

$$T^*(0, r^*, t^*) = T^*(L^*, r^*, t^*) \qquad (2-17)$$

and

$$\frac{\partial T^*}{\partial x^*} \bigg|_{x^* = 0} = \frac{\partial T^*}{\partial x^*} \bigg|_{x^* = L^*} \qquad (2-18)$$

Model 3

    In model 1, the boundary conditions for the heat equation at X = 0 and L are somewhat artificial. The temperature distribution in the vicinity of pipe ends may not precisely match the constant temperature end conditions. This is particularly true in the large tidal displacement and/or very high oscillating frequency cases since a temperature drop occurs at the hot end and a rise at the cold end as fluid particles exit the pipe. This leads to a discontinuity of temperature which will lead to unexpected dispersion errors if an even order numerical method is used [3, 24, 30]. To improve the end boundary conditions presented in model 1, the following extended model has been considered. It is assumed that an extension pipe which is some 5 times the length of the central pipe is attached to the original pipe used in model 1. The heat and cold source are assumed to be located on the outer surface of the wall in the extended sections of the pipe as well as at both ends of the tube as shown in Fig. 2-4. This model is used to
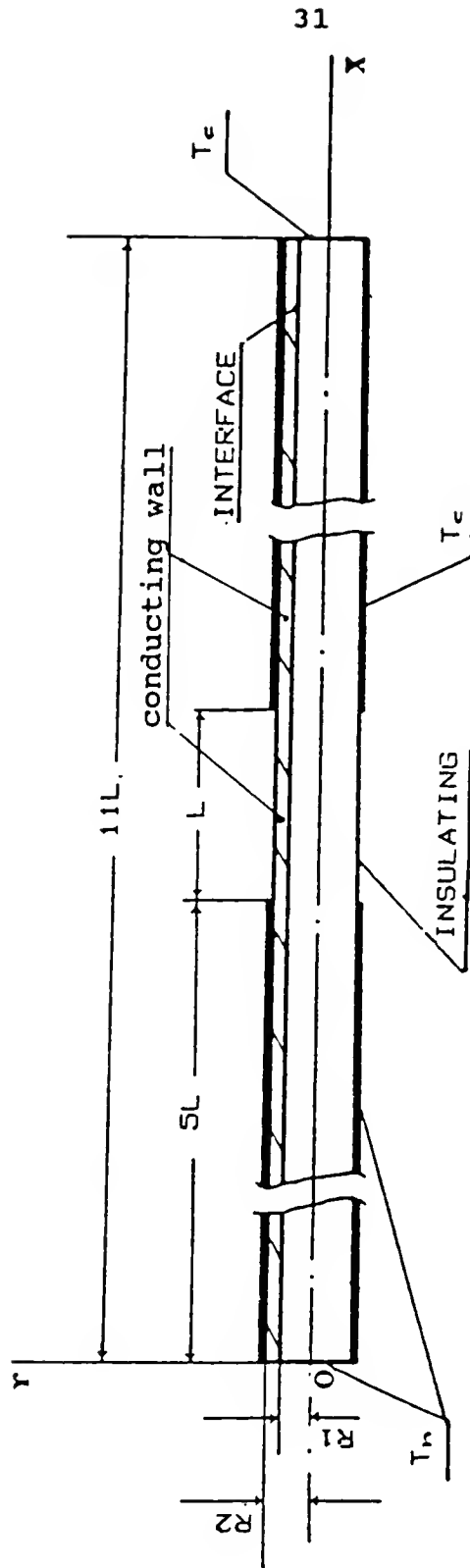
Fig 2-4   Model 3 ●━━● Pipe with Conducting Pieces Model
L=20cm, R_1=0.1cm

investigate the situation where the heat contained in the jet is exchanged by pure heat conduction with the surrounding fluid elements in each reservoir without any convective mixing. In this case, the boundary conditions along the outer surface of the wall are

$$T^* = T^*_h \; , \qquad\qquad 0 \le x^* \le X1^* \qquad\qquad (2\text{-}19)$$

$$T^* = T^*_c \qquad\qquad X2^* \le x^* \le X3^* \qquad\qquad (2\text{-}20)$$

and

$$\frac{\partial T^*}{\partial r^*} = 0 \qquad\qquad X1^* \le x^* \le X2^* \qquad\qquad (2\text{-}21)$$

where $X1^*$, $X2^*$, and $X3^*$ are nondimensional coordinates of points which correspond to X = 5L, 6L, and 11L, respectively, in Fig. 2-4. At both ends, we have

$$T^*(0, r^*, t^*) = T^*_h \qquad\qquad (2\text{-}22)$$

and

$$T^*(L^*, r^*, t^*) = T^*_c \qquad\qquad (2\text{-}23)$$

As in the other models, the symmetry condition along the axis of pipe requires that

$$\frac{\partial T^*}{\partial r^*} \bigg|_{r^*=0} = 0 \qquad\qquad (2\text{-}24)$$

and the radial flux and temperature continuity condition along the interface are

$$k_f \left. \frac{\partial T^*}{\partial r^*} \right|_{fluid} = k_w \left. \frac{\partial T^*}{\partial r^*} \right|_{wall} \tag{2-25}$$

and

$$\left. T^* \right|_{fluid} = \left. T^* \right|_{wall} \tag{2-26}$$

Here again k_f and k_w are the same as described in the previous models.

Initial Conditions

The initial condition chosen depends on the problem under consideration. If one's goal is to investigate the periodic quasi-steady solution only, the initial conditions chosen should be as close to the quasi-steady state as possible so that a rapid convergence rate at low CPU time cost is achievable. If one intends to study the transient process, then various initial conditions should be supplied according to purpose of the investigating cases selected. For the velocity initial condition we choose for all our studies

$$U^*(x^*, r^*, 0) = 0 \tag{2-27}$$

For the temperature, if the purpose of investigation is to examine the build-up process of the periodic quasi-steady

state in the thermal field, the initial condition should be taken as

$$T^*(x^*, r^*, 0) = 0 \qquad (2\text{-}28)$$

However, for the other cases, in order to gain faster convergence, the initial temperature can be assumed to have a linear distribution in the axial direction, and thus have the form

$$T^*(x^*, r^*, 0) = T^*_h + \frac{(T^*_c - T^*_h)xx^*}{LL^*} \qquad (2\text{-}29)$$

where LL^* is the dimensionless length within which the axial linear temperature distribution is assumed to hold, and xx^* is the dimensionless distance measured from the "origin" which is chosen only for the purpose of this linear temperature initialization. Both the LL^* and the origin selected depend on the model considered. For Model 1 and Model 3, LL^* is equal to L^*, and the origin is taken at the left end (Model 1), or at the left intersection between the central pipe and the left extension pipe (Model 3). However, for Model 2, equation (2-29) is valid only for the right half portion of the pipe as LL^* is taken to be $L^*/2$, and the origin is chosen at the middle section of the pipe. The initial temperature of the left half pipe can then be found from the plane symmetric condition about the origin cross-section.

Calculation of Tidal Displacement

An important quantity encountered in the study of the enhanced heat transfer process in oscillatory pipe flow is the tidal displacement, which is usually required to be smaller than one half of the total pipe length in order to avoid any convective mass exchange occurring between the two reservoirs. It has already been defined in the introduction chapter (1-6) and in the present computation the dimensional tidal displacement takes the form

$$\Delta x = \frac{2}{R_1^2} \int_0^{R1} \chi(r, \pi/\omega) r \, dr \qquad (2-30)$$

where R_1 is the inner radius of the pipe and $\chi(r, \pi/\omega)$ is the Lagrangian displacement of the fluid elements located along a radius within the capillary tube at $t = \pi/\omega$. It is assumed these elements are initially lined up at axial position $x = L/2$ (Model 1 and Model 2) or $x = 5.5L$ (Model 3), half way between the tube ends. Numerically, the dimensional Lagrangian displacement at time t is computed via the equation

$$\chi(r, t) = \int_0^t U(r, t) \, dt \qquad (2-31)$$

It is obvious that the dimensional Lagrangian displacement $\chi(r,t)$ is a function of both time t and the radial position r. Note that, since the existence of phase lags between the

stimulating pressure gradient and the displacements vary for different Wormersley numbers, in actual calculations, the tidal displacement is equal to the sum of the absolute maximum cross-section averaged Lagrangian displacement and the absolute minimum cross-section averaged Lagrangian displacement within a period. With the same non-dimensionalizaton procedure used in the previous section for the governing equations, the dimensionless Lagrangian and tidal displacement can be written as

$$\Delta X^* = 2 \int_0^{R^*} \chi^*(r^*, \pi/\omega) r^* dr^* \qquad (2\text{-}32)$$

The nondimensional Lagrangian displacement within the period can then be computed by

$$\chi^*(r^*, t^*) = \int_0^{t^*} U^*(r^*, t^*) dt^* \qquad (2\text{-}33)$$

where

$$\chi^* = \frac{\chi}{(A/\omega^2)}$$

and

$$\Delta X^* = \frac{\Delta X}{(A/\omega^2)}$$

It is pointed out that this dimensionless tidal displacement Δx^* differs from ΔX defined by equation (1-7) by a constant 1/2.

Effective Heat Flux

The time averaged total effective axial heat flow within the pipe has the form

$$Q_{total} = c\rho\omega \int_0^{2\pi/\omega} dt \int_0^{R_1} UTrdr \qquad (2-34)$$

where c is the specific heat, ρ is the density and again, ω is the oscillatory frequency. The per unit area effective heat flow (termed heat flux) can then be written as

$$\phi = \frac{Q_{total}}{\pi R_1^2} \qquad (2-35)$$

Equation (2-34) follows from the fact that ρcUT is the convective heat flux. The dimensionless total effective heat flow can be written as

$$Q^*_{total} = c\rho\omega \int_0^{2\pi} dt^* \int_0^{R1^*} U^*T^*r^*dr^* \qquad (2-36)$$

and the dimensionless heat flux by

$$\phi^* = \frac{Q^*_{total}}{\pi R^{*2}} \qquad (2-37)$$

CHAPTER III
NUMERICAL TECHNIQUES EMPLOYED

Equations (2-5), (2-6) and (2-7) which were derived in Chapter II can not generally be solved analytically in any simple manner. Therefore, it is necessary to seek a numerical solution approach to the problem.

As is well known, in order to numerically solve a set of simultaneous governing differential equations more accurately and efficiently, an optimized grid system plays a very important role. For the present purpose the grid networks were generated in the following way: within the tube, a non-uniform grid (see Fig. 3-1) is clustered along the radial direction in the vicinity of the inner surface of the pipe where the larger gradients of velocity and temperature are expected to be present, while along the x-axis the grid is distributed uniformly except for those calculations dealing with model 3.

The solution process was carried out in the computational plane rather than directly in the physical plane. Thus, a transformation which converts the governing equations as well as the boundary condition plays an essential role.

38
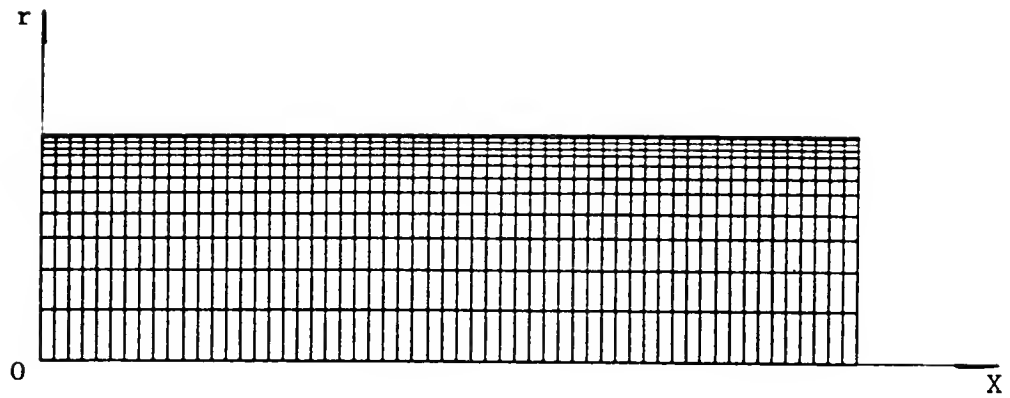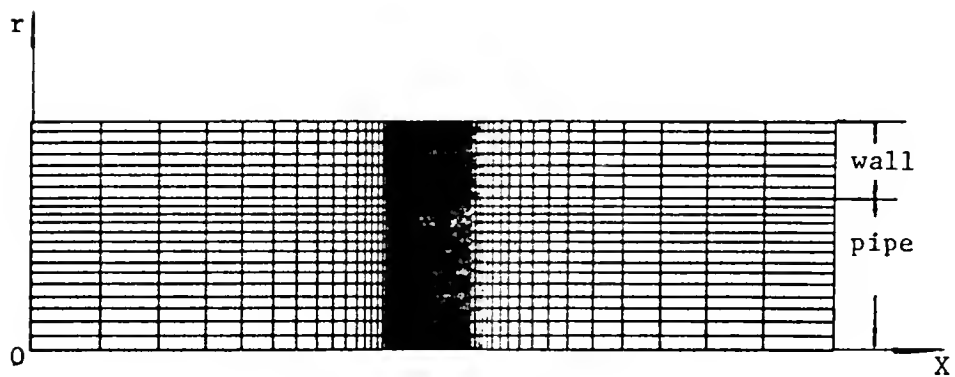
1). For Model 1

2). for Model 3

Fig 3-1 Grid Systems Used in the Numerical Simulations

The second-order implicit unconditionally stable Crank-Nicolson scheme and the ADI method [2, 31] are employed to break up the transformed equations into finite difference form. A computer code designated ETP (for Enhanced Thermal Pumping) has been developed for obtaining the desired results. Details of this procedure will be described in this chapter.

Transformation

The numerical solution of a system of partial differential equations can be greatly simplified by a well-constructed grid. It is also true that an improper choice of grid point locations can lead to an apparent instability or lack of convergence. Early work using finite difference methods was restricted to some simple problems which can be numerically solved in the physical domain. As experience was gained, general mappings were used to transform the physical plane into the computational domain as well as the governing differential equations [31]. Such a grid transformation technique brought to the numerical simulation numerous advantages, and the computational work was no longer restricted to a few simple geometries. A body-fitted non-uniform grid in the physical domain could be used, which retains the uniform spaced grid system features in the computational domain [33, 34, 35]. However, several requirements must be placed on the transformation: first, the mapping must be one to one, second, the grid lines must

be smooth and have small skewness in the physical domain, third, grid node point spacing should be small where large numerical errors are expected (i.e., large solution gradient regions) in the physical domain (Fig. 3-2).

In present study, the grid system in the physical space is numerically generated by solving an algebraic equation which clusters the grid lines in the region where large gradients of the physical quantities are expected so as to gain higher resolution of these physical quantities. Because of the simple pipe geometry, the requirements of grid smoothness and orthogonality are not a serious problem. For the present purpose, the transformation is a simple one which transforms a non-uniform grid network in the physical plane onto a uniform grid system in the computational plane.

$$x^* = x^*(\xi)$$
$$r^* = r^*(\eta)$$
$$t^* = t^*(\tau) \tag{3-1}$$

The inverse transformation can be found as

$$\xi = \xi(x^*)$$
$$\eta = \eta(r^*)$$
$$\tau = \tau(t^*) \tag{3-2}$$

where x^*, r^* are the dimensionless coordinates and t^* the dimensionless time in the physical domain, ξ, η are the transformed coordinates and τ is the transformed time in the

42
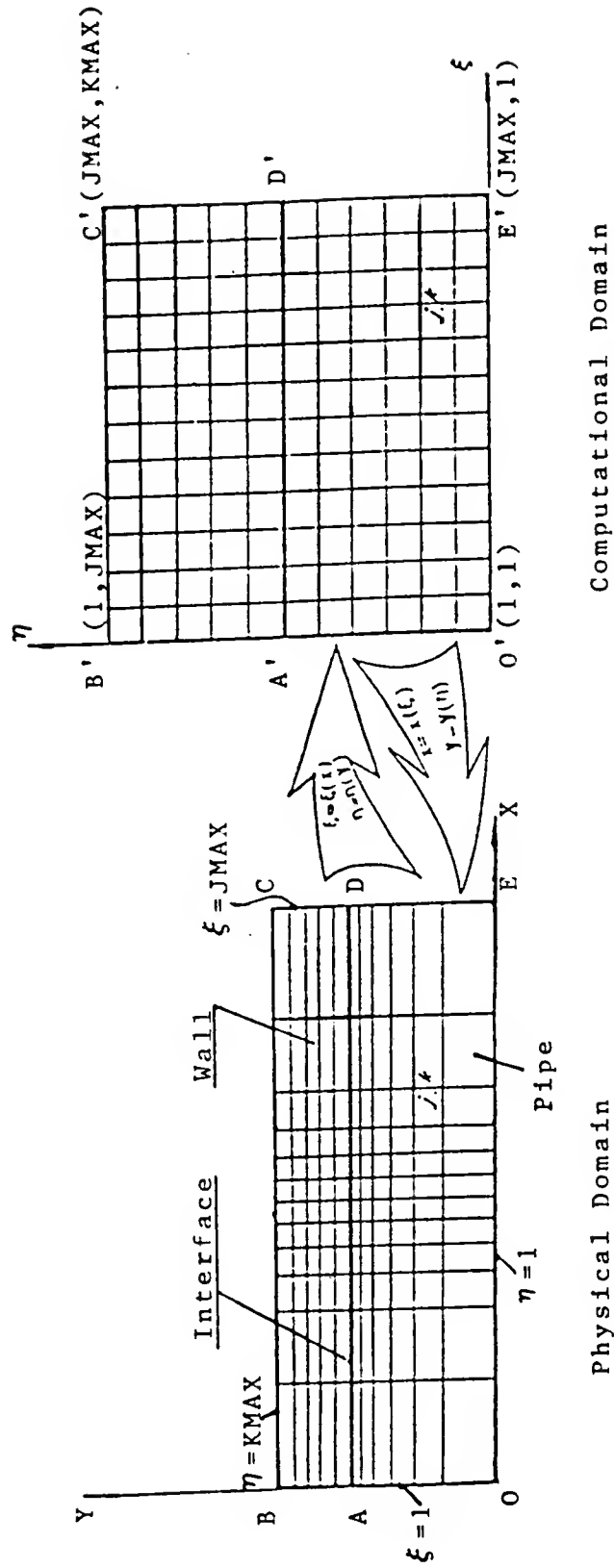
Fig. 3-2 Coordinates Transformation

computational domain. With this transformation, the transformed governing equations have the form:

$$\frac{\partial U^*}{\partial \tau} = f(\tau) + a(\eta)\frac{\partial^2 U^*}{\partial \eta^2} + b(\eta)\frac{\partial U^*}{\partial \eta} \tag{3-3}$$

$$\frac{\partial T^*}{\partial \tau} = P1\frac{\partial T^*}{\partial \xi} + P2\frac{\partial^2 T^*}{\partial \xi^2} + P3\frac{\partial T^*}{\partial \eta} + P4\frac{\partial^2 T^*}{\partial \eta^2} \tag{3-4}$$

and

$$\frac{\partial T^*}{\partial \tau} = w1\frac{\partial T^*}{\partial \xi} + w2\frac{\partial^2 T^*}{\partial \xi^2} + w3\frac{\partial T^*}{\partial \eta} + w4\frac{\partial^2 T^*}{\partial \eta^2} \tag{3-5}$$

where

$$f(\tau) = \frac{\partial t^*}{\partial \tau}\cos(t^*) \tag{3-6}$$

$$a(\eta) = \frac{1}{2}\frac{\partial t^*}{\partial \tau}\frac{1}{(\partial r^*/\partial \eta)^2} \tag{3-7}$$

$$b(\eta) = \frac{1}{2}\frac{\partial t^*}{\partial \tau}\left(\frac{1}{r^*(\partial r^*/\partial \eta)} - \frac{1}{(\partial r^*/\partial \eta)^3}\frac{\partial^2 r^*}{\partial \eta^2}\right) \tag{3-8}$$

and

$$P1 = \frac{\partial t^*}{\partial \tau}\left(\frac{CU^*}{\partial x^*/\partial \xi} - \frac{1}{2Pr(\partial x^*/\partial \xi)^3} + \frac{\partial^2 x^*}{\partial \xi_2}\right) \tag{3-9}$$

$$P2 = \frac{\partial t^*}{\partial \tau}\frac{1}{2Pr(\partial x^*/\partial \xi^2)} \tag{3-10}$$

$$P3 = \frac{\partial t^*}{\partial \tau}\frac{1}{2Pr}\left(\frac{1}{r^*(\partial r^*/\partial \eta)} - \frac{1}{(\partial r^*/\partial \eta)^3}\frac{\partial^2 r^*}{\partial \eta^2}\right) \tag{3-11}$$

$$P4 = \frac{\partial t^*}{\partial \tau}\frac{1}{2Pr\ (\partial r^*/\partial \eta)^2} \tag{3-12}$$

$$W1 = \frac{\partial t^*}{\partial \tau} \frac{1}{2Pr_w} \left(\frac{-1}{(\partial x^*/\partial \xi)^3} \frac{\partial^2 x^*}{\partial \eta^2} \right) \qquad (3-13)$$

$$W2 = \frac{\partial t^*}{\partial \tau} \frac{1}{2Pr_w} \frac{1}{(\partial x^*/\partial \xi)^2} \qquad (3-14)$$

$$W3 = \frac{\partial t^*}{\partial \tau} \frac{1}{2Pr_w} \left[\frac{1}{r^*(\partial r^*/\partial \eta)} - \frac{1}{(\partial r^*/\partial \eta)^3} \frac{\partial^2 r^*}{\partial \eta^2} \right] \qquad (3-15)$$

$$W4 = \frac{\partial t^*}{\partial \tau} \frac{1}{2Pr_w} \frac{1}{(\partial r^*/\partial \eta)^2} \qquad (3-16)$$

As mentioned in chapter II, equations (3-3), (3-4) and (3-5) are a set of second-order parabolic partial difference equations in cylindrical coordinates. In addition, since the oscillating flow is considered as incompressible in the present studies, the momentum equation (3-3) can then be independently solved at each time step. As a result, the time-dependent update velocity found can then be substituted into the heat conduction equation (3-4) as a known quantity at the same time step level. Eventually, the coupled heat conduction equations (3-4) and (3-5) are solved simultaneously to obtain the temperature distribution both in the fluid and in the wall at any time. To best solve this set of equations in terms of accuracy and efficiency, the proper choice of numerical technique and grid net-work is dictated by an understanding of the physical aspects of the problem.

The same transformation should be also applied on all the boundary conditions proposed in the three different models. For the temperature compatibility conditions along the interface between the fluid and the wall (2-25) one has the following transformed forms:

$$\frac{\partial T^*}{\partial \eta} \frac{1}{(\partial r^*/\partial \eta)} k_f \bigg|_{fluid} = \frac{\partial T^*}{\partial \eta} \frac{1}{(\partial r^*/\partial \eta)} k_w \bigg|_{wall} \qquad (3\text{-}17)$$

or

$$\frac{\partial T^*}{\partial \eta} \bigg|_{flow} = K_a \frac{\partial T^*}{\partial \eta} \bigg|_{wall} \qquad (3\text{-}18)$$

where

$$K_a = \frac{k_w \, \partial r^*/\partial \eta \big|_{pipe}}{k_f \, \partial r^*/\partial \eta \big|_{wall}} \qquad (3\text{-}19)$$

To make the subsequent form of the corresponding finite difference governing equations less cumbersome, the superscript " * " will be dropped from the variables T^*, r^*, t^*, and x^*, and in addition, U^* will be replaced by V.

In the process of deriving the finite difference governing system equations, the second-order central differences in the domain and forward or backward differences along the boundaries or interface of the fluid and wall have been employed at each nodal point.

Crank-Nicolson Method for Momentum Equation

The second-order accurate Crank-Nicolson method is quite well known and widely used. It is an unconditional stable, implicit scheme for solving the parabolic types of partial difference equations. When the Crank-Nicolson method is applied to equation (3-3), the finite difference algorithm at a typical node k in the radial direction and at the time step n assumes the simpler form:

$$\left(B_k V_{k-1} + D_k V_k + A_k V_{k+1} \right)^{n+1} = C_k^n$$

$$k = 1, 2, \ldots\ldots km$$

$$(3-20)$$

where

$$C_k = \frac{1}{2}\left(f^{n+1} + f^n \right) - \left(B_k V_{k-1} + E_k V_k - A_k V_{k+1} \right)^n \quad (3-21)$$

$$A_k = -\frac{1}{4}(2a + b)_k \quad (3-22)$$

$$B_k = \frac{1}{4}(2a + b)_k \quad (3-23)$$

$$D_k = 1 + a_k \quad (3-24)$$

$$E_k = 1 - a_k \quad (3-25)$$

The boundary conditions along the interface (i.e., the inner surface of the wall, k = kmid) and the axis (k = 1) then become

$$V \Big|_{k \,=\, kmid} = 0$$

(3-26)

$$\frac{\partial V}{\partial \eta} \Big|_{k \,=\, 1} = 0$$

The initial conditions of the velocity at all nodal points is taken to be zero.

$$V_k^n \Big|_{n \,=\, 1} = 0$$

$$k = 1, \ 2, \ 3, \ \dots\dots kmid$$

(3-27)

Equation (3-20) associated with the boundary conditions (3-26) can then be written in the matrix form. This yields a set of linear system algebraic equations which can be solved in terms of the nodal values of velocity in the capillary tube by using either an iterative method or a Thomas algorithm at each time step. The explicit form is

$$
\begin{bmatrix}
D_1 & A_1^* & & & & & \\
B_2 & D_2 & A_2 & & & & \\
 & B_3 & D_3 & A_3 & & & \\
 & & \cdot & \cdot & \cdot & & \\
 & & & \cdot & \cdot & \cdot & \\
 & & & & B_{kd-1} & D_{kd-1} & A_{kd-1} \\
 & & & & & B_{kd} & D_{kd}
\end{bmatrix}^n
\begin{Bmatrix}
V_1 \\ V_2 \\ V_3 \\ \cdot \\ \cdot \\ \cdot \\ V_{kd-1} \\ V_{kd}
\end{Bmatrix}^{n+1}
=
\begin{Bmatrix}
C_1 \\ C_2 \\ C_3 \\ \cdot \\ \cdot \\ \cdot \\ V_{kd-1} \\ V_{kd}
\end{Bmatrix}^n
$$

$$(3\text{-}28)$$

where

$$A_1^* = A_1 + B_1$$

$$kd = kmid-1$$

ADI Method for Axisymmetric Heat Equations

The governing PDEs (3-3), (3-4) and (3-5) are all of the second-order parabolic type. Thus it might be suggested that the Crank-Nicolson scheme used in solving the momentum equation (3-3) can also be applied to the axisymmetric heat equations (3-4) and (3-5), and one can then take advantage of the tridiagonal matrix form while using this unconditionally stable technique. However, when attempting to use such a formulation, one immediately finds that the resulting system of linear algebraic equations is no longer of the tridiagonal type (3-20) but rather a non-tridiagonal matrix system requiring substantial CPU time to solve. This difficulty can be avoided by applying the unconditionally stable Alternating Direction Implicit method (ADI),

developed by Peaceman and Rachford and Douglas in 1955. According to this scheme, the entire solution process at each time step is "split" into two portions, i.e., the first half of solution processes for k^{th} column (radial direction), while the other half processes for the jth row (axial direction).

With the ADI scheme, second-order central differences are used to approximate the values of derivatives at each nodal point in equations (3-4), (3-5). The finite difference algorithm for those equations during the first half of each time step for the jth column are then

$$\left(BP_{jj,k}T_{jj,k-1} + DP_{jj,k}T_{jj,k} + AP_{jj,k}T_{jj,k+1} \right)^{n+1/2} = PX_{jj,k}^{n}$$

$$k = 1, 2, \ldots kmid$$

(3-29)

and

$$\left(BW_{jj,k}T_{jj,k-1} + DW_{jj,k}T_{jj,k} + AW_{jj,k}T_{jj,k+1} \right)^{n+1/2} = WX_{jj,k}^{n}$$

$$k = kmid+1, \ldots kmax$$

(3-30)

where the subscript jj is used to emphasize the specific column currently to be computed. It can be seen that the set of difference equations now is in the tridiagonal form

since the right-hand-side terms in the equations (3-29), (3-30) contain only known values from the previous results and the boundary conditions. These values can be computed by

$$PX_{jj,k}^{n} = \left(-CP_{jj,k}T_{jj-1,k} + EP_{jj,k}T_{jj,k} - FP_{jj,k}T_{jj+1,k}\right)^{n}$$

$$(3-31)$$

and

$$WX_{jj,k}^{n} = \left(-CW_{jj,k}T_{jj-1,k} + EW_{jj,k}T_{jj,k} - FW_{jj,k}T_{jj+1,k}\right)^{n}$$

$$(3-32)$$

The computational algorithm is implemented column by column and the unknown value $(T_{j,k})^{n}$ can then be solved by either an iterative or a direct method. In order to do this, equation (3-29) needs to be assembled into the following matrix form.

$$\begin{bmatrix} PD_1 & PA_1 & & & & & \\ PB_2 & PD_2 & PA_2 & & & & \\ & PB_3 & PD_3 & PA_3 & & & \\ & & \cdot & & \cdot & & \\ & & & \cdot & & \cdot & \cdot \\ & & & & \cdot & \cdot & \cdot \\ & & & & PB_{kd-1} & PD_{kd-1} & PA_{kd-1} \\ & * & & & & PB_{kd} & PD_{kd} \end{bmatrix}_j^{n} * \begin{bmatrix} T_1 \\ T_2 \\ T_3 \\ \cdot \\ \cdot \\ \cdot \\ T_{kd-1} \\ T_{kd} \end{bmatrix}_j^{n+1/2} = \begin{bmatrix} PX_1 \\ PX_2 \\ PX_3 \\ \cdot \\ \cdot \\ \cdot \\ PX_{kd-1} \\ PX_{kd} \end{bmatrix}_j^{n}$$

$$j = 1, 2, 3 \ldots\ldots jmax$$

$$(3-33)$$

Similarly, equation (3-30) can be assembled into the matrix form as seen in (3-34).

$$
\begin{bmatrix}
WD_{kd+1} & WA_{kd+1} & & & & * \\
WB_{kd+2} & WD_{kd+2} & WA_{kd+2} & & & \\
& \cdot & \cdot & \cdot & & \\
& & \cdot & \cdot & \cdot & \\
& & & \cdot & \cdot & \cdot \\
& & WB_{km} & WD_{km} & WA_{km} & \\
* & & & WB_{kmax} & WD_{kmax}
\end{bmatrix}_j^n
\begin{bmatrix}
T_{kd+1} \\
T_{kd+2} \\
\cdot \\
\cdot \\
\cdot \\
T_{km} \\
T_{kmax}
\end{bmatrix}_j^{n+1/2}
=
\begin{bmatrix}
WX_{kd+1} \\
WX_{kd+2} \\
\cdot \\
\cdot \\
\cdot \\
WX_{km-1} \\
WX_{kmax}
\end{bmatrix}^n
$$

$$j = 1, 2, 3 \ldots\ldots jmax$$

$$(3-34)$$

It should be pointed out that the coefficients and/or the right hand side terms in the row marked with symbol "*" in those matrixes needs to be properly modified as well as the limit of either subscript j or subscript k according to the different boundary conditions in the various models considered. For example, along the axis, the symmetry condition requires that $\partial T/\partial r = 0$ and this could be accomplished numerically by equating the temperature T_0 and T_2 and by employing a new combining coefficient of $PA_1^* = PA_1 + PB_1$ rather than the original PA_1 in the first matrix for evaluating the temperature distribution within the pipe. In addition, if the temperature distributions along certain parts of the outer surface of the wall are given, then the

limit of subscript k will be ended with k = kmax-1 rather than k = kmax shown in equation (3-34). The same arguments are also applicable for another subscript j in the axial direction.

By using a similar procedures for the second half of each time step, the finite difference algorithm for the kth row then becomes

$$\left(CP_{j,kk}T_{j-1,kk} + GP_{j,kk}T_{j,kk} + FP_{j,kk}T_{j+1,kk} \right)^{n+1} = PY_{j,kk}^{n+1/2}$$

$$j = 1, 2, \ldots\ldots\ldots jmax$$

$$(3-35)$$

$$\left(CW_{j,kk}T_{j-1,kk} + GW_{j,kk}T_{j,kk} + FW_{j,kk}T_{j+1,kk} \right)^{n+1} = WY_{j,kk,}^{n+1/2}$$

$$j = 1, 2, \ldots\ldots\ldots jmax$$

$$(3-36)$$

where the right hand terms can be computed by

$$PY_{j,kk}^{n+1/2} = \left(-CP_{j,kk}T_{j,kk-1} + HP_{j,kk}T_{j,kk} - AP_{j,kk}T_{j,kk+1} \right)^{n+1/2}$$

$$(3-37)$$

$$WY_{j,kk}^{n+1/2} = \left(-CB_{j,kk}T_{j,kk-1} + HW_{j,kk}T_{j,kk} - AW_{j,kk}T_{j,kk+1} \right)^{n+1/2}$$

$$(3-38)$$

Similarly, to emphasize that the current calculation is in the kth row, we use the symbol kk rather than k in above formula and the matrix form of equation (3-35) for the kth row can then be written as

$$
\begin{pmatrix}
PG_2 & PF_2 & & & & & & * \\
PC_3 & PG_3 & PF_3 & & & & & \\
 & PC_4 & PG_4 & PF_4 & & & & \\
 & & \cdot & \cdot & \cdot & & & \\
 & & & \cdot & \cdot & \cdot & & \\
 & & & & \cdot & \cdot & \cdot & \\
 & & & & PC_{jm-1} & PG_{jm-1} & PF_{jm-1} \\
* & & & & & PC_{jm} & PG_{jm}
\end{pmatrix}_k^{n+1/2}
\begin{pmatrix}
T_2 \\
T_3 \\
T_4 \\
\cdot \\
\cdot \\
\cdot \\
T_{jm-1} \\
T_{jm}
\end{pmatrix}_k
=
\begin{pmatrix}
PY_2 \\
PY_3 \\
PY_4 \\
\cdot \\
\cdot \\
\cdot \\
PX_{jm-1} \\
PX_{jm}
\end{pmatrix}_k^{n+1/2}
$$

$$k = 2, 3 \ldots\ldots\ldots kmid$$

$$(3-39)$$

and the matrix form of equation (3-36) becomes

$$
\begin{pmatrix}
WG_2 & WF_2 & & & & & & * \\
WC_3 & WG_3 & WF_3 & & & & & \\
 & WC_4 & WG_4 & WF_4 & & & & \\
 & & \cdot & \cdot & \cdot & & & \\
 & & & \cdot & \cdot & \cdot & & \\
 & & & & \cdot & \cdot & \cdot & \\
 & & & & WC_{jm-1} & WG_{jm-1} & WF_{jm-1} \\
* & & & & & WC_{jm} & DG_{jm}
\end{pmatrix}_k^{n+1/2}
\begin{pmatrix}
T_2 \\
T_3 \\
T_4 \\
\cdot \\
\cdot \\
\cdot \\
T_{jm-1} \\
T_{jm}
\end{pmatrix}_k^{N+1}
=
\begin{pmatrix}
WY_2 \\
WY_3 \\
WY_4 \\
\cdot \\
\cdot \\
\cdot \\
WX_{jm-1} \\
WX_{jm}
\end{pmatrix}_k^{N+1/2}
$$

$$k = kmid+1, kmid+2 \ldots\ldots\ldots km$$

$$(3-40)$$

As indicated above, the symbol " * " shows that the coefficients in that row as well as the right-hand-side terms need to be properly modified corresponding to the different boundary conditions. The matrix terms in equations (3-29), (3-30), (3-31) and (3-32), (3-35), (3-36), (3-37) and (3-38) can be computed by

$$AP_{j,k} = -(\frac{1}{2}P3 + P4)_{j,k} \qquad EP_{j,k} = (1 - 2*P2)_{j,k}$$

$$BP_{j,k} = (\frac{1}{2}P3 - P4)_{j,k} \qquad FP_{j,k} = -(\frac{1}{2}P1 + P2)_{j,k}$$

$$CP_{j,k} = (\frac{1}{2}P1 - P2)_{j,k} \qquad GP_{j,k} = (1 + 2*P2)_{j,k}$$

$$DP_{j,k} = (1 + 2*P4)_{j,k} \qquad HP_{j,k} = (1 - 2*P4)_{j,k}$$

$$(3-41)$$

and

$$AW_{j,k} = -(\frac{1}{2}W3 + P4)_{j,k} \qquad EW_{j,k} = (1 - 2*P2)_{j,k}$$

$$BW = (\frac{1}{2}W3 - W4)_{j,k} \qquad FW_{j,k} = -(\frac{1}{2}W1 + W2)_{j,k}$$

$$CW_{j,k} = (\frac{1}{2}W1 - W2)_{j,k} \qquad GW_{j,k} = (1 + 2*W2)_{j,k}$$

$$DW_{j,k} = (1 + 2*W4)_{j,k} \qquad HW_{j,k} = (1 - 2*W4)_{j,k}$$

$$(3-42)$$

In order to rewrite the equation in a simple form we define the following linear operator :

$$LY \, [P]_{j,k} = [BP, \, DP, \, AP]_{j,k}$$

$$LY \, [W]_{j,k} = [BW, \, DW, \, AW]_{j,k}$$

$$(3-43)$$

$$LX \, [P]_{j,k} = [CP, \, GP, \, FP]_{j,k}$$

$$LX \, [W]_{j,k} = [CW, \, GW, \, FW]_{j,k}$$

and column vectors

$$\{TY\}_{j,k} = \{T_{j,k-1}, \, T_{j,k}, \, T_{j,k+1}\}$$

$$(3-44)$$

$$\{TX\}_{j,k} = \{T_{j-1,k}, \, T_{j,k}, \, T_{j+1,k}\}$$

Equations (3-29) which are in the radial direction can be simply written as

$$LY \, [P]_{j,k}^{n} \, \{TY\}_{j,k}^{n+1/2} = PX_{j,k}^{n} \qquad (3-45)$$

$$LY \, [W]_{j,k}^{n} \, \{TY\}_{j,k}^{n+1/2} = WX_{j,k}^{n} \qquad (3-46)$$

$$j = 1, \, 2, \, \ldots\ldots\ldots$$
$$k = 1, \, 2, \, \ldots\ldots\ldots$$

Equations (3-33) and (3-34), which are in the axial direction, then assume the following simple forms:

$$LX \, [P]^{n+1/2}_{j,k} \, \{TX\}^{n+1}_{j,k} = PY^{n+1/2}_{j,k} \qquad (3-47)$$

$$LX \, [W]^{n+1/2}_{j,k} \, \{TX\}^{n+1}_{j,k} = WY^{n+1/2}_{j,k} \qquad (3-48)$$

$$j = 1, 2, \ldots\ldots\ldots$$
$$k = 1, 2, \ldots\ldots\ldots$$

where the right side terms can be estimated by

$$PX_{j,k} = (-CP, \, EP, \, -FP)_{j,k} \, \{TX\}_{j,k}$$

$$WX_{j,k} = (-CW, \, EW, \, -FW)_{j,k} \, \{TX\}_{j,k}$$

$$\qquad\qquad\qquad\qquad\qquad\qquad\qquad\qquad (3-49)$$

$$PY_{j,k} = (-BP, \, HP, \, -AP)_{j,k} \, \{TY\}_{j,k}$$

$$WY_{j,k} = (-BW, \, HW, \, -AW)_{j,k} \, \{TY\}_{j,k}$$

It is seen, as the result of the ADI "splitting" procedure which has been employed in the algorithm associated with different boundary conditions for the various models, that only a tridiagonal system of linear algebraic equations needs to be solved (i.e., during step 1, the coupled tridiagonal matrix (3-33), (3-34) are solved for each jth column of the grid points, while during step 2, the coupled tridiagonal matrix (3-39) and (3-40) are then solved for each kth row of grid points).

Once the periodic steady solution has been obtained, we can calculate both the tidal displacement and the heat flux at different locations within the pipe. The numerical technique used here to integrate equations (2-38), (2-39) and (2-41) for evaluating the tidal displacement and the heat flux at each specified location can be obtained either by the Trapezoidal rule (with end correction) or Simpson's rule. Both numerical approaches are essentially fourth-order methods.

Convergence Criteria

As is known, once the calculation work has started, the time-matching process will be in the loop forever unless a criterion can be derived that indicates when the goal of the current computing work has been reached and further solution-matching processes do not produce significant increases in accuracy. Such a criterion depends on the purpose of the calculation. If one's goal is to study the

transient process, one can indicate a time limit to pause or quit the current computing work.

However, if one seeks a final periodic state solution, one has to develop a criterion to test if the solution can be considered acceptable.

It seems that the temperature is a good measure of the accuracy of the overall solution process so that the most efficient way is to apply the convergence test on the temperature rather than on the velocity. For the present purpose, two convergence criteria were alternatively used. The choice of the criterion depends on what was the main goal in the particular study case. If the main effort is to observe the distribution of the quasi-steady temperature at any phase angle ωt within a period, the testing is done by comparing the temperature residual, i.e., by inspecting the averaged temperature difference of each nodal point at thee same ωt between adjacent periods. This can be written as

$$Res1 = \frac{\left[\Sigma \ (T11 - T22 \ )^2_{j,k} \right]^{1/2}}{(JMAX)(KMAX)} \qquad \leq \epsilon_1$$

$$j = 1, 2, \ldots\ldots.JMAX$$

$$k = 1, 2, \ldots\ldots.KMAX$$

(3-50)

where $T11_{j,k}$ is the value of the temperature of node (j,k) at ωt in the current period, $T22_{j,k}$ is the value of the

temperature of node (j,k) at the same ωt in the previous period, and ϵ_1 is the convergence parameter.

If the goal of the investigation is to examine the effective heat transfer, the convergence criterion is established by computing the residual

$$\text{Res2} = \frac{\left[\Sigma \, (\phi1 - \phi2)_j^2 \right]^{1/2}}{\text{JSEC}} \leq \epsilon_2 \qquad (3\text{-}51)$$

$$j = 1,2,\ldots\ldots\text{JSEC}$$

where JSEC is the number of cross-sections where the axial heat flux was examined, ϵ_2 is the convergence parameter, and $\phi1$, $\phi2$ are the cross-section averaged heat flux in the current period and previous period, respectively. The summation is carried out over all sections (JSEC) where the heat flux is computed.

The value of the convergence parameter can be determined by a balance of the acceptable solution accuracy and the cost of CPU time. In the current study both $\epsilon1$ and $\epsilon2$ were taken between 0.001-0.01 as the residual of the temperature or the heat fluxes for acceptable value.

Grid Generation

As is well known, the solution accuracy and efficiency in a large degree depends on the grid system used in the numerical calculation. A good grid is characterized by small skewness, high smoothness and capability of high

resolution in the large gradient regions in the physical plane. It has been shown that rapid changes of grid size and highly skewed grids can result in undesirable errors [25]. The success of a numerical simulation of a complex thermal fluid dynamics problem does depend strongly upon the grid system used in the computation.

In the present study, the grid mesh was generated with the emphasis on the high resolution capability of its simple geometric boundaries. The technique used here is one of the algebraic schemes which cluster the grid lines near the region desired [34], namely,

$$\Delta S_k = \Delta S_o (1 + \epsilon)^{k-1} \qquad (3-52)$$

where ΔS_o is the minimum specified grid spacing next to the wall or to some inner interfaces within the tube. The parameter ϵ is determined by a Newton-Raphson iteration process so that the sum of the above increments matches the known arc length between $k = 1$ and $k = kmax$. The grid networks used in Model 1 and Model 2 are uniformly distributed along the axial direction in both the fluid and the wall; however, in Model 3, most grid points are clustered near the central portion of the pipe so as to gain higher resolution in the region of interest, while along the radial direction a non-uniform grid was employed in all three models. The minimum specified grid spacing ΔS_o used

depends on the boundary layer thickness δ, namely, the kinematic viscosity of working fluid and the oscillating frequency. In the present study, it was found that a good choice of this value is $\Delta S_O = 0.05\delta$ for laminar flow cases with a total of about 15-20 nodal points distributed along the radius.

CHAPTER IV
NUMERICAL RESULTS AND DISCUSSION

The problem of time-dependent enhanced heat conduction subjected to sinusoidal oscillations can now be solved numerically for the boundary conditions appropriate to a long capillary tube according to the various models described in previous chapters. The computational tasks fall into two catagories: the first part is a numerical study concerned with the characteristics of the oscillatory pipe flow, which includes an investigation of the velocity profiles, the Lagrangian and the tidal displacement trajectories. The second part of this study includes a thorough investigation of the final periodic state temperature build-up process in oscillating pipe flow, the periodic temperature distribution in the pipe and wall, and a study of the relationship between the enhanced axial heat flux and the tidal displacement. It also includes an investigation of the tuning effect and a comparison of the enhanced axial heat transfer with the corresponding pure molecular axial heat conduction as well as the investigation of the influences of the pipe radius and the wall thickness on the enhanced axial heat transfer.

Properties of oscillating laminar pipe flow have been analytically discussed by S. Uchida [36] for several different Wormersley numbers, and these results offer a useful reference for comparing with the present numerical studies. However, in the area of thermal fields associated with enhanced thermal pumping there is little information available for comparison, except for some recent results of Kaviany [13].

The present computational work was carried out on the Vax-11/750 computer in the Department of Aerospace Engineering, Mechanics, and Engineering Science, and on the Vax-11/780 in the Center for Instructional and Research Computing Activities, University of Florida, Gainesville, Florida. Note that it is very time-consuming to build-up a final periodic state, for example, if the grid size is 101×22 and the time steps are 2000 per period, it takes 7.5 minutes (CPU) with the VAX-11/780 machine or almost 1 hour (CPU) with the VAX-11/750 machine to run only one period. It usually takes 20-30 periods to reach the final periodic state solution.

The process of selecting model size (i.e., total nodal points) is a synthetic balance among the storage requirement, the solution accuracy, and the cost of CPU time for finding an acceptable solution. Such a selection allows each case to be solved with a minimum of expense in computing operation thereby making it possible to do the

large number of runs needed to obtain enough data points to plot curves of the desired parameters.

The results discussed in this chapter are presented for the purpose of illustrating the effects to be encountered in working with the enhanced thermal pump. These results should be effective in gaining insight into some interesting features of this enhanced heat transfer process. Since the analytic approximations [15, 16, 18, 22] are effective in describing the flow and the heat transfer aspects and to give considerable insight into the problem, they are often used to compare with the numerical results and should give good agreement when applicable.

Part 1.   Oscillatory Pipe Flow Features

In order to better understand the mechanism of the enhanced thermal pump, it is necessary to examine the mechanical features of the oscillating pipe flow.   As mentioned in previous chapters, the present interest in the enhanced thermal pumping is confined to an investigation of the central part of the slender pipe, thus the flow field can be well approached by a 1-D time-dependent laminar model which neglects the ends effects.

Velocity Profiles

Fig. 4-1 shows the numerically computed time-dependent velocity profiles at different phase angles of the exciting pressure when Wormersley numbers are equal to 1, 10, 100, and 1000, respectively. It can be clearly seen

α = 1

α = 10

α =100

α =1000 .

ωt =   0   30   60   90   120   150   180   210   240   270   300   330   360
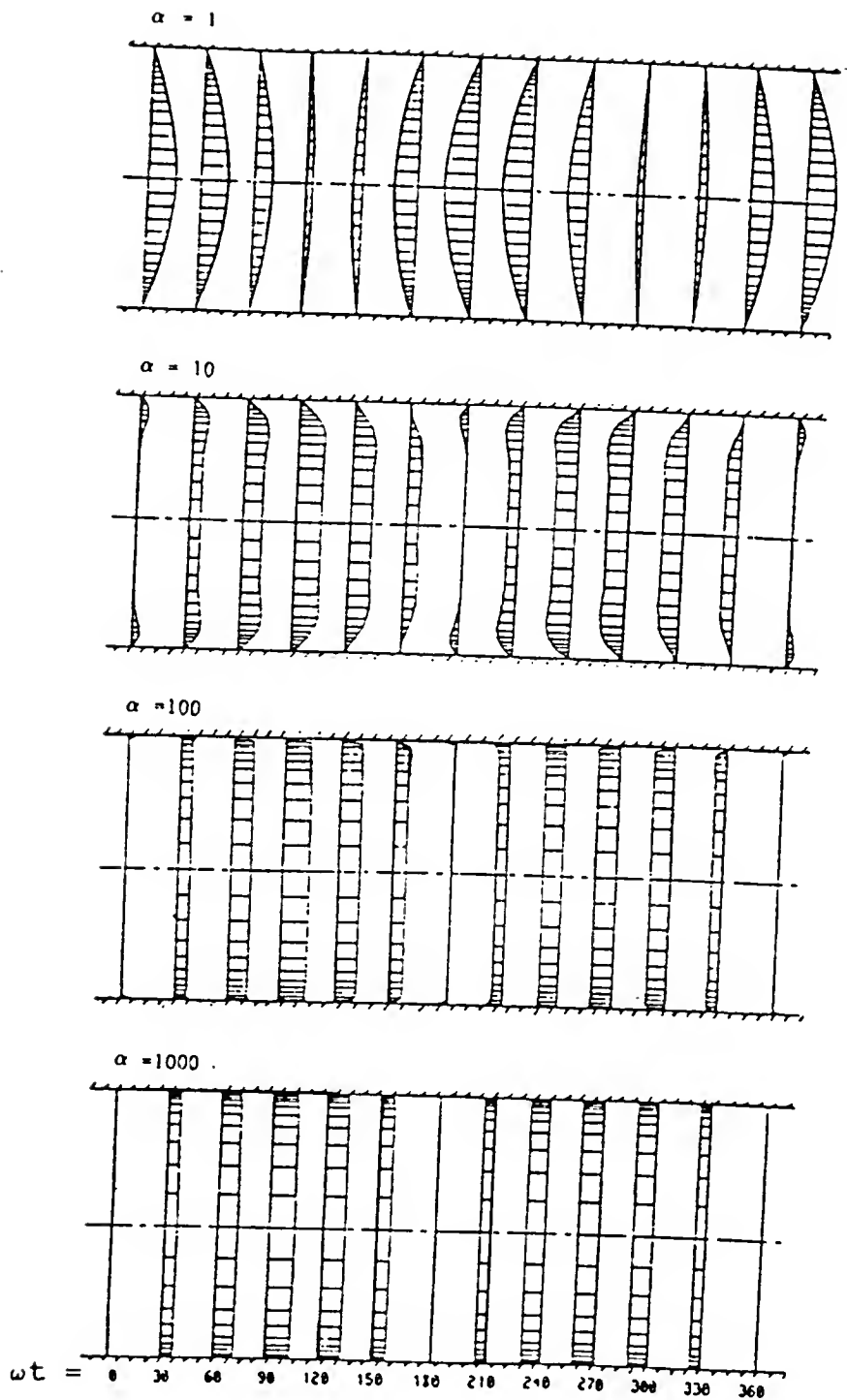
Fig 4-1   1-D Velocity Profiles in Oscillating Flow
         for Wormersley Number α = 1, 10, 100 and 1000

that the velocity profile at α = 1 presents a quasi-parabolic shape at any instant within a period and is in phase with the stimulating pressure gradient. However, at higher frequency, for example, α = 100 and 1000, the velocity profiles can be clearly separated into two regions: in the vicinity of the wall the flow shows a typical thin boundary layer, while in the region far away from the wall the fluid moves as if it were frictionless slug flow. In fact, within this core region the velocity distribution is independent of the distance from the wall [29]. It can be also seen that the phases of the velocity profiles at higher frequencies cases are shifted about $\pi/2$ with respect to the
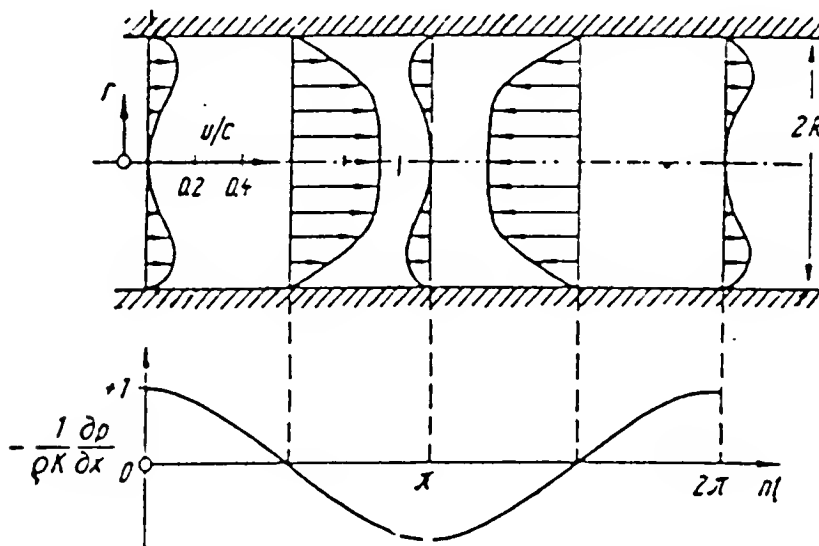
Fig 4-2 Velocity Profile (α=5) [29]
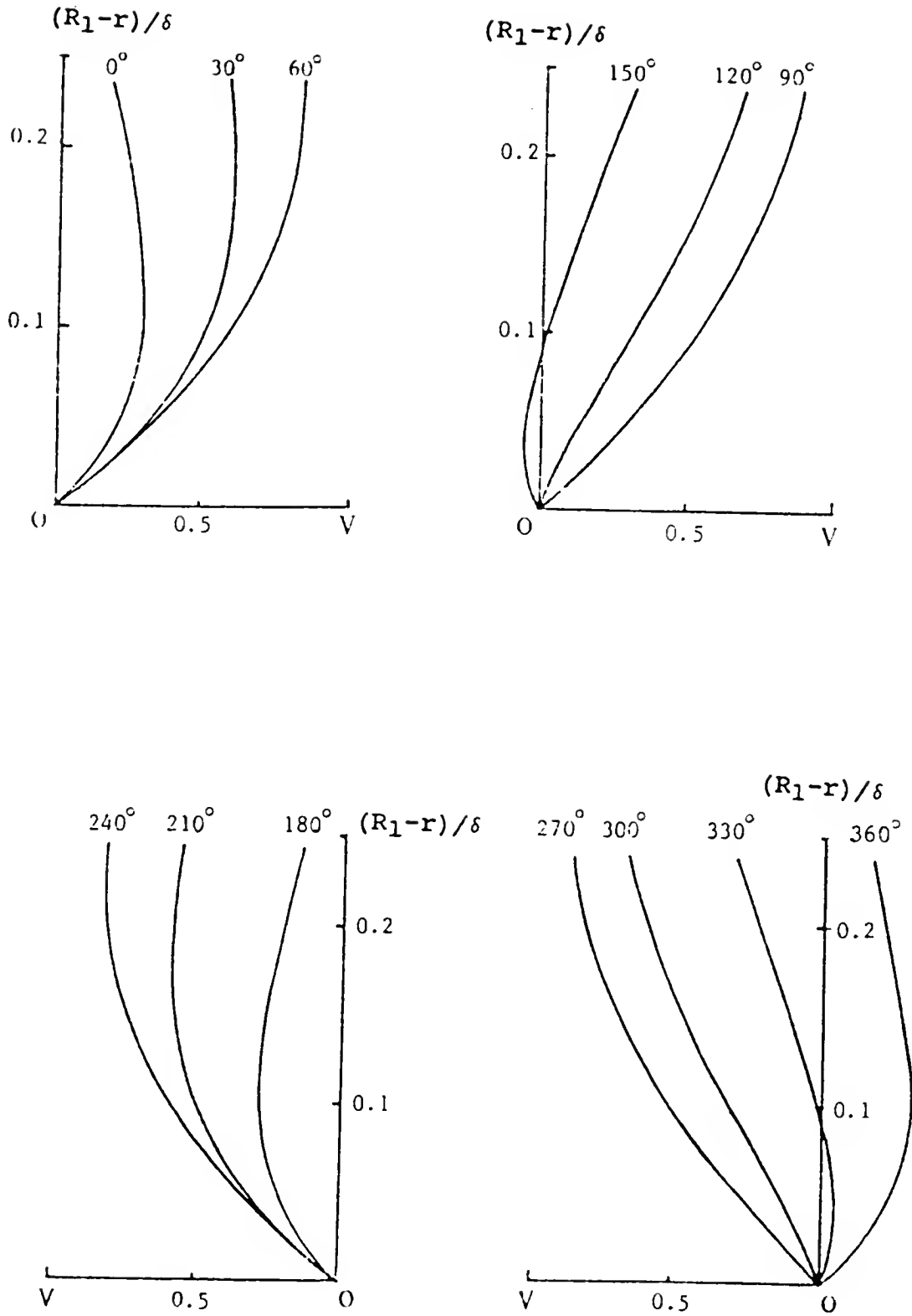
Fig 4-3   Magnified View of Velocity Profile Near Wall
(Wormersley Number $\alpha=10$, H_2O, $\delta=0.014$cm)

stimulating pressure gradient. At the intermediate frequency case (α = 10 of Fig. 4-1), the slug flow boundary is not so evident, but one can still note a boundary layer near the wall. The same pattern of the velocity profiles associated with moderate Wormersley numbers can also be found in the reference [36] where the velocity profile at Wormersley number α less than 10 was presented (Fig. 4-2). In order to better see the variation of the time-dependent velocity profile within the boundary layer, a set of closer view of the velocity profile with respect to Wormersley number at α = 10 during phase intervals ωt = 30° is plotted in Fig. 4-3.

It should be emphasized that the solutions shown here are under the assumption that the secondary velocity in the radial direction is negligible compared to the axial velocity component, namely, the non-linear inertial terms are not considered in the governing equation (2-1). This is a reasonable approximation for moderate oscillatory frequency ω except near the ends of the pipe. However, at high Wormersley numbers, care should also be taken to avoid violating another assumption, namely, that of incompressibility and the concomitant condition that the oscillating phase does not change between the tube ends. High Wormersley number can be obtained either by increasing the oscillating frequency ω or by increasing the pipe diameter for a given fluid. An oscillating flow can be

considered incompressible if $\Delta x \omega / 2 < 0.05C$, where C is the speed of sound in the fluid. For mercury, C = 1360 m/sec, one requires $\alpha = 27.1$, when $\Delta x = 20$ cm and $R_1 = 0.1$ cm. To avoid a appreciable phase difference between the tube ends, one requires that $L/C << 2\pi/\omega$. Both the restrictions are met in the examples to be considered below.

The Lagrangian Displacements

An alternative interesting representation to the oscillatory velocity field are the Lagrangian displacements of the fluid elements at different radii within the pipe. They have been plotted in Figs. 4-4 and 4-5 at time intervals of $\omega t = 30°$ for Wormersley number $\alpha = 0.1$, 1.0 and 10. It is noted that since both pipe diameter and the working fluid were fixed in this test, Figs. 4-4 and 4-5 represent the relationship between the Lagrangian displacement and the oscillating frequency. The trajectories plotted in Figs. 4-4 and 4-5 have been normalized by A/ω^2, where $A = 1/\rho |dp/dx|$ is the amplitude of the sinusoidal pressure gradient as defined in equation (2-1) and ω is the angular velocity. Suffice it here to point out that for the lower frequency case (for example $\alpha = 0.1$ and 1.0) the Lagrangian displacement trajectory shows a foreseeable parabolic pattern at any moment. Nevertheless, the essential distinction between low frequency oscillatory pipe flow and steady Hagen-Poiseuille flow is that in the former, the Lagrangian displacement trajectories as well as
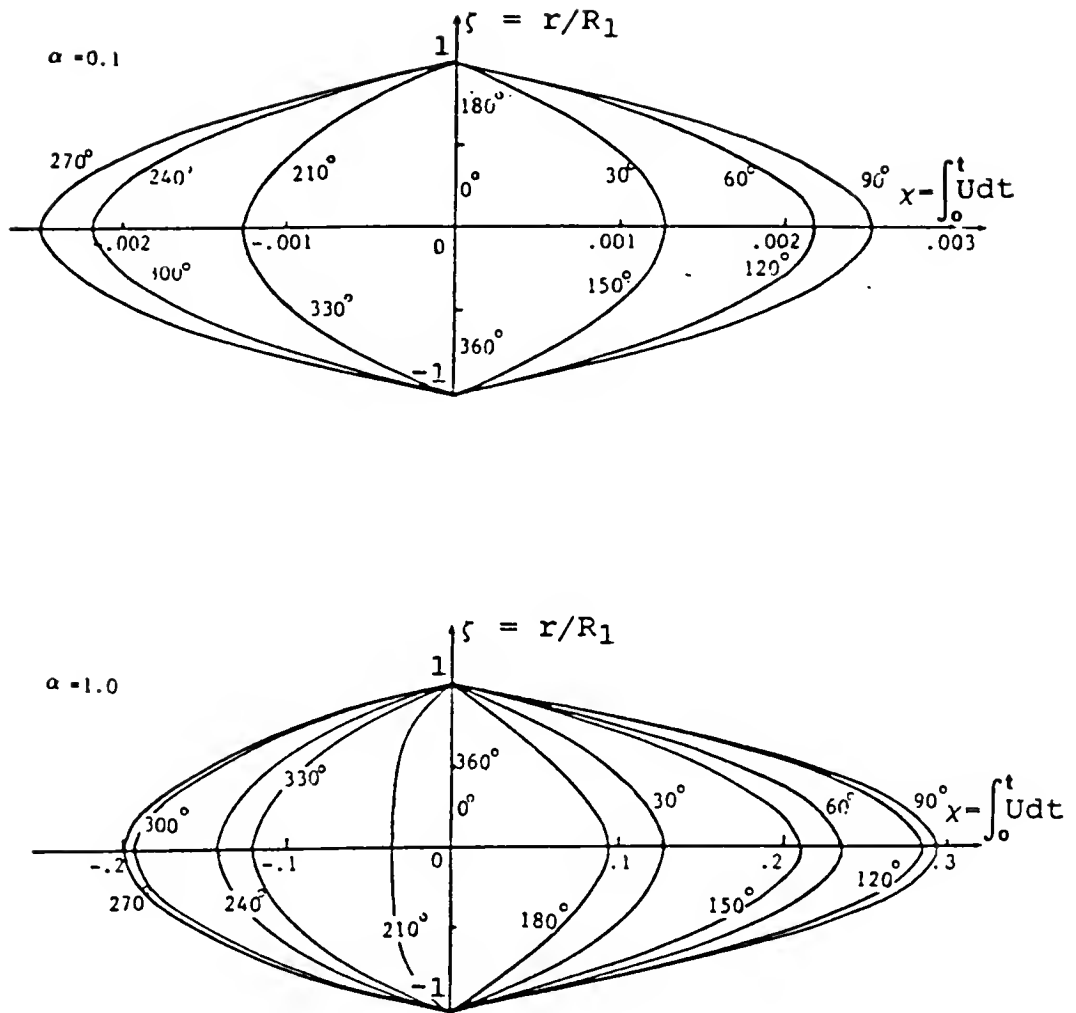
Fig 4-4   Lagrangian Displacement for α = 0.1 and 1.0
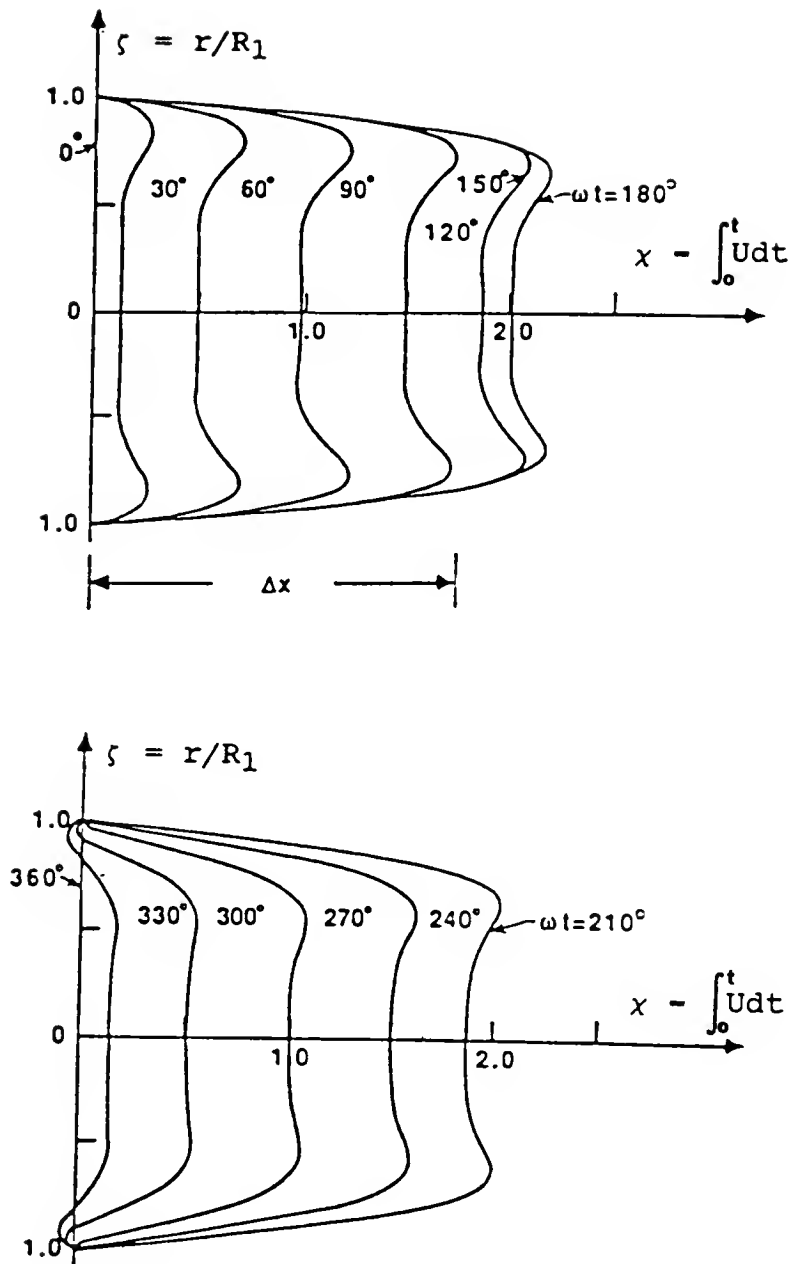
Fig 4-5   Lagrangian Displacement at $\alpha = 10$

the velocity profiles are periodic so that the fluid particles do not translate axially upon time averaging, while in the later case they will.

For intermediate Wormersley number (α = 10), the trajectories of the Lagrangian displacement departs considerably from the standard parabolic shape. This phenomenon can be even more clearly seen in the α = 100 case. Evidently, the higher the oscillating frequency, the thinner the boundary layer ($\delta = \sqrt{2\nu/\omega}$).

Tidal Displacements

Figs. 4-6 and 4-7 demonstrate time variation of the cross-section averaged dimensionless Lagrangian displacement at Wormersley numbers in the range from α = 0.1 to 50. The tidal displacement can be obtained by summing the absolute maxima and the absolute minima of these curves. The corresponding non-dimensional tidal displacements with respect to Wormersley number from α = 0.1 to α = 12 are listed in table 4-1 below

Table 4-1   Dimensionless Tidal Displacement at Different Wormersley Numbers

α	0.1	1.0	2.0	3.0	4.0	5.0
ΔX	0.00246	0.14295	0.67303	1.20213	1.41160	1.49041
α	6.0	7.0	8.0	10.0	12.0	
ΔX	1.56294	1.61879	1.66046	1.71900	1.76698	
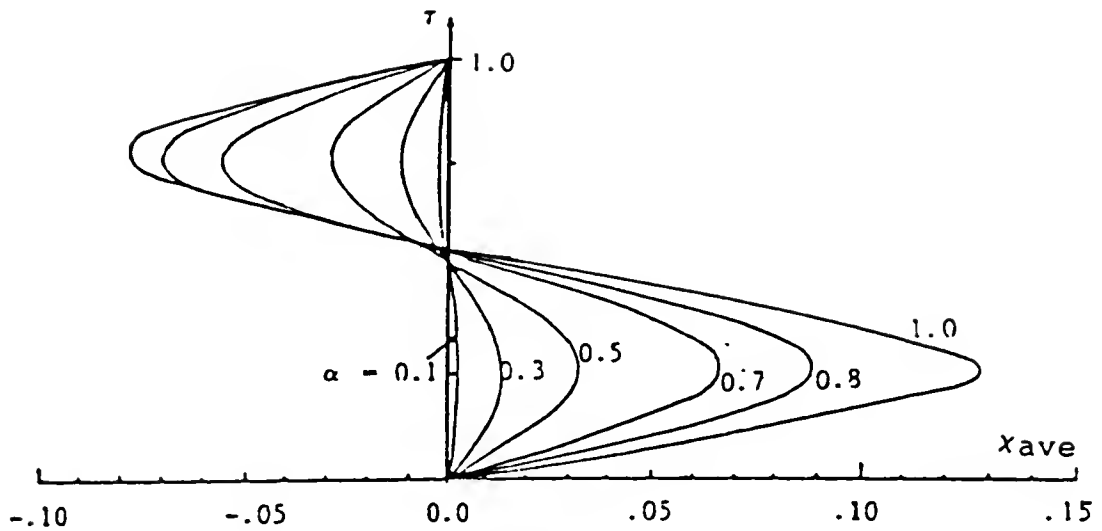
Fig 4-6   Dimensionless Cross-section Averaged
Displacement Versus Time
$\alpha = 0.1 - 1.0$
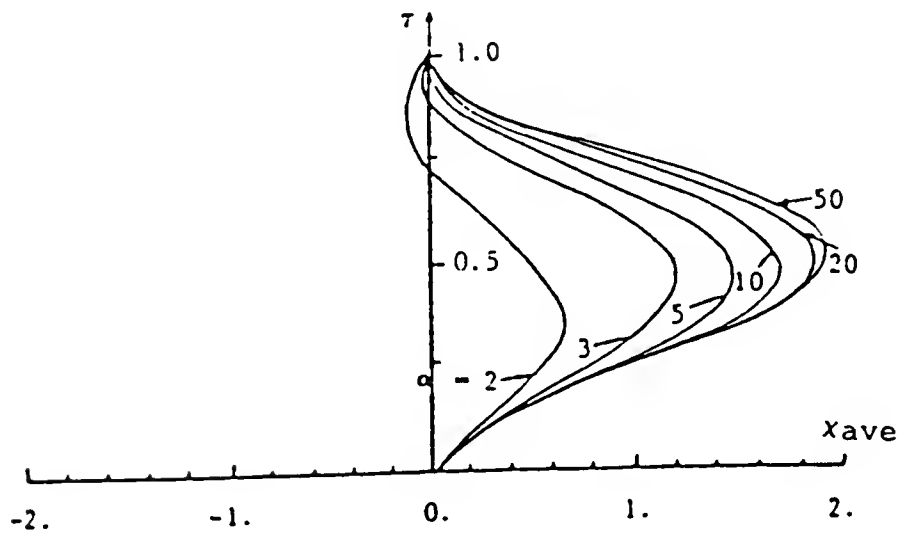
Fig 4-7   Dimensionless Cross-section Averaged
Displacement Versus Time
$\alpha = 2 - 50$

It is noticed that for very small Wormersley number cases ($\alpha \leq 0.5$), the cross-section averaged displacement varies like a sinusoidal function with respect to time (the ordinate), and as Wormersley number increases, the cross-section averaged displacements are no longer symmetric about the ordinate but rather favor positive values of χ. If the Wormersley number is further increased, eventually, the cross-section averaged displacement almost entirely lies on the right half plane. A similar feature can also be seen in Figs. 4-4 and 4-5. In fact, this just again shows the existence of the phase shift in the oscillating pipe flow. When the Wormersley number is small the cross-section averaged displacements as well as the Lagrangian displacements show a sinusoidal variation with respect to time and this has $\pi/2$ phase lag with respect to the stimulating pressure gradient which is assumed to be a cosine function of ωt with zero initial phase angle. However, for higher Wormersley number, the phase lags increase to almost π with respect to the phase of the exciting pressure gradient. Note that the Lagrangian displacements in Figs. 4-4 and 4-5 were computed by lining up all the fluid particles on the plane $x = 0$ at $\omega t = 0$, however, by using non-zero velocity at $\omega t = 0°$ as shown in Fig. 4-1. This implies that if the phase of the exciting pressure gradient is taken as the base of the measurement, it is generally not possible to assure the same phase to the

velocity and Lagrangian displacement as well as the tidal
displacement. For example, at phase of the stimulating
pressure gradient $\omega t = 0°$, the corresponding velocity phase
may be $\pi/2$ and the Lagrangian displacement phase may be π.
In fact, this is just as true for very high Wormersley
numbers; however, the phase difference with respect to the
exciting pressure gradient phase is less than the value
shown above for low Wormersley number. One can well see
that if the phase lags of the Lagrangian displacement or the
tidal displacement is given, one can certainly re-draw the
diagram shown in Figs. 4-6, 4-7 by lining up the phase with
itself, and then an exact symmetric pattern of the tidal
displacement curve similar to that in the very small
Wormersley number case can be obtained. Unfortunately, the
phase lags are a function of the Wormersley number and they
are not known in advance.

In order to verify the numerical method used in this
study and to check the ETP code developed, a comparison of
the computed dimensionless tidal displacement to the one
using the analytic equations (1-7) and (1-8) given by
Kurzweg [18] for Wormersley number varying from 0.1 to 100
has been calculated and plotted in Fig. 4-8. The solid line
shows the analytic solution obtained by use of equations (1-
7) and (1-8), while the dashed line shows the results with
the ETP code developed in this study. The agreement is
quite good, particularly when the Wormersley is less than

3.0. However, at high Wormersley number the numerical solution shows a very slight deviation from the analytic solution. This deviation is believed due to an inaccurate numerical integration over the cross-section using relatively large time steps (our time steps per period in the calculation were between 1000-2500). A comparison with using 10^4 time steps per period for Wormersley number $\alpha = 10$ was studied and shows some improvement. However, using such small time steps in the present investigation is beyond the capacity of the current VAX computer facility used. The numerical error becomes particularly serious as the oscillating frequency becomes large where the extremely thin boundary layer requires more grid nodal points to resolve the flow variables in the vicinity of the wall.

Fig. 4-8 shows that as the Wormersley number gets large, the dimensionless tidal displacement tends to the limit of 2.0, which agrees with the limit of 1.0 in the analytical solution given by Kurzweg [18] for the reason that the normalization parameter used in [18] is twice as large as that in the present numerical simulation.

Fig. 4-9 shows the required stimulating axial pressure gradient used in the present study for a pipe radius $R_1 = 0.1$ cm and water ($\nu = 0.01$ cm^2/sec) taken as the working medium versus the dimensional tidal displacement Δx in cm for various Wormersley numbers (namely, oscillating frequency). It is evident from these results that for fixed
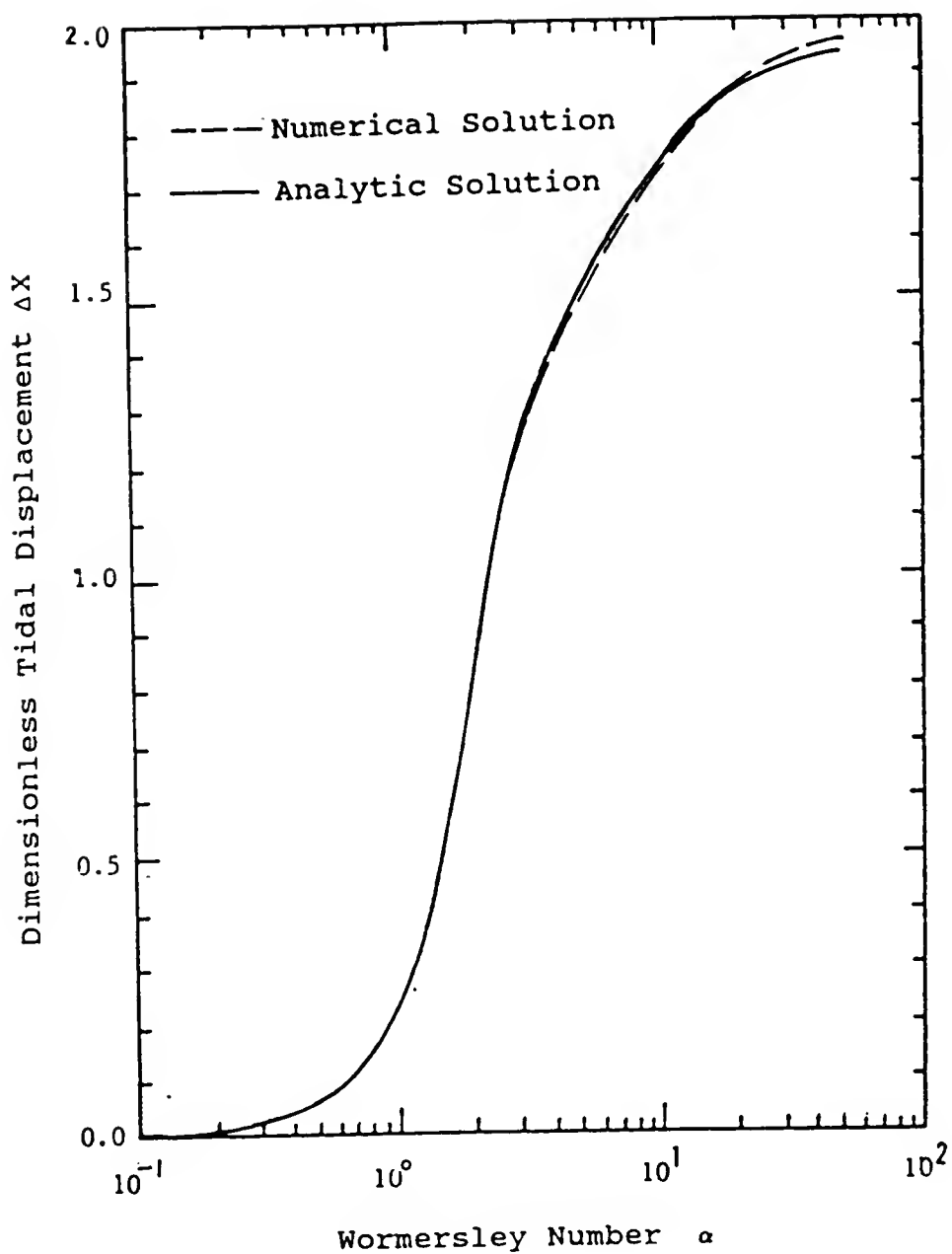
Fig 4-8   Relationship Between Dimensionless Tidal
Displacement ΔX and Wormersley Number α
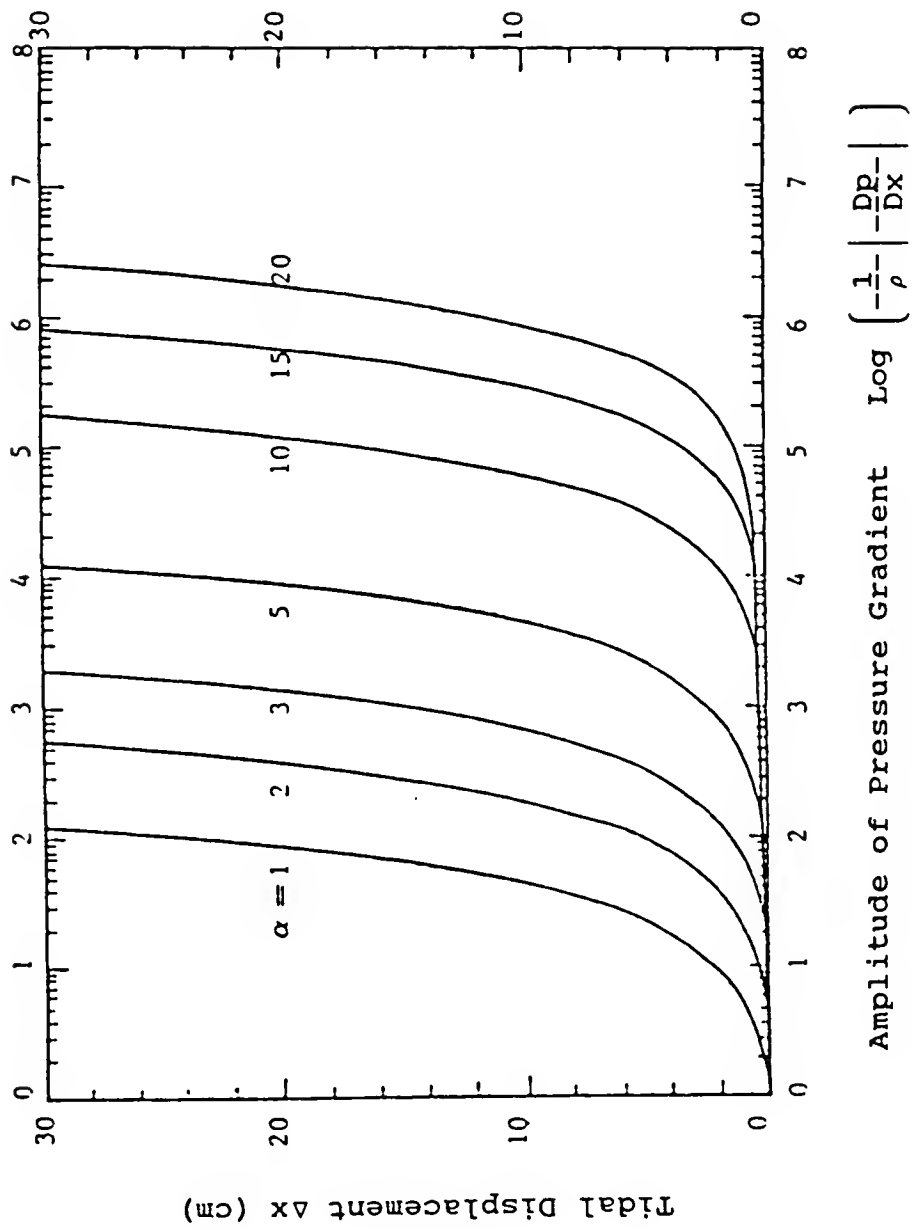
Fig 4-9   Relationship Between Tidal Displacement Δx
           and Exciting Pressure Gradient in Water

tidal displacement, the required axial pressure gradient in the large Wormersley number case is orders of magnitude higher than that in the small Wormersley number case. This may eventually put some constraint on the use of very high frequency in the enhanced heat transfer technique. Fortunately, to meet the tuning condition, the required Wormersley number in this case is of order 1. As already discussed in the introduction, in order to gain the benefit of axial heat transfer, the use of large tidal displacement is always preferred. However, such an increase must be limited by the requirement of no convective net mass transfer occurring between two reservoirs and may also be constrained by the ability of the device to withstand the increase in the exciting pressure gradient.

Phase Lags

We are now in the position to study the phase lags of the Lagrangian displacement in the oscillatory pipe flow. Fig. 4-10 shows the phase variations (in degrees) along radius for Wormersley number varying from $\alpha = 0.1$ to 4. Some numerical results are also shown in Tables 4-2 and 4-3. All of the data shown in Fig. 4-10 and the tables have the phase angle measured relative to the exciting pressure gradient. Two features can be seen in Fig. 4-10; first, in the core portion, the phase lags are almost equal to $\pi/2$ when the Wormersley number is small, while the lags are almost π when the Wormersley number is large, and second,

the phase lags vary along radius, especially in the boundary
layer. It is such phase lags that allow the existing
temperature gradient in the very thin boundary layer of the
oscillating pipe flow to act as region of temporary heat
storage. It absorbs heat when the temperature of the core

Table 4-2　　　　　　　Phase Lags Along Radius
(Working Medium: H_2O, Δx = 10 cm)

Nodal point K	$\alpha = 0.1$		$\alpha = 1.$		$\alpha = 2.$	
	η=r/R1	phase	η=r/R1	phase	η=r/R1	phase
1	0.0000	90.63	0.0000	102.06	0.0000	134.28
2	0.1667	90.63	0.0366	102.06	0.1095	134.10
3	0.3333	90.63	0.0957	102.06	0.2164	133.38
4	0.5000	90.63	0.1913	101.88	0.2836	132.66
5	0.5833	90.63	0.2593	101.70	0.3620	131.76
6	0.6667	90.63	0.3458	101.52	0.4535	130.50
7	0.7500	90.63	0.4559	101.16	0.5603	128.70
8	0.8333	90.63	0.5958	100.62	0.6849	126.00
9	0.9167	90.63	0.7737	99.72	0.8303	122.58
10	1.0000	0.00	1.0000	0.00	1.0000	0.00

Table 4-2 -- continued

Nodal point K	$\alpha = 3$		$\alpha = 4$		$\alpha = 7$	
	$\eta=r/R1$	phase	$\eta=r/R1$	phase	$\eta=r/R1$	phase
1	0.0000	170.83	0.0000	179.82	0.0000	181.62
2	0.0917	170.47	0.1242	179.28	0.0970	181.62
3	0.1818	169.75	0.2370	178.02	0.1892	181.62
4	0.2703	168.31	0.3395	176.04	0.2769	181.44
5	0.3573	166.51	0.4324	173.70	0.3604	180.72
6	0.4427	164.00	0.5168	171.00	0.4397	179.28
7	0.5267	161.12	0.5935	168.12	0.5152	177.12
8	0.6091	157.88	0.6630	165.24	0.5869	174.06
9	0.6901	154.64	0.7262	162.18	0.6552	170.28
10	0.7696	150.69	0.7835	159.12	0.7201	165.78
11	0.8478	146.73	0.8356	156.06	0.7818	160.74
12	0.9246	142.42	0.8828	153.18	0.8406	155.16
13	1.0000	0.00	0.9257	150.30	0.8964	149.04
14			0.9646	147.60	0.9495	142.56
15			1.0000	0.00	1.0000	0.00

Table 4-2 -- continued

Nodal Point K	$\alpha = 10$		$\alpha = 14$		$\alpha = 20$	
	$\eta = r/R1$	phase	$\eta = r/R1$	phase	$\eta = r/R1$	phase
1	0.0000	180.54	0.0000	179.46	0.0000	179.10
2	0.0884	180.72	0.0834	179.10	0.1635	180.54
3	0.1740	181.08	0.1647	180.18	0.3032	185.93
4	0.2566	181.80	0.2440	184.50	0.4227	182.34
5	0.3364	182.52	0.3215	190.25	0.5247	186.65
6	0.4135	182.70	0.3970	192.41	0.6120	184.14
7	0.4880	181.80	0.4709	189.53	0.6865	184.14
8	0.5599	179.64	0.5428	183.06	0.7502	181.98
9	0.6295	175.68	0.6130	174.07	0.8046	178.38
10	0.6966	170.46	0.6815	164.00	0.8512	173.71
11	0.7616	163.80	0.7484	153.20	0.8909	167.95
12	0.8243	156.06	0.8136	141.70	0.9249	161.12
13	0.8849	147.24	0.8773	130.19	0.9540	153.57
14	0.9434	137.52	0.9394	118.32	0.9788	146.01
15	1.0000	0.00	1.0000	0.00	1.0000	0.00

Table 4-3   Comparison of Phase Lags With Different
Working Mediums ($\Delta x = 10$)

| Nodal Point K	$\alpha = 1.$			$\alpha = 5.$		
	$\eta = r/R1$	Phase Lags		$\eta = r/R1$	Phase Lags	
		Water	Mercury		Water	Mercury
1	0.0000	102.06	102.14	0.0000	181.62	181.62
2	0.0161	102.06	102.14	0.0714	181.44	181.26
3	0.0366	102.06	102.14	0.1429	180.90	180.54
4	0.0626	102.06	102.14	0.2143	179.64	179.46
5	0.0957	102.06	102.14	0.2857	178.02	178.02
6	0.1378	101.88	102.14	0.3571	176.04	175.86
7	0.1912	101.88	102.14	0.4286	173.34	173.37
8	0.2593	101.70	102.14	0.5000	170.28	170.11
9	0.3458	101.52	101.78	0.5714	166.50	166.51
10	0.4559	101.16	101.42	0.6429	162.18	162.20
11	0.5957	100.62	101.06	0.7143	157.50	157.52
12	0.7737	99.72	99.98	0.7857	152.10	152.13
13	0.0000	0.00	0.00	0.8571	146.16	146.37
14				0.9286	139.86	139.90
15				1.0000	0.00	0.00
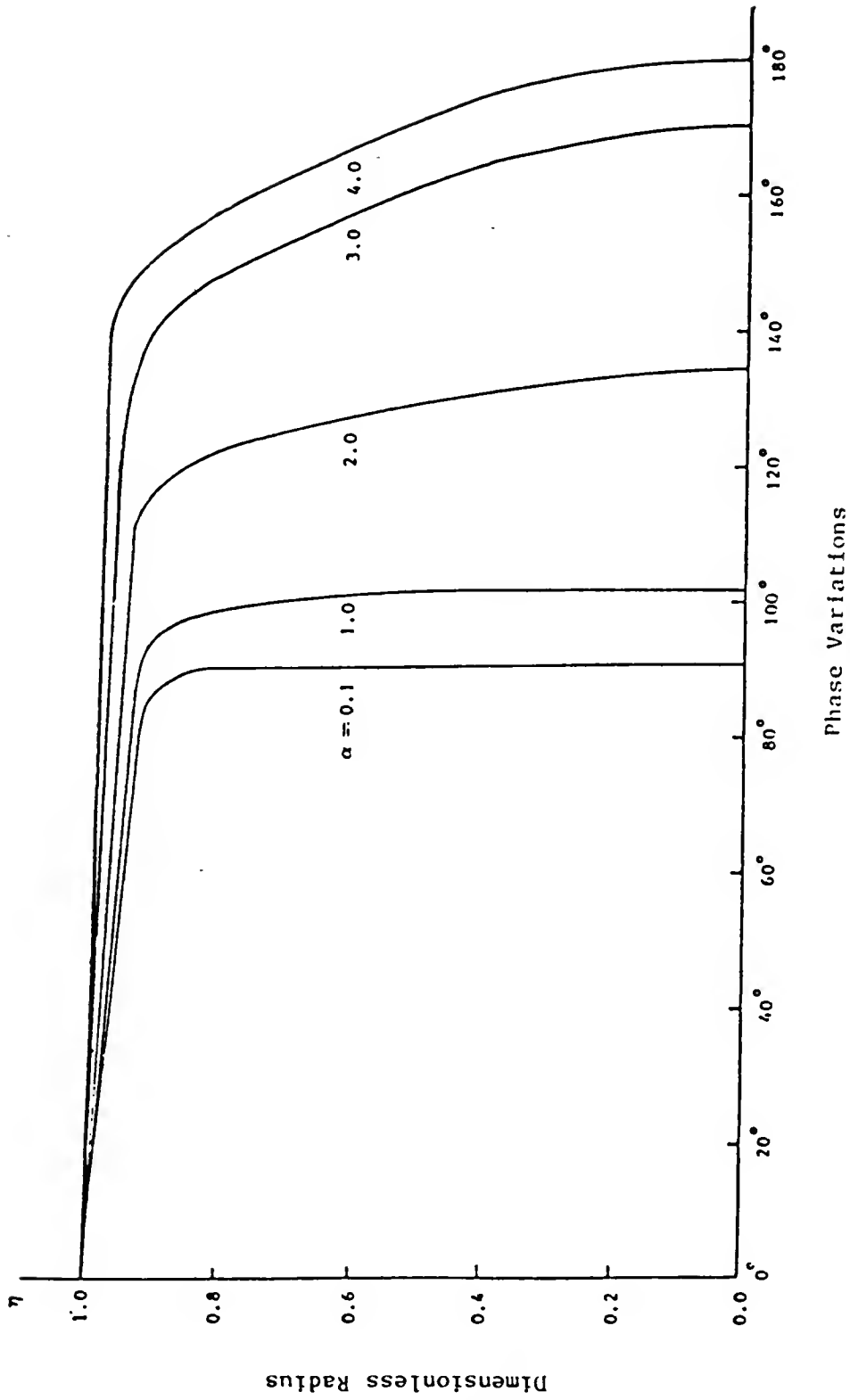
Fig 4-10   Phase Variation Along Radius
for Different Wormersley Numbers

slug flow is higher than that of the boundary layer, and it releases heat as the core temperature is relatively lower. This large temperature gradient enhanced by the existing velocity phase lags allows a large amount heat to be conductively transferred radially within a very short time and subsequently to be transferred axially by a convective coupling.

Part 2. The Enhanced Heat Transfer Investigation

We have examined some mechanical characteristics in oscillating pipe flow, and compared the computed solution of the velocity field with Uchida's solution. The results for the velocity profiles are in good agreement. Nevertheless, before a detailed examination of the thermal field, it is first necessary to test the current developed ETP code when applying the temperature equations (2-6),(2-7). It is seen that the energy equations strongly depend on the velocity distribution and its build-up process, so that one can use analytic periodic velocity state (Eqs. 1-4 and 1-5, with no build-up process), and the computed velocity (with build-up process) to verify the correctness of the resulting thermal variables. The enhanced heat flux is a function of both velocity and temperature (Eqs. 2-34 and 2-35) and was chosen for a comparison of the analytic and numerical results of the problem. Part A of table 4-4 shows the results of the computed enhanced axial heat flux as well as the axial conduction heat flux when using the analytic velocity

Table 4-4   The Comparison of Enhanced Heat Flux Using
Numerical Velocity with Heat Flux Using Analytical Velocity
(Model 3, Water-Glass, Pr = 7.03, α = 3)

A. Heat Flux Using Analytic Velocity				
Δx (cm)	ϕ (w/cm$^2 \cdot$K)	ϕ_f (w/cm$^2 \cdot$K)	ϕ_w (w/cm$^2 \cdot$K)	β (w/cm$^4 \cdot$K)
0.9839	0.0230	0.0149	0.0811	0.0238
2.9519	0.1855	0.0132	0.0724	0.0213
4.9194	0.3864	0.0098	0.0541	0.0159
6.8868	0.5810	0.0075	0.0415	0.0122
7.8847	0.6775	0.0067	0.0369	0.0109
9.8390	0.8638	0.0055	0.0302	0.0089
B. Heat Flux Using Computed Velocity				
1.0033	0.0234	0.0149	0.0811	0.0232
3.0101	0.1870	0.0133	0.0728	0.0206
5.0164	0.3899	0.0097	0.0533	0.0155
7.0226	0.5790	0.0076	0.0420	0.0117
8.0402	0.6746	0.0068	0.0374	0.0104
10.0328	0.8597	0.0055	0.0302	0.0085

* Model 3, Water-Glass
* ϕ......enhanced axial heat flux
* ϕ_f.....axial heat flux by conduction in fluid
* ϕ_w.....axial heat flux by conduction in pipe wall
* β = $\phi/\Delta x^2$

(Eq. 1-4) for $\alpha = 1$, Pr = 7.03, pipe radius $R_1 = 0.1$ cm and glass walls of thickness $\Delta R = R_2 - R_1 = 0.05$ cm (which is almost equal to the boundary layer thickness $\delta = 0.047$ cm for this case) with Model 3. There were 22 points distributed along the radius (13 points in fluid), and the smallest distance next to the wall is equal to 0.16δ, while along the axial direction 101 point were used (60 points in the central pipe section). Thirty period runs were considered in order to insure that the final periodic state was achieved. An exception was the $\Delta x = 1$ cm case where only 23 period runs were computed. Under the exact same conditions described above, a calculation using the numerical velocity with build-up process was tested. Part B of table 4-4 gives the axial heat flux results using the corresponding numerical generated velocity profile. A comparison of results shown in Table 4-4 is quite good. One sees that the disagreement for most terms is less than 0.001. Note for Δx of 10 cm, the ratio ϕ/ϕ_f is about 15 and gets larger as Δx is increased further.

Periodic Temperature Build-up in Thermal Pumping Process

The purpose of this facet of the present study was to examine the temperature field build-up pattern and to determine how long before the final periodic temperature state can be reached. The author also intends to verify whether or not there indeed exists a time averaged linear axial temperature distribution within the thermal pump at

larger time as assumed in existing analytic solutions [15, 16, 22].

Model 1 was employed to study the temperature build-up history for the case where the initial velocity was zero everywhere inside the pipe as well as at the boundary. The initial temperature condition was assumed to be identical with the cold end temperature at all grid points except those at $x = 0$ where the dimensionless temperature $T = T_h = 1.0$

Figs. 4-11, 4-12 and 4-13 show the computed temperature build-up history at Wormersley number $\alpha = 1$ at $x = L/4$, and $L/2$ (where $L = 20$ cm is the pipe length), and either on the axis $r = 0$ or at the wall $r = R_1$. The tidal displacements were chosen as $\Delta x = L/10$, $L/4$, and $L/2$, respectively. In these figures, the ordinate represents the dimensionless temperature, while the abscissa represents the oscillatory period runs. These temperature histories show a sinusoidal variation. Three characteristics can be summarized: 1) when the tidal displacement is large, the amplitude of the temperature variation is also large, and less adjusting time is needed; 2) the amplitude of the sinusoidal variation of the temperature along the axis is larger than that near the wall (see Figs. 4-4, 4-5); 3) after a short transient process, the final oscillatory state is reached. The time-averaged temperatures of this oscillatory state at a given x-position have the same value
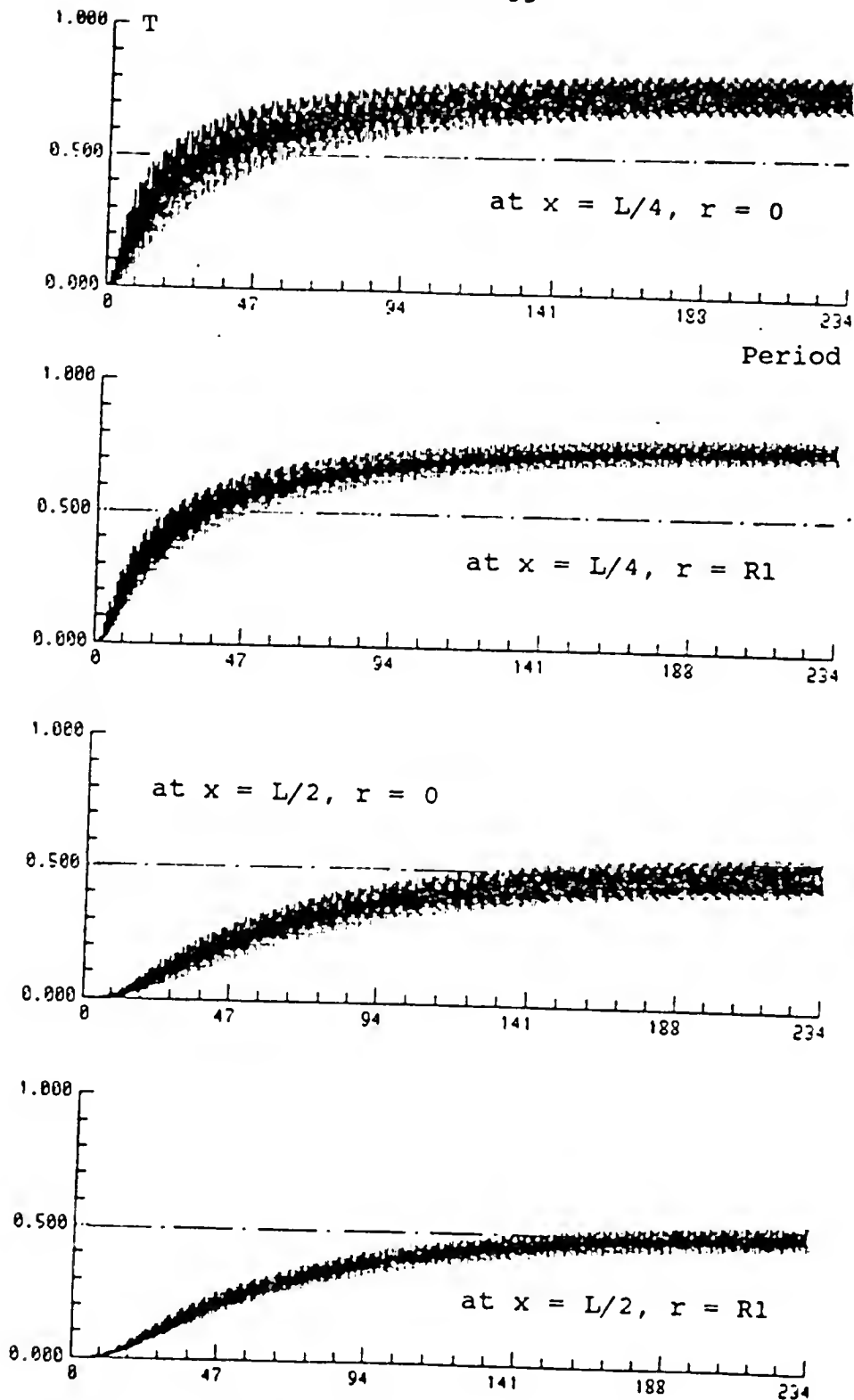
Fig 4-11   Temperature Build-up Process In Oscillating
Flow (Model 1, $\alpha = 1$, $\Delta X = 2$cm)
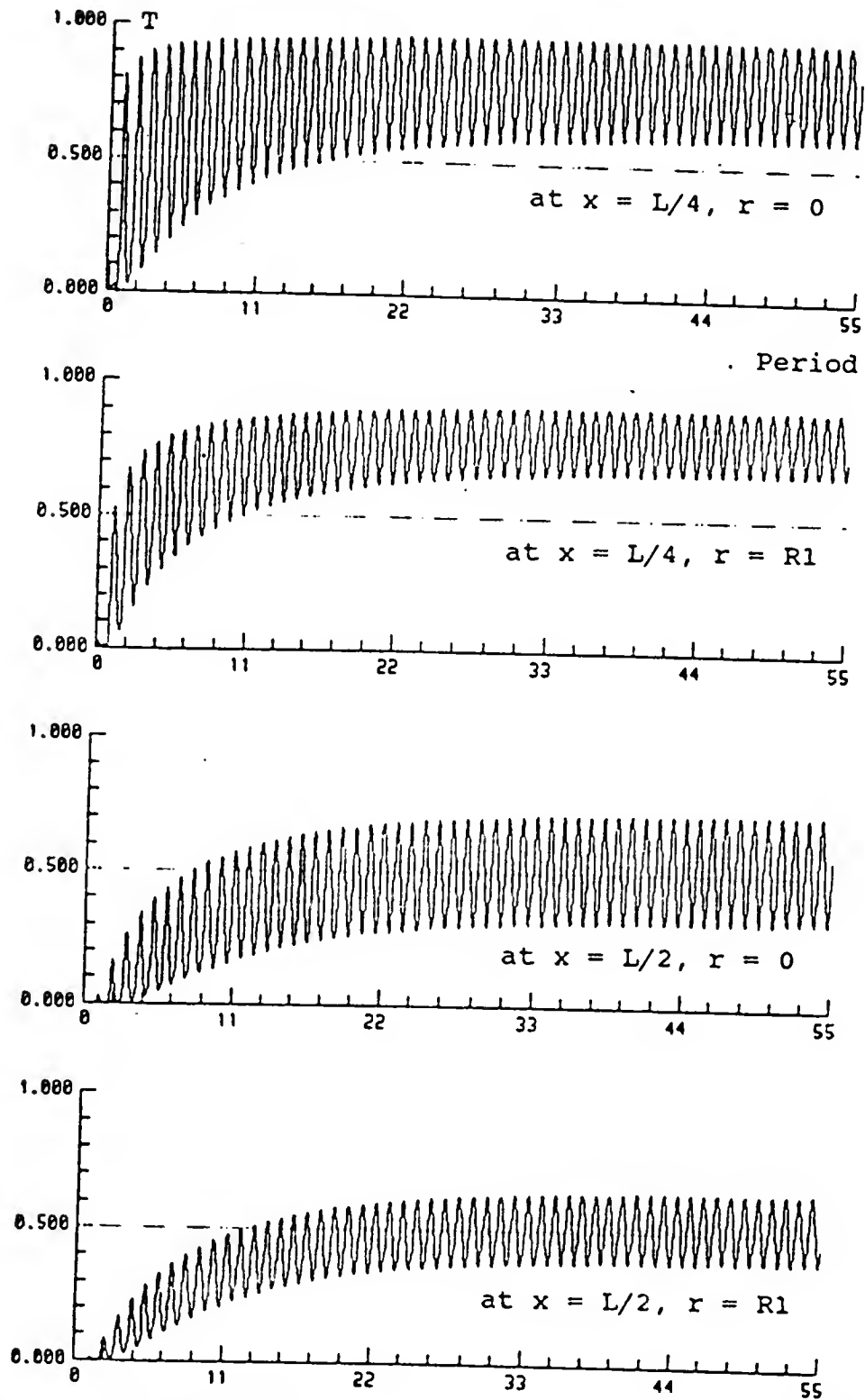
Fig 4-12   Temperature Build-up Process In Oscillating
Flow (Model 1, $\alpha = 1$, $\Delta x = 5cm$)
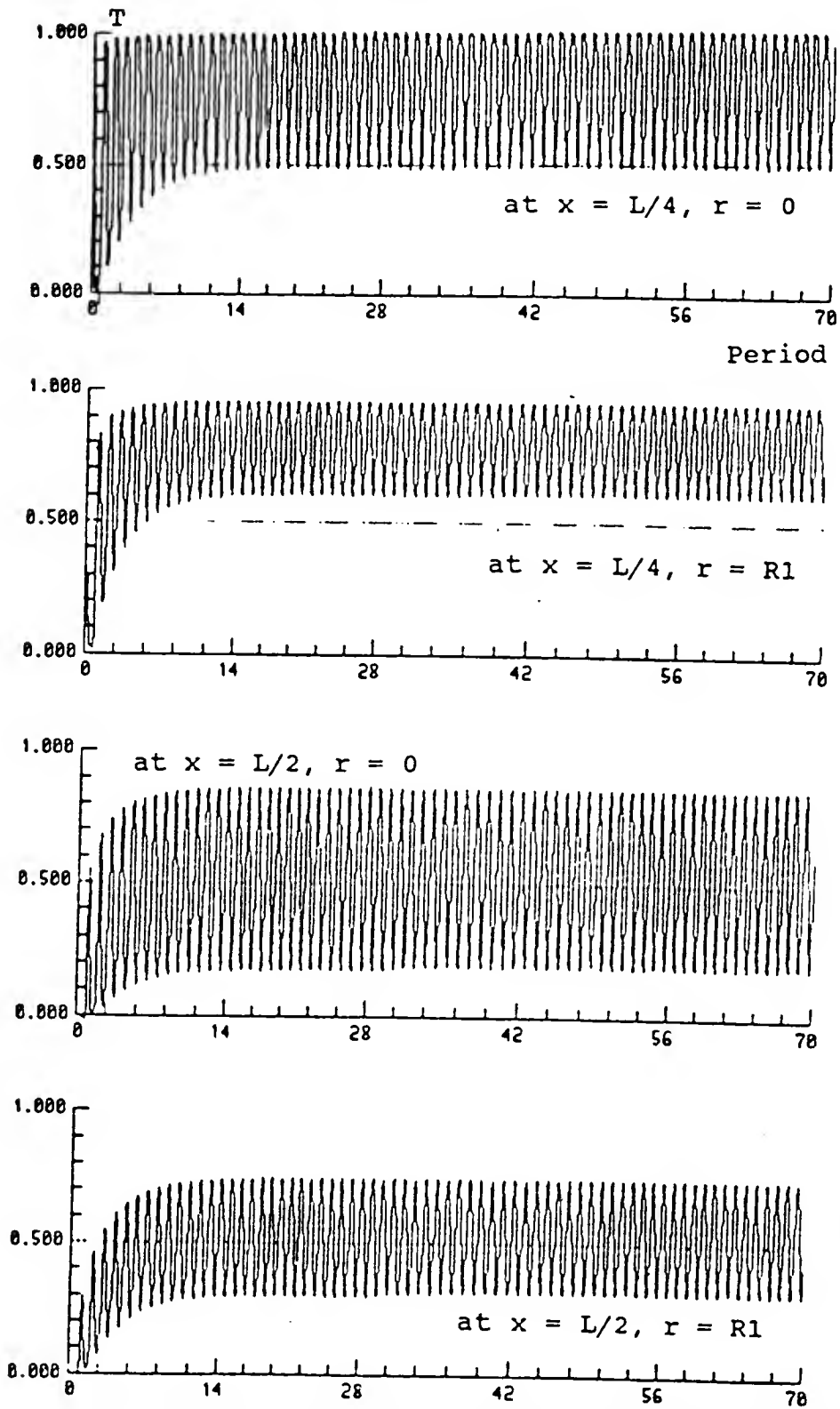
Fig 4-13   Temperature Build-up Process In Oscillating
              Flow (Model 1, $\alpha = 1$, $\Delta x = 10$cm)

for all tidal displacements. It implies that the final time-averaged temperature depends on its x-position only. For example, the final periodic dimensionless time-averaged temperature is about 0.5 at the location x = L/2, while it is about 0.75 at x = L/4 since this latter position is much closer to the hot end. From this observation, one may well imagine that the periodic temperature state along the longitudinal direction is close to the linear function form assumed in existing analytic studies [17, 22]. This feature will be further demonstrated later.

Figs. 4-11, 4-12, 4-13 also show the time needed for a build-up to the final periodic state of the thermal field. An unpublished conservative analytical estimation of the build-up time by Kurzweg, based on the assumption that the oscillating flow satisfies the tuning condition is

$$t_1 = L^2/[\omega \Delta x^2 \ \lambda(\alpha, Pr)] \qquad (4-1)$$

where $\lambda(\alpha, Pr) = k_{eh}/\omega \Delta x^2$ is a function of thermal conductivity and Wormersley number [15, 16]. At the tuning point, this value of λ is about 0.02. If the tidal displacement Δx = L/2 = 10 cm and the angular frequency ω = 1 (for water with R_1 = 0.1 cm), the adjustment time t_1 can be estimated from equation (4-1) to be equal to 200 sec., or 32 periods. The computed results show that the actual adjusting time is only 20 periods.
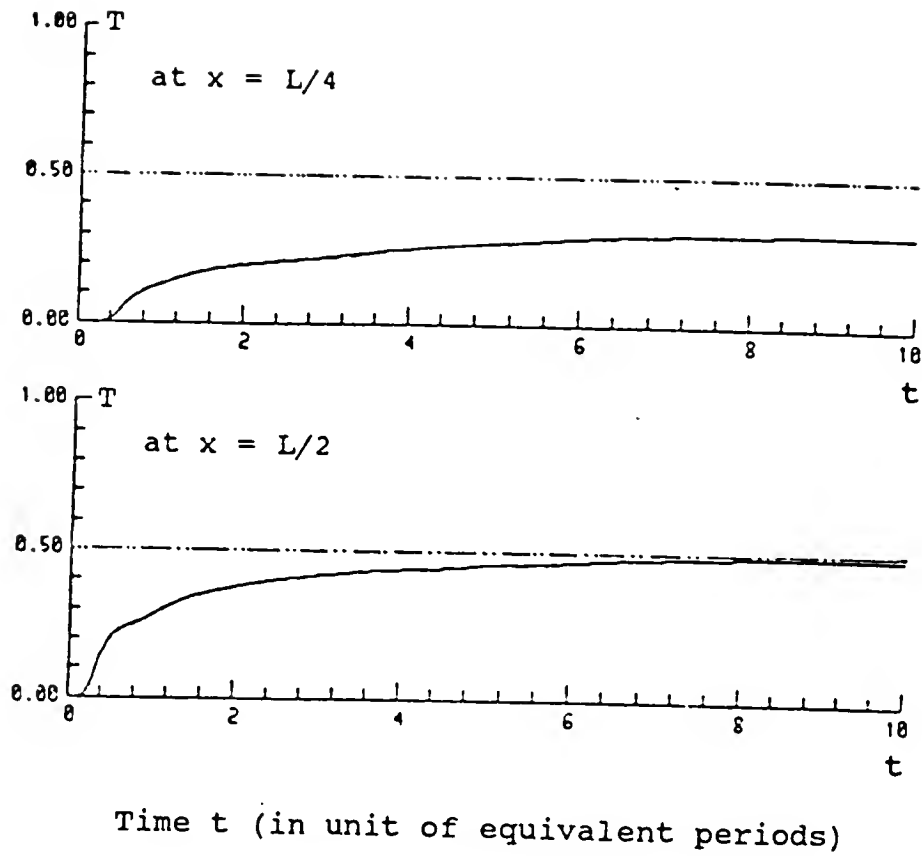
Fig 4-14   Temperature Build-Up Process In Steady Flow
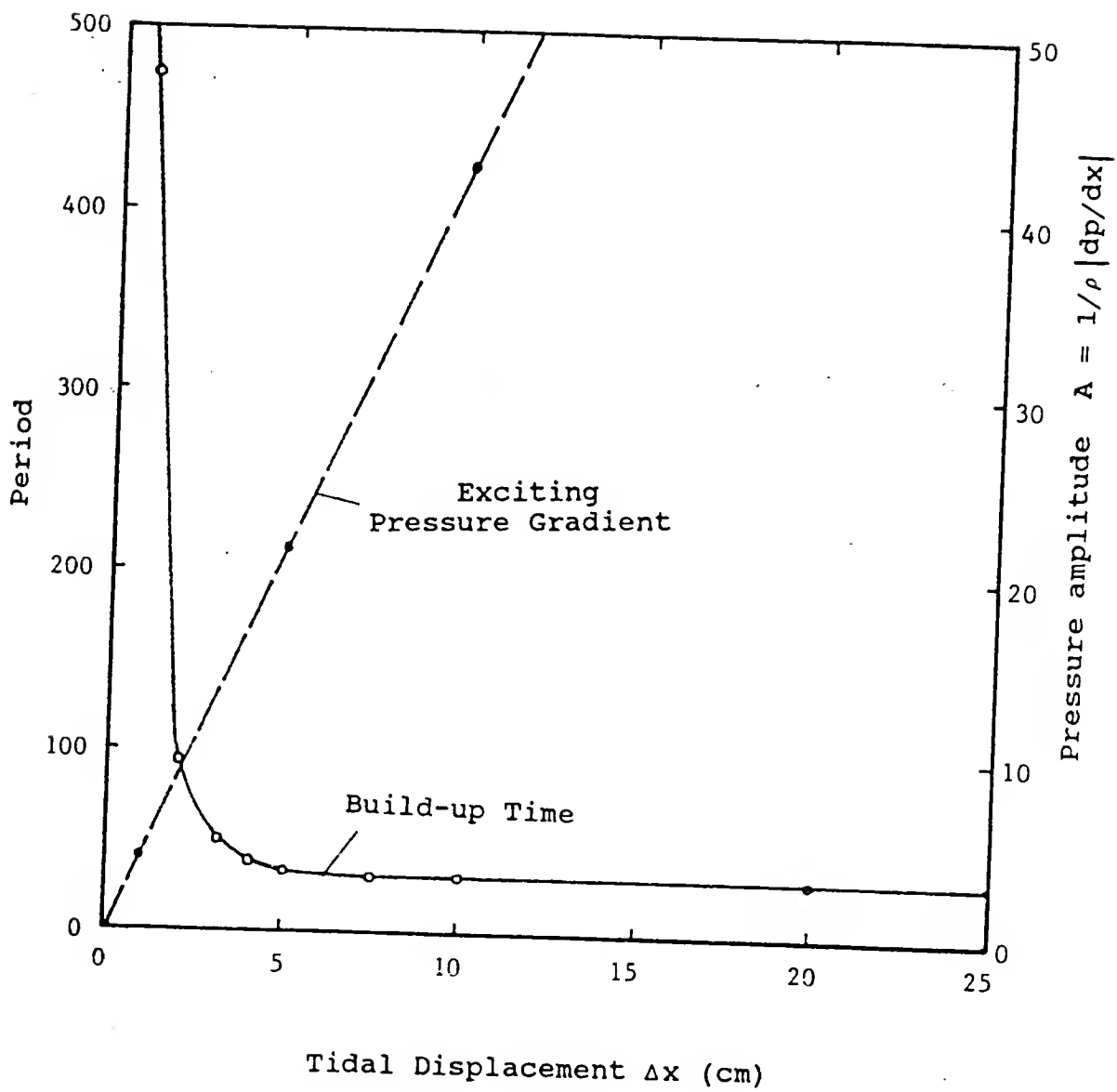(Model 2, U_{eq} = 1.5 cm/sec)

Fig 4-15   Build-Up Time Versus Tidal Displacement
(Model 2, $\alpha = 1$)

Fig. 4-15 shows the build-up time versus the tidal displacement and applied pressure gradient corresponding to various tidal displacements with Model 2. It can be seen that when the tidal displacement is very small, the build-up time tends towards infinity, so that the so-called final periodic state no longer exists. The final periodic temperature state will thus be established only by heat conduction and has a complementary error function $erfc(x,t)$ = 1 - $erf(x,t)$ temperature build-up history [1, 11]. As the tidal displacement gets larger, the build-up time needed decreases, and when Δx is greater than about L/4 (5 cm) the build-up time is almost constant.

In order to compare with the steady Hagen-Poiseuille flow, a transient temperature history of such a flow with Model 2 is also shown in Fig. 4-14. Both curves represent the temperature computed along the axis (r = 0). The upper temperature curve is at x = L/4, while the lower one is at x = L/2. It is clearly seen that here there is no oscillatory pattern at all. The final temperature state is here related to the classical Graetz problem dealt with in great detail in the heat transfer literature [5, 11].

Temperature Distribution in Model 1

The final periodic temperature distributions for the three different models with either conducting walls or insulating walls have been obtained. Fig. 4-16, 4-17 and 4-18 show the computed periodic final temperature distribution
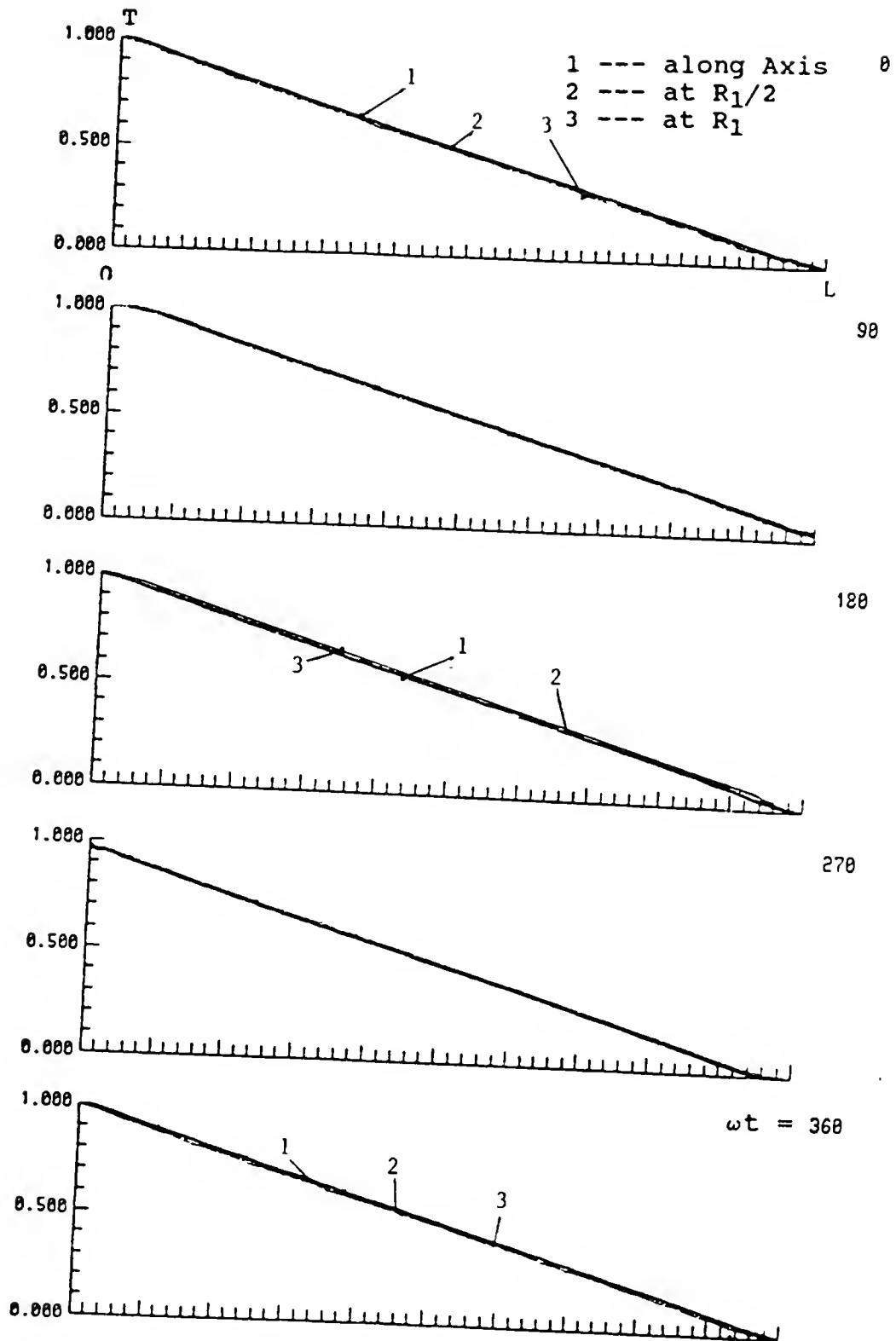
Fig 4-16   Temperature Distribution in Oscillating Pipe
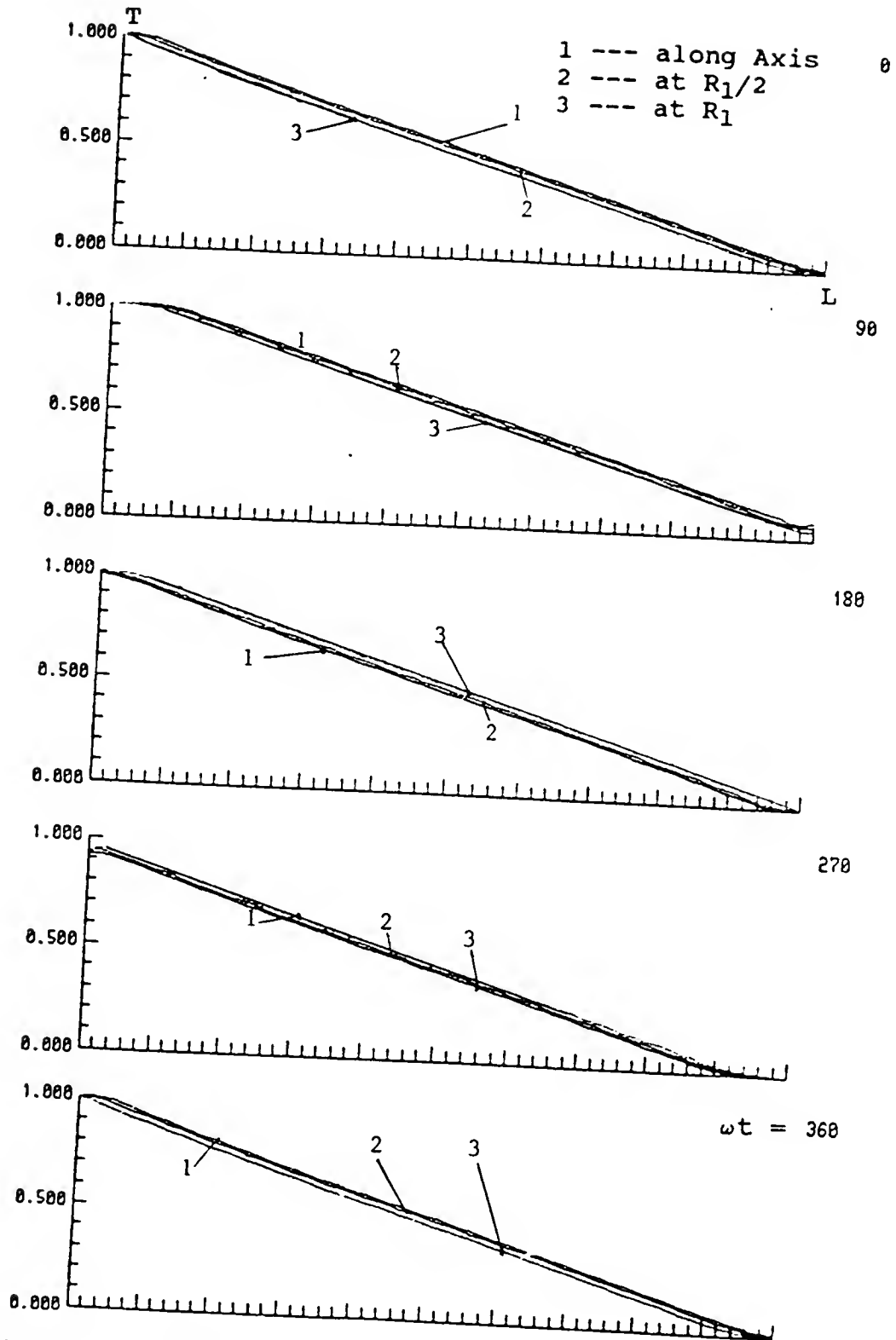Flow (Model 1, $\alpha = 1$, $\Delta x = 1$cm)

Fig 4-17   Temperature Distribution in Oscillating Pipe
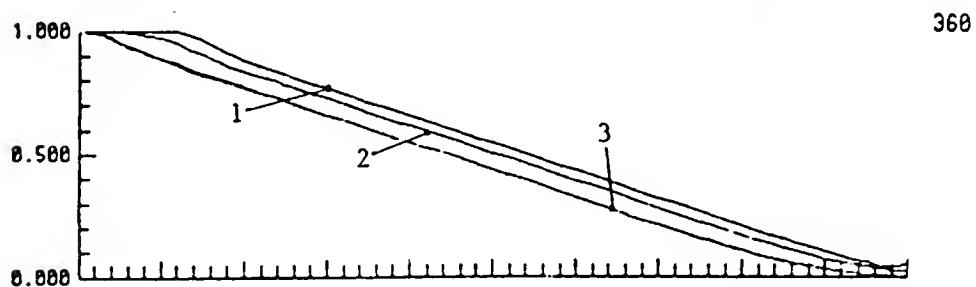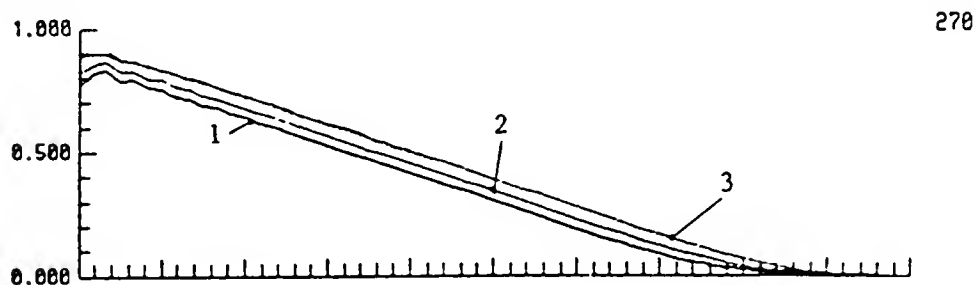Flow (Model 1, $\alpha = 1$, $\Delta x = 2cm$)
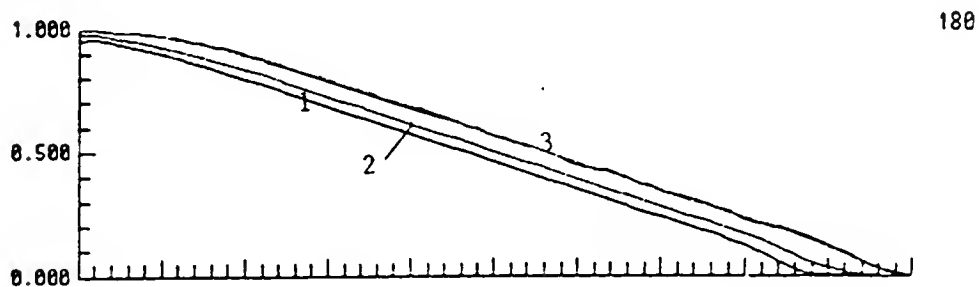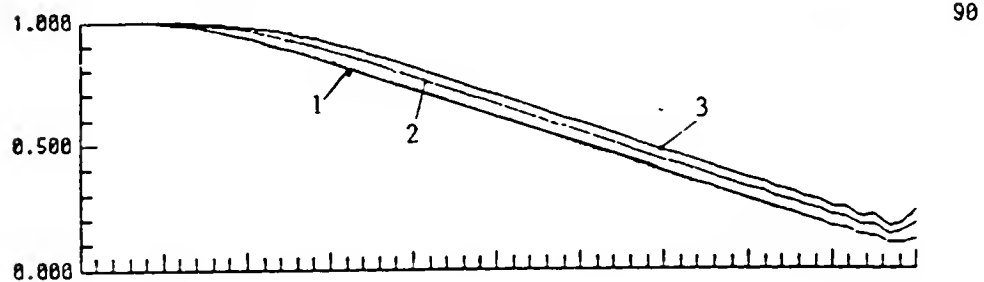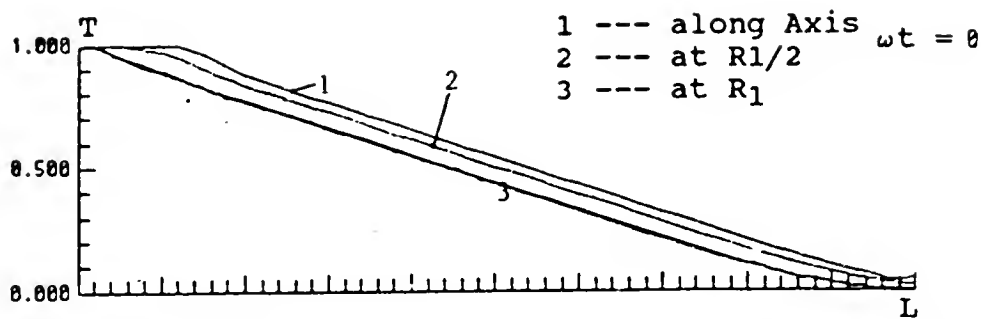
Fig 4-18   Temperature Distribution in Oscillating Pipe
Flow (Model 1, $\alpha = 1$, $\Delta x = 5$cm)

$T(r,x,\infty)$ in oscillating pipe flow with Model 1. The marked numbers 1, 2, 3 represent the temperature along the axis (r = 0), $r = R_1/2$, and at $r = R_1$ (wall), respectively. For these computations, the Wormersley number was taken as $\alpha = 1$ and the tidal displacement was chosen as Δx = 1 cm, 2 cm and 5 cm, respectively. Neglecting the somewhat erratic behavior near the pipe ends, the time-dependent temperature shows a clear linear distribution pattern along longitudinal direction especially for the relatively small tidal displacement case, of say, Δx = 1 cm. If one focuses on one cross-section (x = constant), one can clearly see the temperature near the boundary and that at the axis are alternately higher and lower relative to each other (Fig. 4-18) within a period. This implies that a very large radial conduction heat exchange occurs between the core of the flow and the boundary layer. Note that the radial temperature gradient becomes very large during parts of an oscillating cycle.

The poor behavior of the temperature distribution noted near both ends of the pipe in Fig. 4-18 at tidal displacement of Δx = 5 cm is caused by numerical dispersion which is a common shortcoming of the second order numerical method employed [24, 28, 30, 37]. It may be improved by either using an odd order numerical method such as the first-order upwind method, flux splitting technique [24] or by employing alternative models which are able to avoid any

discontinuity of the physical properties at both ends, such as Model 3.

Temperature Distribution in Model 2

In order to explore some alternative possible devices which apply the enhanced thermal pumping technique, Model 2 (Fig. 2-3) was developed and numerically examined. The temperature distributions in Model 2 have been studied and results are recorded in Figs. 4-19, 4-20, 4-21, 4-22 and 4-23 for some special cases. The working fluid used is again water and similarly, the Wormersley number was taken as $\alpha = 1$. The tidal displacements used were $\Delta x = 1$ cm, 5 cm, 10 cm, 20 cm, and 30 cm, respectively. The marked numbers 1, 2, 3 in those figures represent the temperatures at $r = R_1$ (wall), $R_1/2$ and $r=0$ (i.e., along the axis). It can be seen that the temperatures in the core of the flow and that in the boundary layer in these figures vary periodically in the radial direction during the oscillations. The results also show a linear axial temperature variation between the heating and cooling sources when the tidal displacement is small ($\Delta x = 1$ cm, Fig. 4-19). As the tidal displacement becomes larger ($\Delta x = 5$ cm, Fig. 4-20), the linear axial temperature variation becomes weaker. The difference of temperature in the core of the flow and that in the boundary layer is evident and shows a radially alternating pattern within an oscillation period just as seen in Model 1. However, as the tidal displacements are further increased,

Fig 4-19   Temperature Distribution in Oscillating Pipe
Flow (Model 2, $\alpha = 1$, $\Delta x = 1cm$)

Fig 4-20   Temperature Distribution in Oscillating Pipe
            Flow (Model 2, α = 1, Δx = 5cm)

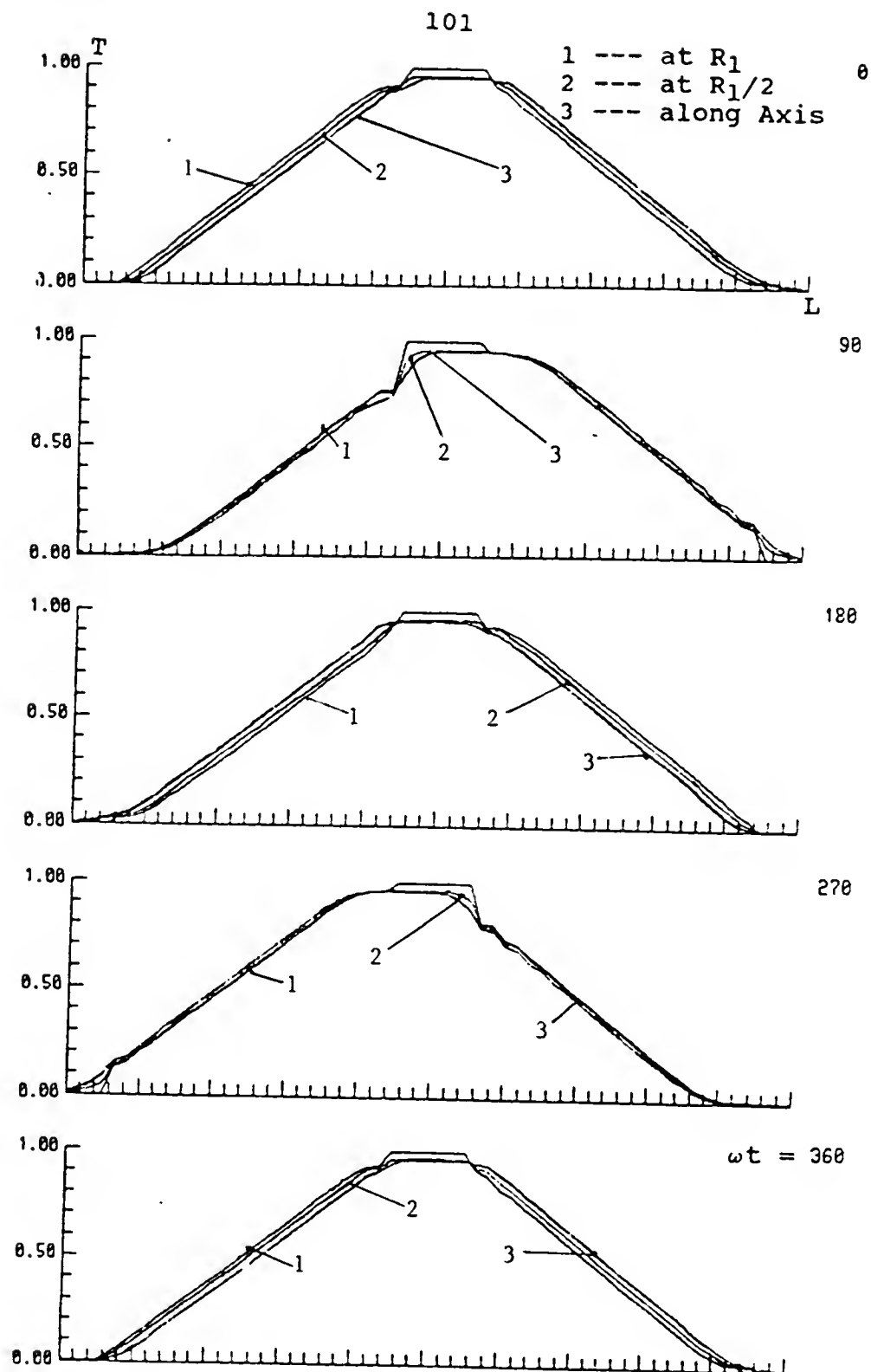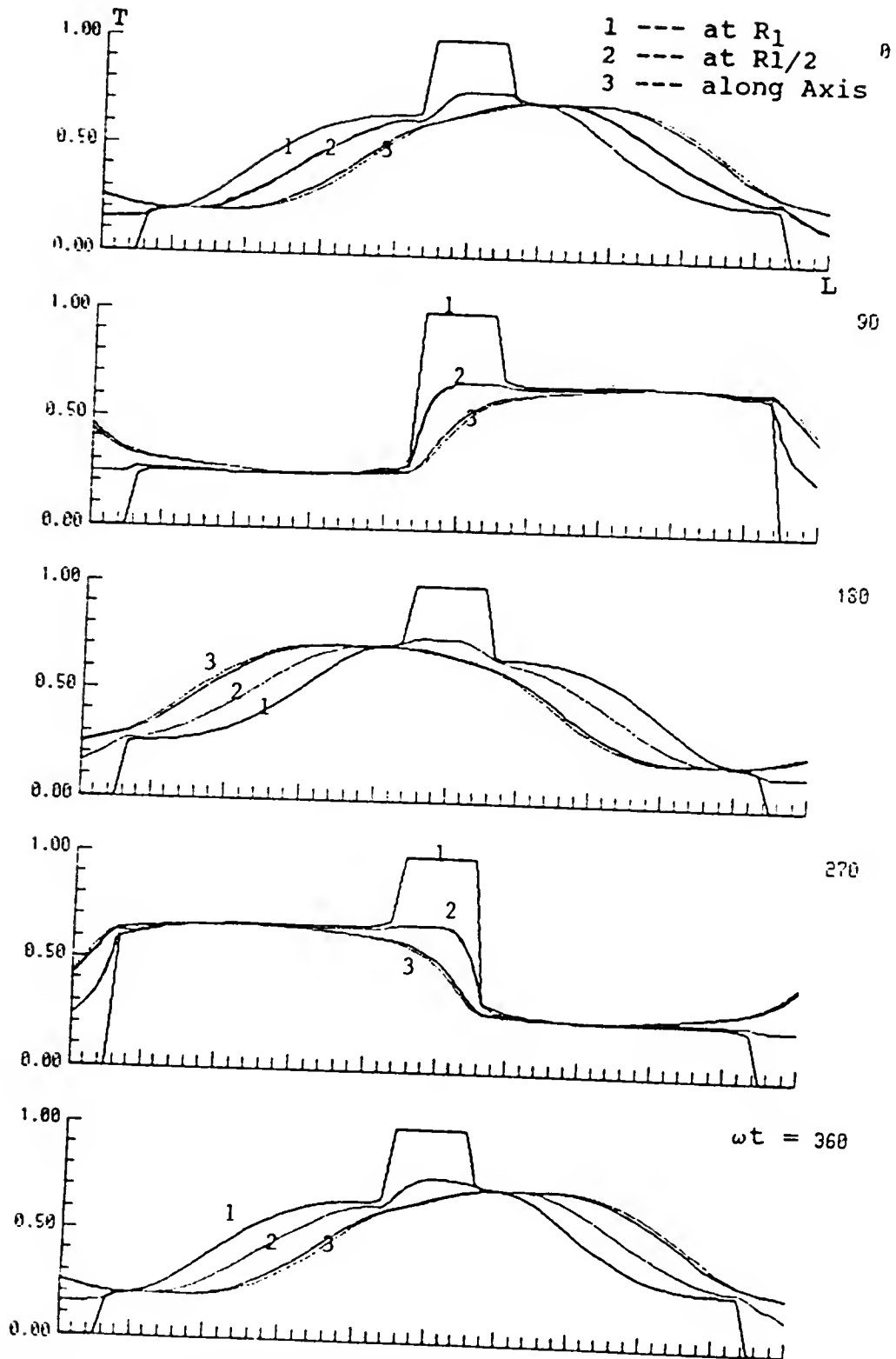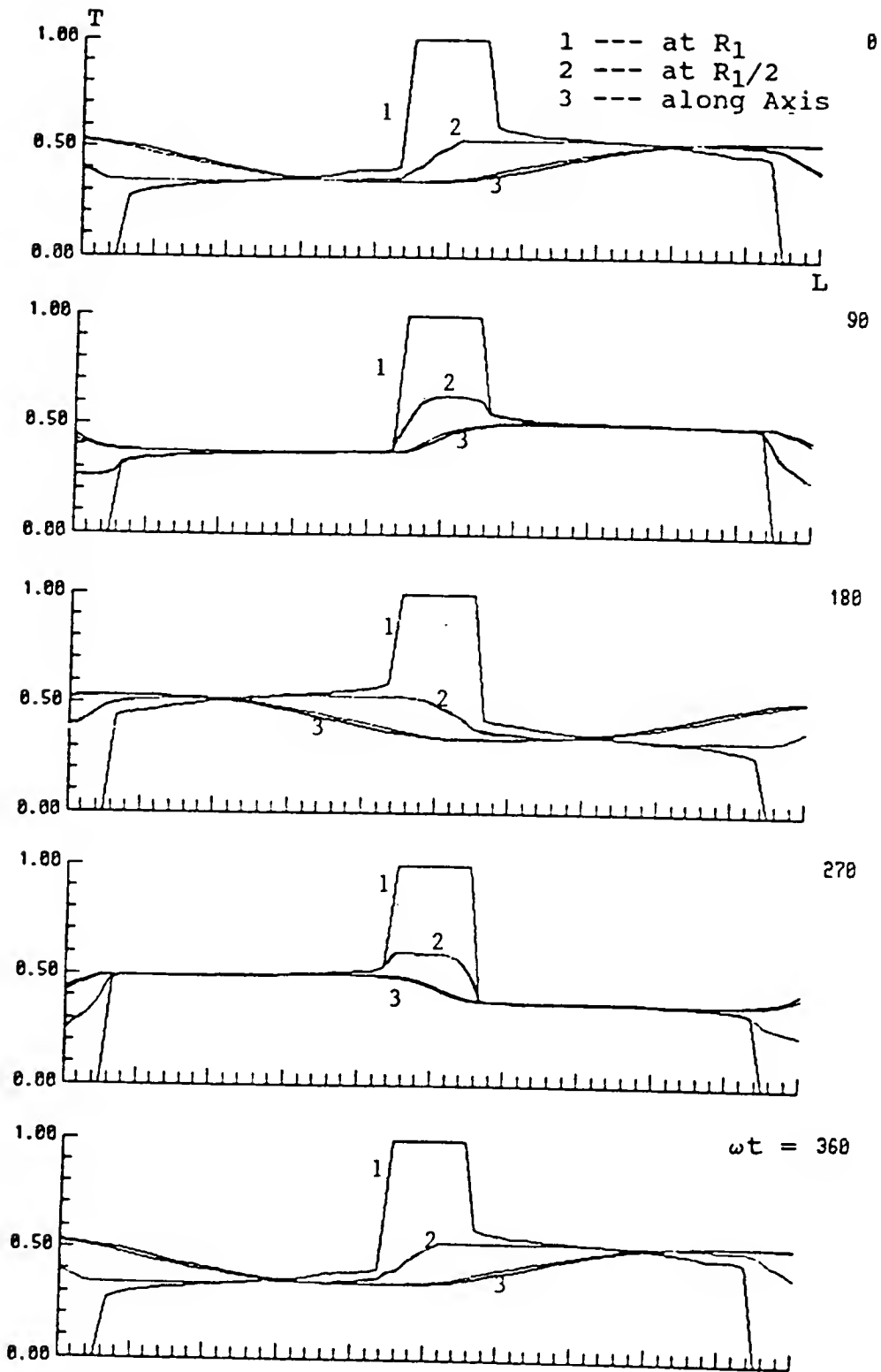Fig 4-21   Temperature Distribution in Oscillating Pipe
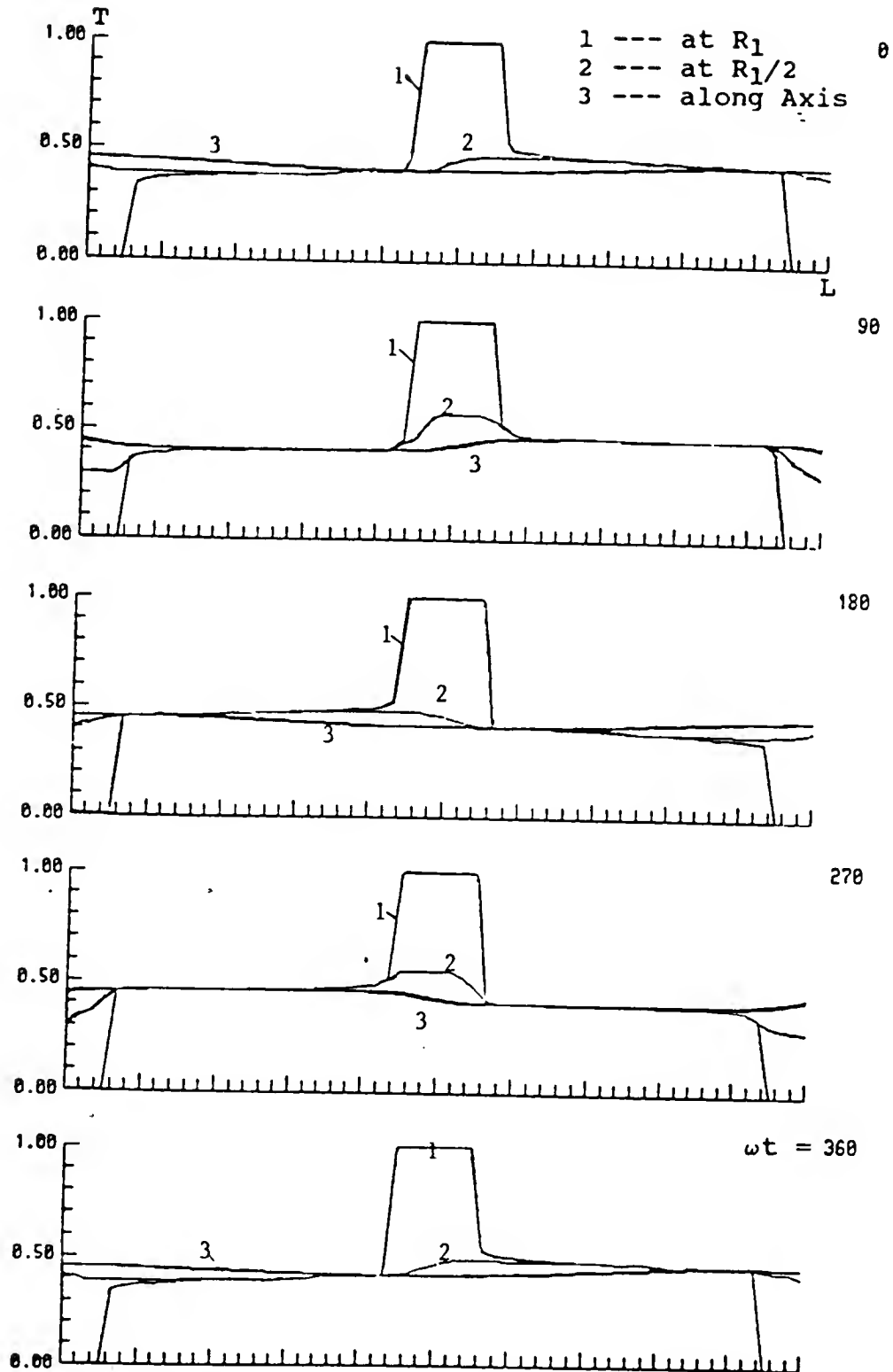Flow (Model 2, $\alpha = 1$, $\Delta x = 10$cm)

Fig 4-22   Temperature Distribution in Oscillating Pipe
            Flow (Model 2, α = 1, Δx = 20cm)
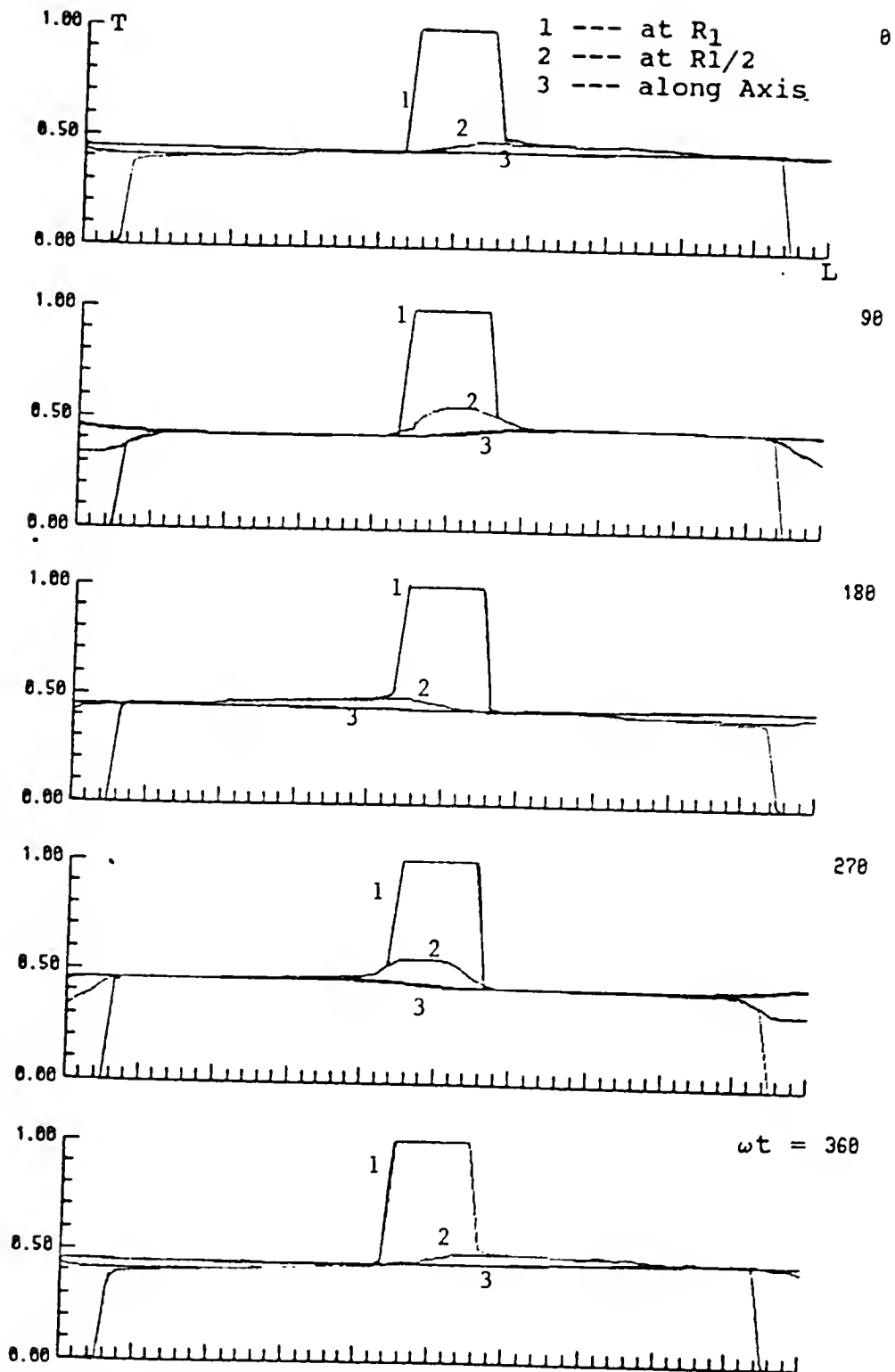
Fig 4-23   Temperature Distribution in Oscillating Pipe
Flow (Model 1, α = 1, Δx = 30cm)
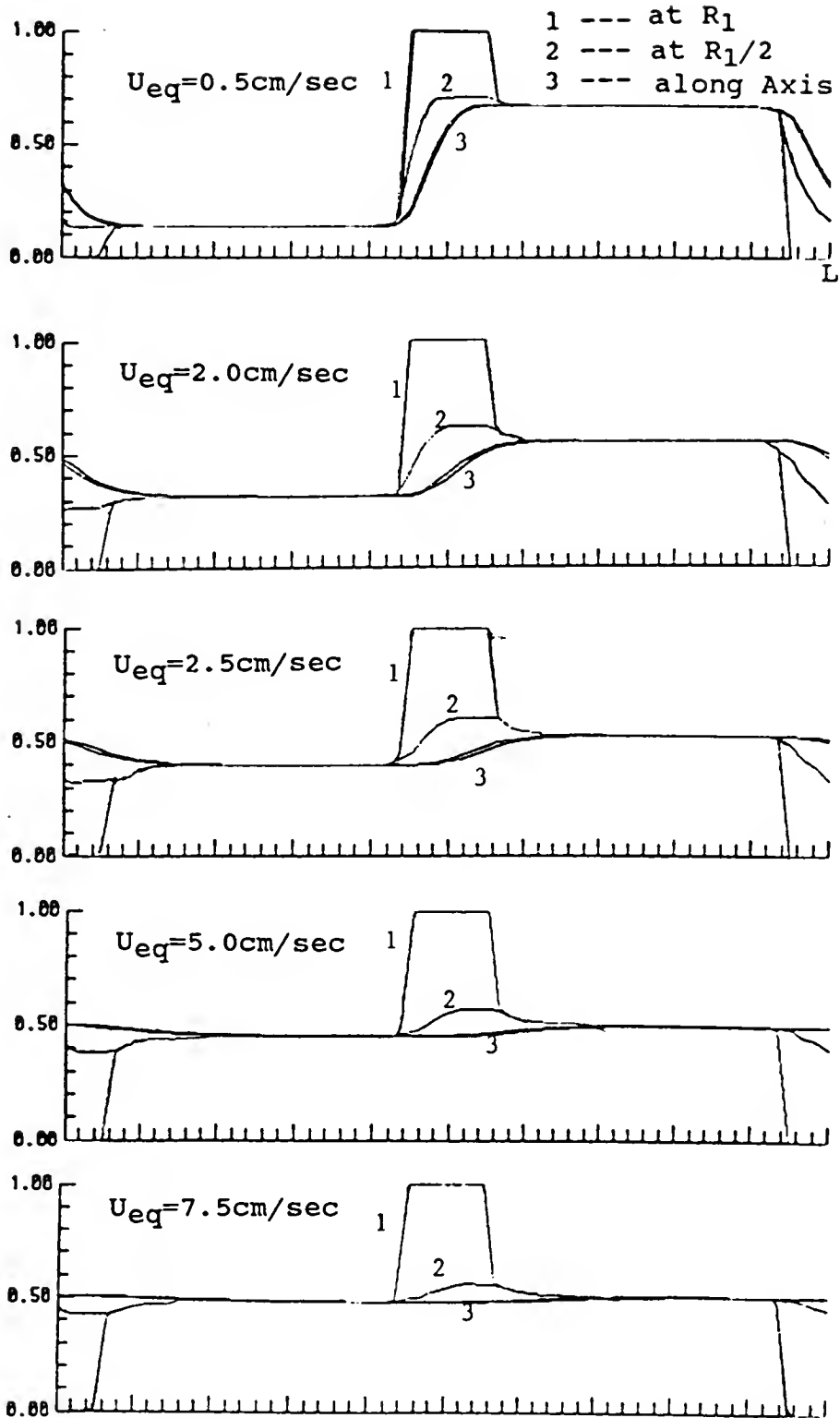
Fig 4-24   Temperature Distribution in Steady Flow
(Model 2, U_{ave} = 0.5-7.5 cm/sec)

as shown in Fig. 4-21, the radial temperature gradient almost no longer exists except directly in the vicinity of the heat source and sink area. It is obvious that the cross-section averaged temperature in the pipe tends to become constant and equal to the mean value of the hot and cold source region. This phenomenon can be seen even more clearly as the tidal displacement is further increased (Figs. 4-22, and 4-23). One can conclude from such a temperature distribution that the increase of axial heat transfer ability with increasing tidal displacement is most likely to be limited. At the same time, this axial heat transfer capability is expected to increase by increasing either the individual source size or the density of the alternatively distributed hot and cold sources.

This unexpected temperature distribution in Model 2 at large tidal displacements led us to further examine the thermal field of steady pipe flow for the boundary conditions used in Model 2. The computed temperature distribution with an equivalent steady averaged velocity from 0.5 cm/sec to 7.5 cm/sec, corresponding to tidal displacement from 1 cm to 15 cm at an oscillating frequency of ω = 1/sec are shown in Fig. 4-24. The equivalent velocity is established from the relation $U_{eq} = \Delta x \omega / 2$. As could have been anticipated, large radial temperature gradients in this flow (similar that in the oscillating flow with large tidal displacement), occur only at the heat

source and sink areas, while the radial temperature gradient in the rest of the pipe is very small. The constant temperature difference at the right-hand-side differs from that on the left hand side of the heat source. This temperature difference becomes progressively smaller as the equivalent velocity is increased (i.e., the fluid heating becomes less).

Temperature Distribution in Model 3

Model 3 was developed to examine the performance of the thermal pump without convective heat exchange at the ends (in the chambers). That is, the heat is added and withdrawn by conduction through the pipe end section (see Fig. 2-4). The computed temperature distribution in this model is shown in Fig. 4-25, and a magnified view of the temperature in the central section is shown in Fig. 4-26. The Wormersley number used is again $\alpha = 1$ and the tidal displacement $\Delta x = 10$ cm. Two features are observed. First, in contrast to the temperature computed in Model 1, the temperature obtained here shows a very smooth pattern at the central section ends (i.e., at $x = 5L$ and $6L$ in Fig. 2-4). Second, the linear axial temperature distribution with time-dependent radial temperature gradient alternating in sign in the central portion of the pipe (namely, $5L < x < 6L$, in Fig. 2-4) is retained even when the tidal displacement is as large as $\Delta x = 10$ cm (Fig. 4-26).
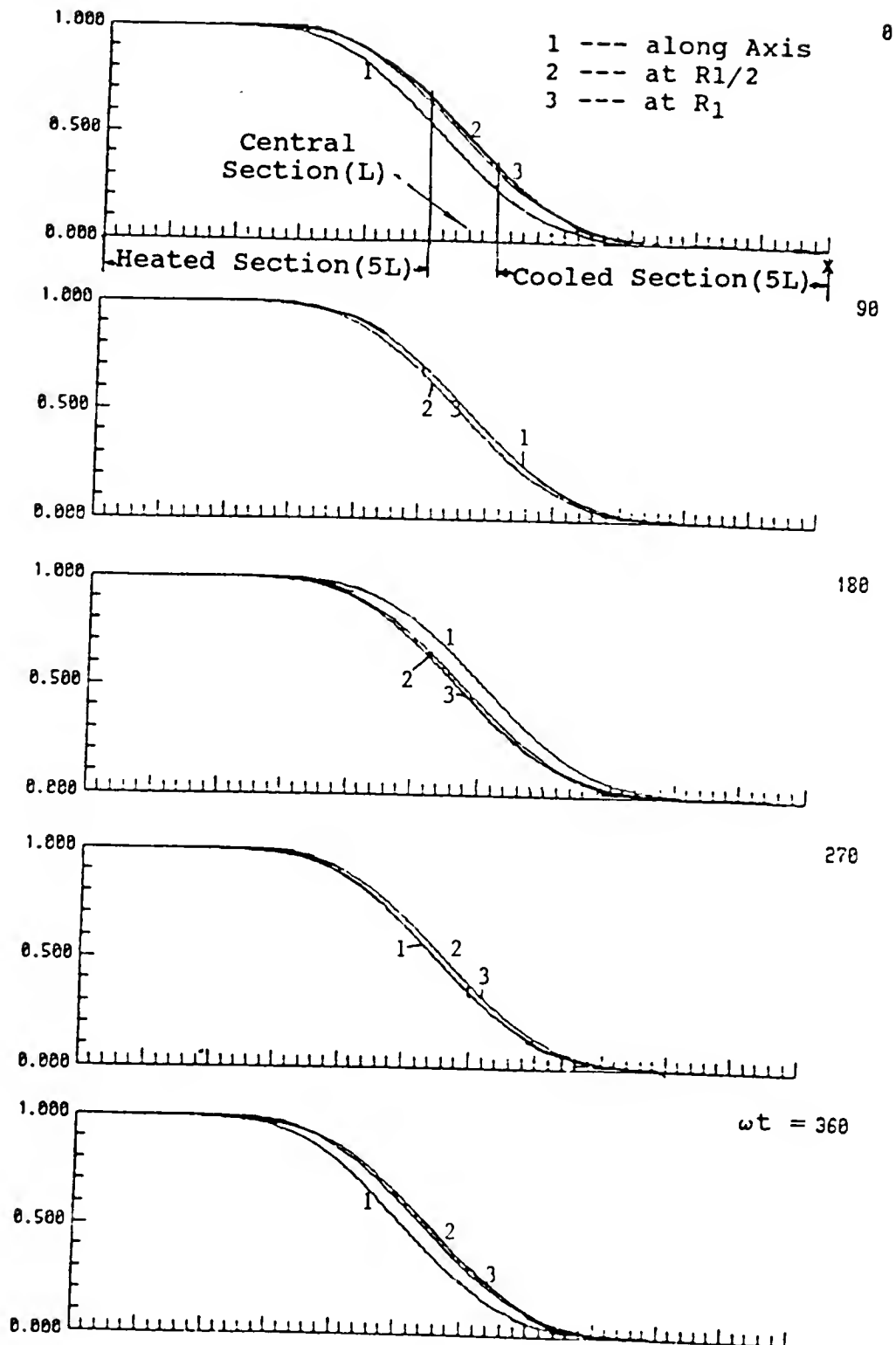
Fig 4-25   Temperature Distribution in Oscillating Pipe
Flow (Model 3, $\alpha = 1$, $\Delta x = 10$cm, $L=20$cm)
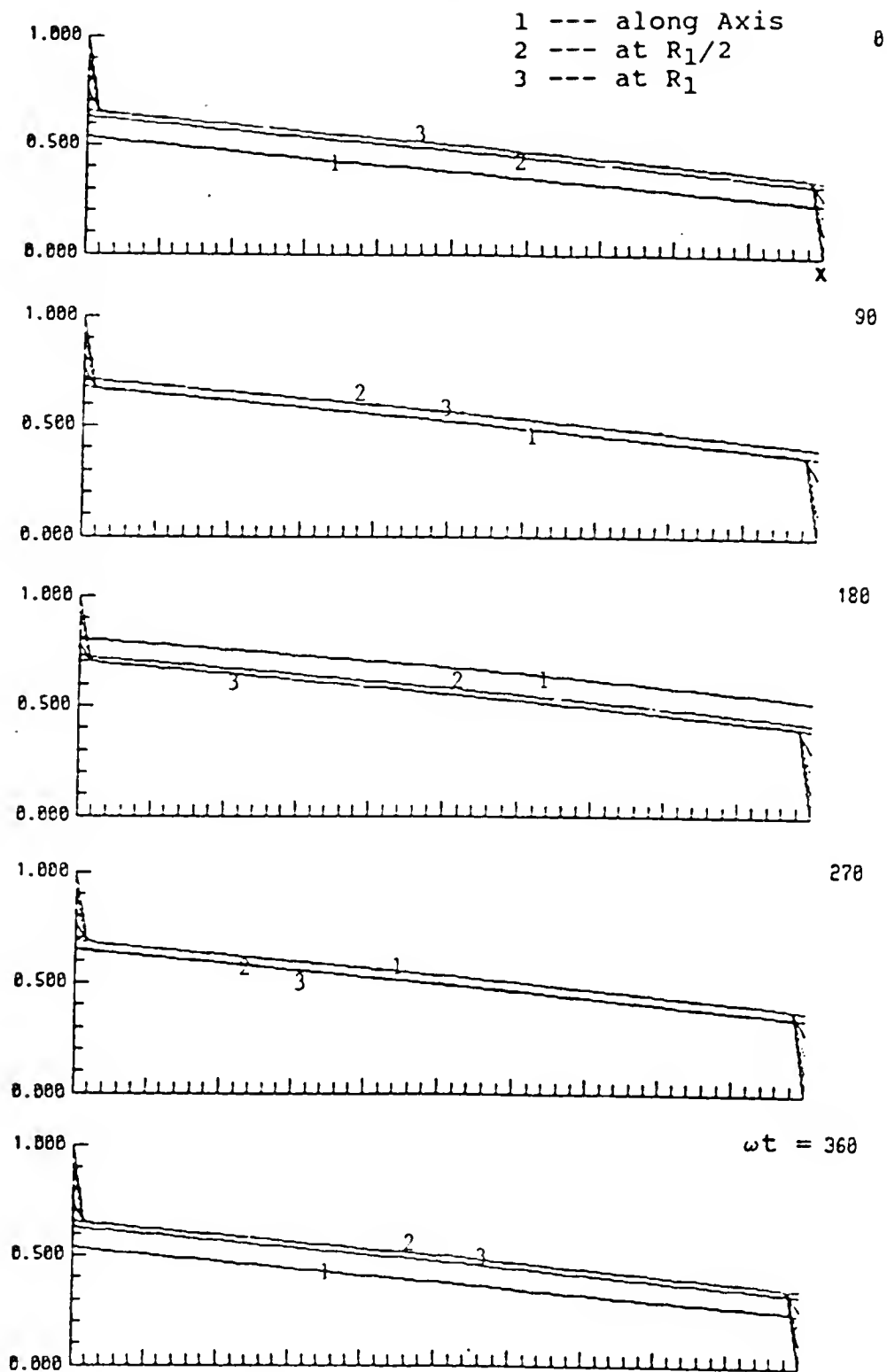
Fig 4-26   Magnified View Of Temperature
in the Central Pipe Section
(Model 3, α = 1, Δx = 10cm)

Heat Flux Versus Tidal Displacement (Model 2)

As mentioned in the previous section, a limit on the axial heat transfer in oscillating flow with Model 2 exists, and the heat axially transferred in the steady Hagen-Poiseuille flow with the same model could be expected as the upper limit of the corresponding oscillating flow.

This has been verified by a numerical calculation with water as the working medium and the results are recorded in Table 4-5, and 4-6, and also plotted in Fig. 4-27. The Wormersley number used in the current test is $\alpha = 1$, and the tidal displacement for the oscillating flow varied from 1 cm to 30 cm. The corresponding equivalent average velocity varied from 0.5 cm/sec to 15 cm/sec for the steady flow case. In Fig. 4-27 the ordinate represents the heat flux released from the hot source, the abscissa is the tidal displacement or the corresponding equivalent velocity for steady flow. The solid curve shows the heat flux computed for the oscillating flow, while the dashed curve shows the axial heat flux in steady flow. It can be seen that the slope of the heat flux curve in the oscillating pipe flow case is smaller than that in steady pipe flow in general and particularly when the tidal displacement is small (i.e., $\Delta x \leq 3$ cm). The flux increases rapidly as the tidal displacement gets larger ($\Delta x = 4$-6 cm). Still further increasing the tidal displacement does not lead to a further large increase of the axial heat flux. In fact the slope
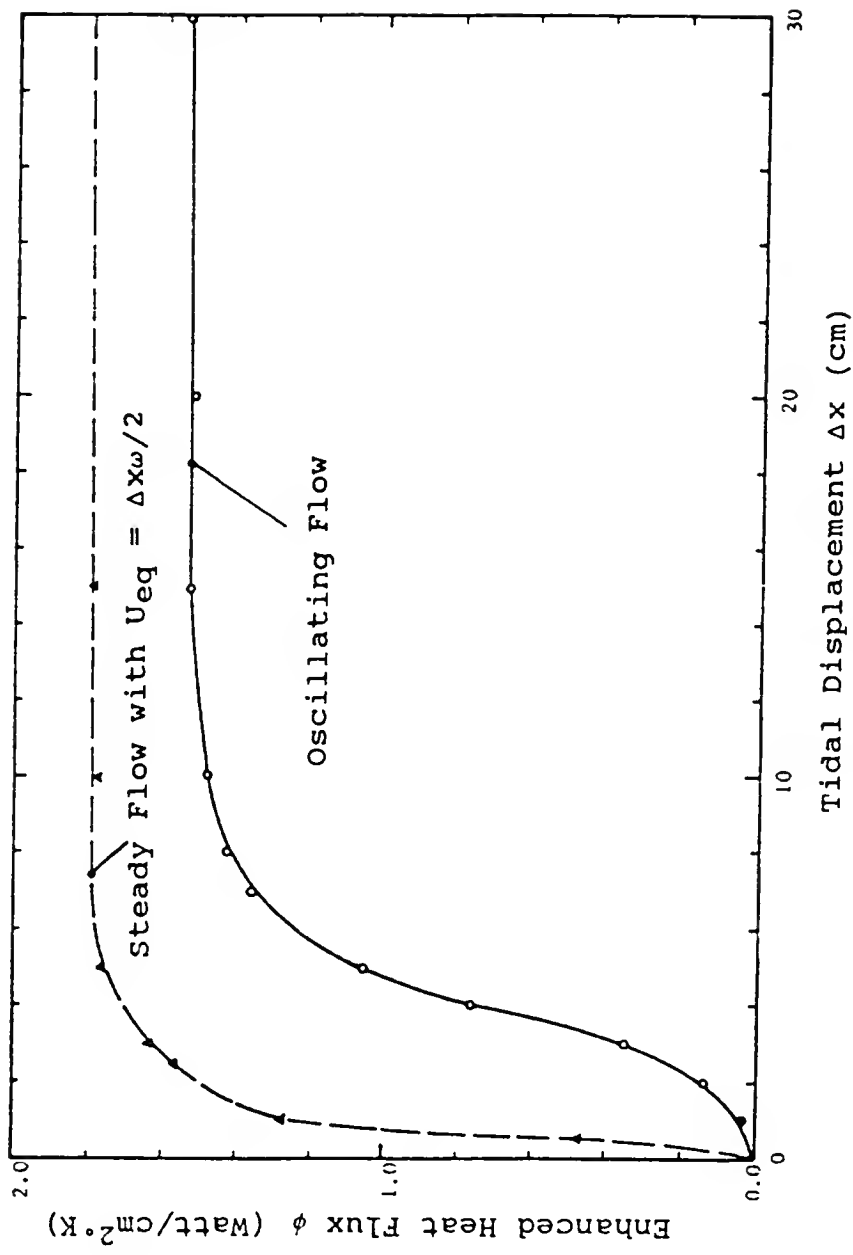
Fig 4-27 Heat Flux in Oscillating Flow and Steady Flow
(Model 2, $\alpha = 1$, Water — Working Fluid, Insulated Wall)

begins to decrease after the tidal displacement becomes larger than about $\Delta x = 8$ cm. Eventually this slope tends to zero as Δx increases still further. For the steady flow,

Table 4-5 Enhanced Heat Flux via Tidal Displacement
(Model 2, oscillating flow Pr = 7.03, α = 3)

Δx (cm)	Periods to final oscillation state *	Max. Pressure gradient $A=1/\rho\,\lvert\partial p/\partial x\rvert$ (cm/s^2)	heat flux ϕ (w/cm$^2\cdot$K)
1.000	75	4.86	0.03
1.962	15	8.372	0.136
2.943	7	12.588	0.345
3.924	6	16.744	0.683
4.905	5	20.930	1.051
6.867	5	29.300	1.377
7.848	5	33.488	1.420
9.843	5	42.000	1.484
15.233	5	65.000	1.545
19.920	5	85.000	1.522
30.100	5	126.000	1.530

* build-up time can be estimated by equation (4-1)

Table 4-6   Enhanced Heat Flux in Steady Flow

Δx (cm)	Max. Pressure gradient $A=1/\rho\,\lvert\partial p/\partial x\rvert$ (cm/s^2)	Ueq=0.5$\omega\Delta x$ (cm/s)	heat flux ϕ (w/cm^2°K)
0.500	2.43	0.25	0.462
1.000	4.86	0.50	1.354
2.500	10.50	1.25	1.567
3.000	12.56	1.50	1.631
5.000	21.00	2.50	1.775
8.000	33.50	4.00	1.664
10.000	42.00	5.00	1.786
15.000	65.00	7.50	1.779

the slope of the heat flux curve is quite large and almost constant at all equivalent velocities less than 0.5 cm/sec, but it rapidly decreases when the equivalent velocity becomes larger. Similar to the oscillating flow case, the heat flux ϕ as the velocity increases reaches a limit. This limit is about 20 percent greater than that for the oscillatory flow.

The reason of the slope variation in the oscillating flow can be explained as follows: At small tidal

displacement, K_e is quite small, and the molecular conduction is dominant, so that only a very small quantity of heat will be transferred axially. However, as the tidal displacement increases, $K_e = \lambda\omega\Delta x^2$ becomes considerably larger and the enhanced heat transfer mechanism now dominates axial conduction. The limit on axial heat flux observed at large Δx is due to a bottleneck which develops at the heat supply and removal sections due to insufficient conduction heat transfer.

In the steady flow, the fluid particles are always fresh ones with no residual heat in them so the radial temperature gradient is relatively larger than that in the oscillating pipe flow case. The larger radial temperature gradient increases the heat supply and removal capability so as to ensure an axial flux limit in excess of that possible for oscillating pipe flow in this model.

Influence of The Thermodynamic Properties (Model 2)

It is well known that the thermodynamic properties of the working fluid, especially the viscosity, are functions of the local temperature. Some thermodynamic properties of water for the temperature range of 0°C to 200°C are listed in Table 4-7. One can see that even over such a small temperature range the thermodynamic properties of water vary considerably. For instance, at T = 0°C, the kinematic viscosity $\nu = 1.788 \ 10^{-6}$ M^2/Sec, and the corresponding Prandtl Number is Pr = 13.6, while at temperature T = 100°,

Table 4-7   The Influence of Properties of
Water on the Enhanced Axial Heat Flux

T $^\circ$C	Pr	ρ g/cm^3	c_p ws/g$^\circ$K	ν 10^{-2} cm^2/sec	K w/cm$^\circ$K	Δx cm	ϕ at $\alpha=1$ w/cm^2°K
200	0.937	0.8668	4.505	0.160	0.665	10.031	1.025
160	1.099	0.9097	4.417	0.173	0.680	11.499	1.249
100	1.740	0.9606	4.216	0.294	0.680	10.029	1.500
80	2.22	0.9741	4.196	0.364	0.668	10.030	1.525
60	3.02	0.9855	4.184	0.478	0.651	10.030	1.706
40	4.34	0.9946	4.178	0.658	0.628	10.041	1.780
20	7.02	1.0000	4.182	1.006	0.597	9.374	1.476
0	13.60	1.0020	4.218	1.788	0.552	10.030	0.747

* Properties are in the saturated state [11].

n = 0.294 10^{-6} M^2/sec and Pr = 1.74.   It varies almost an order of magnitude over this range.

The present study did not intend to investigate the influence of property changes in full detail; however, the performance of axial heat flux versus water properties at temperature from 0°C to 200°C has been examined.

Though Model 2 may not be an ideal device (at large Δx) for the application of enhanced thermal pumping, it can, however, be a good model for demonstrating the influence of
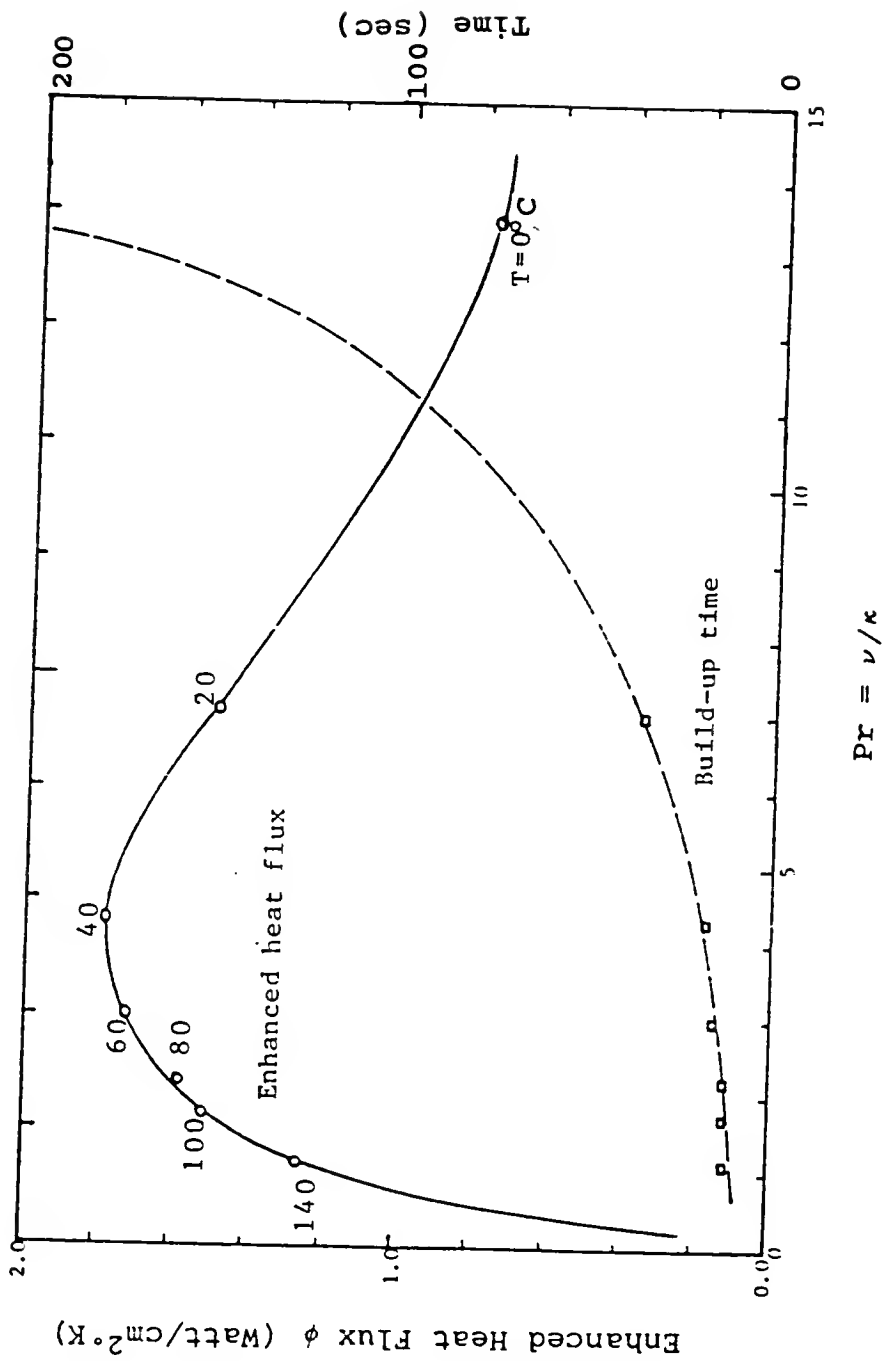
Fig 4-28   Influence Of Thermodynamic Properties of H_2O on the Enhanced Heat Flux (Model 2, $\alpha=1$, $\Delta x= 10$ cm)

the variation of the fluid properties on the heat transfer near the source area in oscillating pipe flow. We used the tidal displacement of $\Delta x = 10$ cm, which according to Fig. 4-27, lies in the maximum axial heat flux range. The enhanced heat flux of the final periodic state is shown in Fig. 4-28 by the solid curve as a function of the Prandtl number for water at different temperatures and also in the last column of Table 4-7. The dashed curve shown in Fig. 4-28 is the time needed to build-up to the final oscillation state. The Wormersley number used in the calculations was $\alpha = 1$.

According to the definition of Wormersley number given by equation (1-10), for a fixed α and pipe radius R_1, the angular velocity ω is directly proportional to the kinematic viscosity ν. This also implies that the fluid boundary layer thickness is constant (Eq. 1-2). So, the solid curve in Fig. 4-28, in fact, mainly reflects a relationship between the enhanced heat flux and the oscillating frequency ω. It is found that a maximum enhanced heat flux can be obtained if the water of approximate temperature $T = 40°C$ is employed. The corresponding angular velocity at this temperature level is $\omega = 0.658$ radian/sec. Physically, the existence of a peak value in Fig. 4-28, may be explained as follows: At higher temperature, say, $T = 100°$ C, the kinematic viscosity ν is quite small and hence the angular velocity ω is too slow to transport large amounts of heat axially. As the

temperature decreases, ν gets larger, and so does the angular velocity ω. Thus more heat can be expected to be transported and this eventually reaches the limit mentioned in the last section. It seems that a similar flattening pattern in the heat flux should also appear if the temperature is further decreased and hence the frequency ω further increased. However, as temperature decreases further the thermal conductivity declines (Table 4-7) so that it weakens the heat supply and removal capability at the sources and hence makes the axial heat flux curve decline from its maximum.

Heat Flux Versus Tidal Displacement (Model 1)

As indicated by Kurzweg in earlier analytic studies [16, 19, 20], the enhanced axial heat transfer versus the oscillating flow is directly proportional to the square of the tidal displacement. A series of numerical tests with Model 1 were run to check this prediction and to study the influence of various fluid properties and boundary conditions on this Δx^2 effect.

The computations were separated into two groups: in the first group, the Wormersley number was chosen very close to the tuning point, i.e., $\alpha = 1$. Water was chosen as the working fluid, and both insulating and conducting wall conditions (glass and steel) were considered. The computational results are shown in Fig. 4-29. In the second group of numerical studies, the Wormersley number was chosen
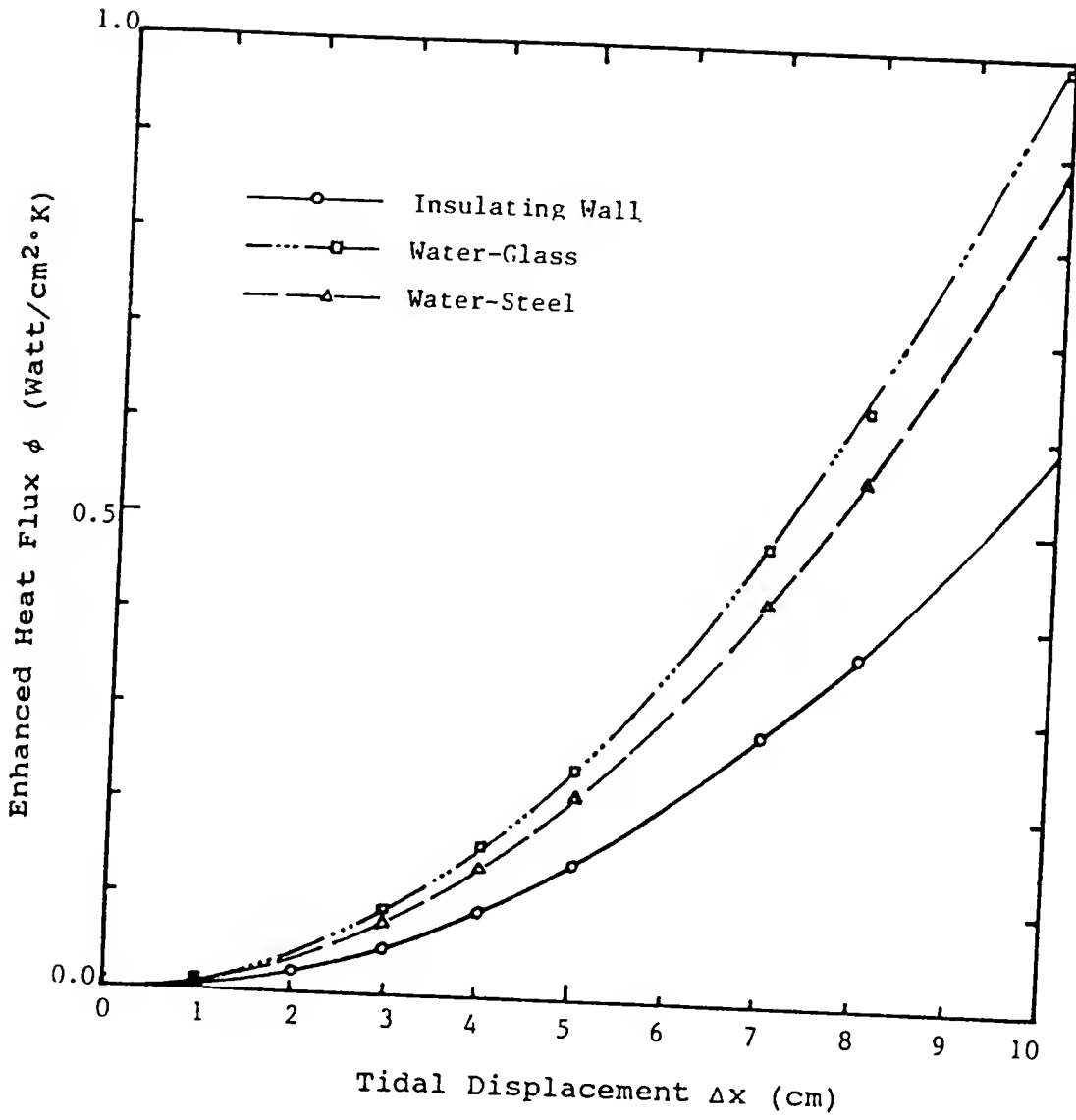
Fig 4-29   Heat Flux versus Tidal Displacement
(Model 1, $\alpha = 1$, Pr = 7.03)
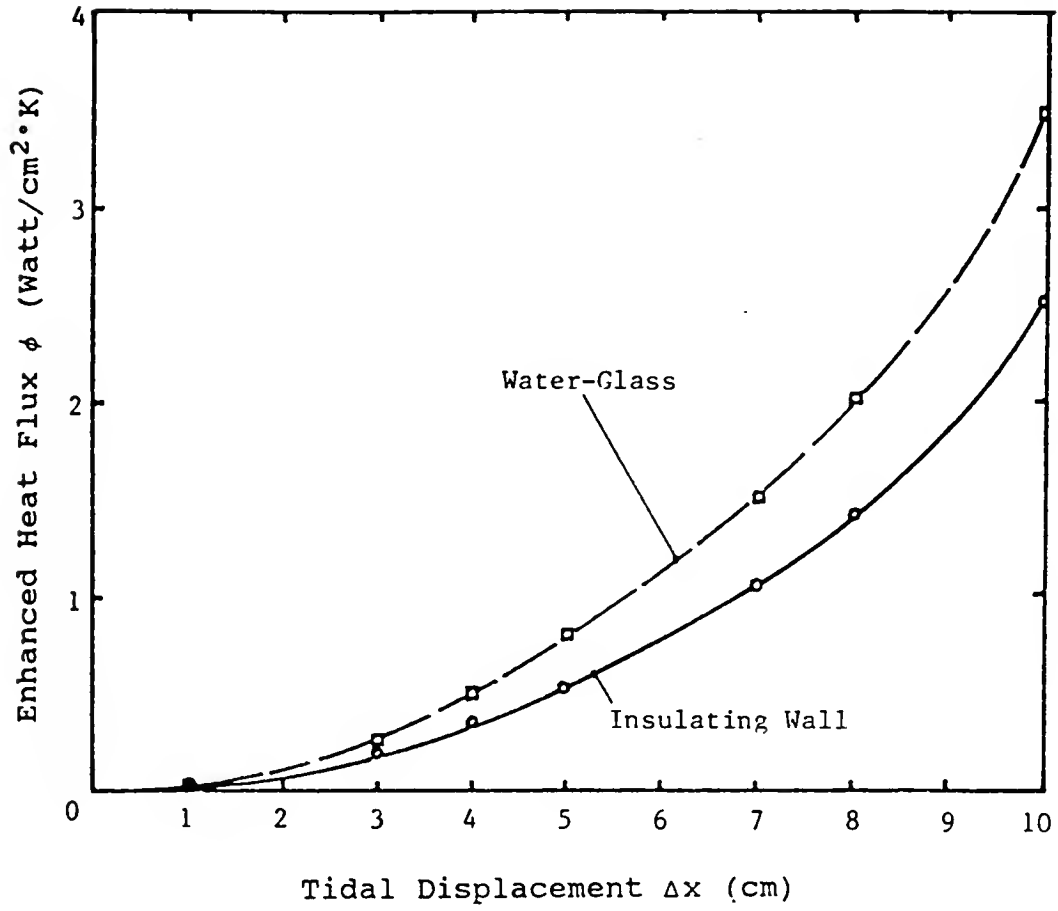
Fig 4-30   Heat Flux versus Tidal Displacement
(Model 1, $\alpha = 3$, Pr = 7.03)

as $\alpha = 3$, which deviates from the tuning point. Again water was chosen as the working medium. Similarly, both insulating wall and conducting (glass only) wall cases were investigated. The results are shown in Fig. 4-30. The solid curve (Fig. 4-29) shows the enhanced axial heat flux in oscillating pipe flow versus tidal displacement for the insulating wall case and the dashed curve represents the enhanced axial heat flux obtained with a steel wall. The " ---- • • • ----" curve shows the enhanced axial heat flux computed for a glass wall. These three curves clearly confirm the quadratic behavior,

$$\phi = k_\phi \cdot \Delta x^2$$

where $k\phi$ is a constant. For this specific case, it is found that

$k_\phi = 0.0056$ for the insulating wall case,

$k_\phi = 0.0086$ for the steel wall case,

$k_\phi = 0.0098$ for the glass wall case.

The computational results for the Wormersley number $\alpha = 3$ case are shown in Fig. 4-30. There the solid curve represents the enhanced axial heat flux in oscillating pipe flow with insulating wall, the dashed curve shows the glass wall results. Similarly, the coefficient k_ϕ in the quadratic formula is found to have the value

$k_\phi = 0.0233$ for the insulating wall case,

$k_\phi = 0.0317$ for the water-glass combination.

It is obvious that the existence of conducting walls tends to increase heat storage capacity and hence enhance the radial and axial heat transfer process. Thus one can expect a larger heat flux for conducting walls than for insulating walls at the same tidal displacement and Wormersley number. It can be seen from Fig. 4-29 and Fig. 4-30 that higher Wormersley number ($\alpha = 3$) will generally lead to a larger axial heat flux. In these specific cases higher Wormersley number simply implies higher oscillating frequency ω. However, it does not mean that the tuning point shifts to a Wormersley number equal to 3. Because here the enhanced axial heat flux is a dimensional quantity, if this quantity is divided by the oscillating frequency, one can clearly see that this new quotient is larger in the $\alpha = 1$ case.

If one compares the computational results obtained by using Model 1 in this section with the previously obtained results for Model 2 as shown in Fig. 4-27, one may at first glance feel somewhat puzzled at discrepancies between the results. Note, however, that there is an essential distinction between Model 1 and Model 2. In Model 1, the fluid elements have infinite heat exchange capability at both ends, in fact, all the new fluid elements with constant temperature (i.e., the reservoir's temperature) enter the pipe at both ends during every oscillating period. This implies that direct convective heat exchange occurs at these

ends during each oscillation so as to match the fast enhanced axial heat transfer possible within the pipe. On the other hand, for the Model 2 case, there is no such infinite heat exchange capability at the heat source and the sink sections. In fact, the heat being supplied and removed is purely by molecular heat conduction at the interface between of the thermal sources and the fluid boundary layer. This conductive heat supply and removal mode is not compatible with a very fast enhanced axial heat transfer within the connecting pipe flow and actually prevents the thermal process from working at peak efficiency. This comparison suggests to us that one should consider a strong and preferably turbulent convective motion in both end reservoirs as a means to increase the efficiency of the enhanced thermal pumping technique.

The Influence of Wall Thickness

As mentioned above, the conducting wall will, in general, make the enhanced axial heat transfer process more efficient since the existence of a conducting wall creates an additional heat storage capability near the fluid-solid interface. This additional heat storage supplements the storage capacity of the boundary layer and hence strengthens the enhanced heat exchange process of the whole system.

The largest radial distance which the heat can be transferred into the wall is the wall thermal penetrating thickness δ_w. This thickness is a function of oscillating

frequency as well as the thermal properties of the solid wall. As mentioned in the introduction chapter (Fig. 2-1), the future engineering applications of the thermal pumping technique probably will require a bundle of capillary tubes connecting the cold and hot fluid reservoirs. In view of space limitations and economics, one wants to minimize the capillary wall thickness used in the thermal pump yet still be able to make full use of the wall heat storage capacity.

Using Model 1, a numerical investigation of enhanced axial heat flux in oscillating pipe flow in a water-glass combination for various wall thicknesses has been performed and the computed results recorded in Fig. 4-31. In this study, the tidal displacement was taken as $\Delta x = 5$ cm ($= L/4$), the Wormersley number $\alpha = 1$, and inner pipe radius $R_1 = 0.1$ cm. Water at 20° C was used as the working medium. If we define the effective heat flux as the enhanced axial heat flux computed not only over the cross-section of the fluid in the pipe but also including the solid wall area, we can see from Fig. 4-31 that as wall thickness increases, the effective heat flux curve first increases with increasing wall thickness $R_2 - R_1$ but soon starts to decline. Apparently there is an optimum value of the wall cladding thickness. For this specific case, it has been found that this optimum wall thickness is about 10 percent of the pipe diameter. It also implies that the penetrating thickness δ_w into the wall in this case is about 0.02 cm, which is 20
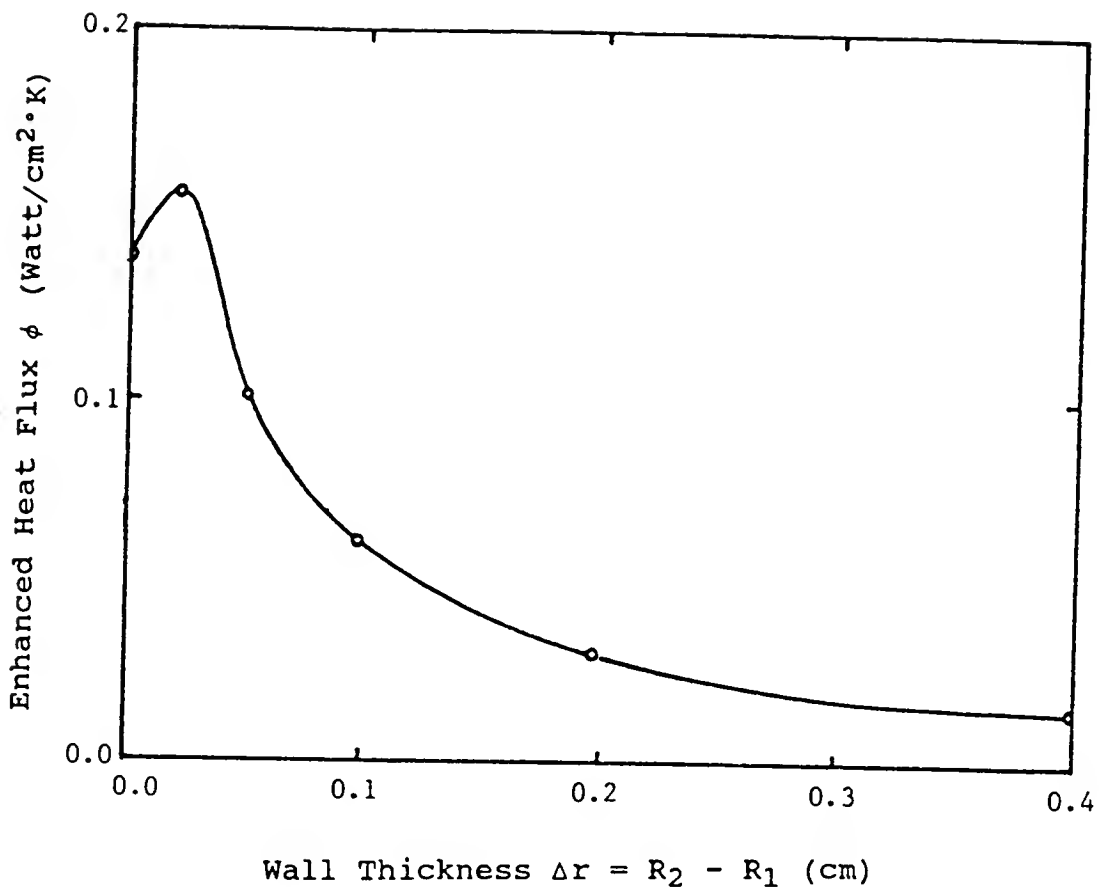
Fig 4-31   Influence of Wall Thickness on Axial Heat flux
(Model 1, Water-Glass, $\alpha = 1$, $\Delta x = 5cm$)

percent of the pipe inner radius. The decline of the effective heat flux curve is due to the "unpenetrated" outer part of the wall which plays a useless role in the enhanced heat axial transfer process.

The Influence of Pipe Diameter

Another very important aspect of the heat transfer technique under consideration is the performance of heat flux versus pipe diameter. A numerical simulation with Model 3 has been carried out to examine the pipe diameter effects. For the test the Wormersley number was taken as α = 3, the tidal displacement Δx = 10 cm, and the fixed wall thickness equal to 0.05 cm. Once again 20°C water was taken as the working fluid and the wall material was glass.

From the definition of Wormersley number (1-10), namely, $\alpha = R_1\sqrt{\omega/\nu}$, it is clear that the oscillating frequency is inversely proportional to the second power of pipe inner radius for fixed Wormersley number and directly proportional to the kinematic viscosity of the working fluid. On the other hand, the enhanced axial heat flux is an increasing monotonic function of the oscillating frequency. This implies that an increase in inner pipe diameter will surely lead to a decline of oscillating frequency and hence the enhanced axial heat flux, if both Wormersley number and the kinematic viscosity are held constant. The numerical results are shown in Fig. 4-32.
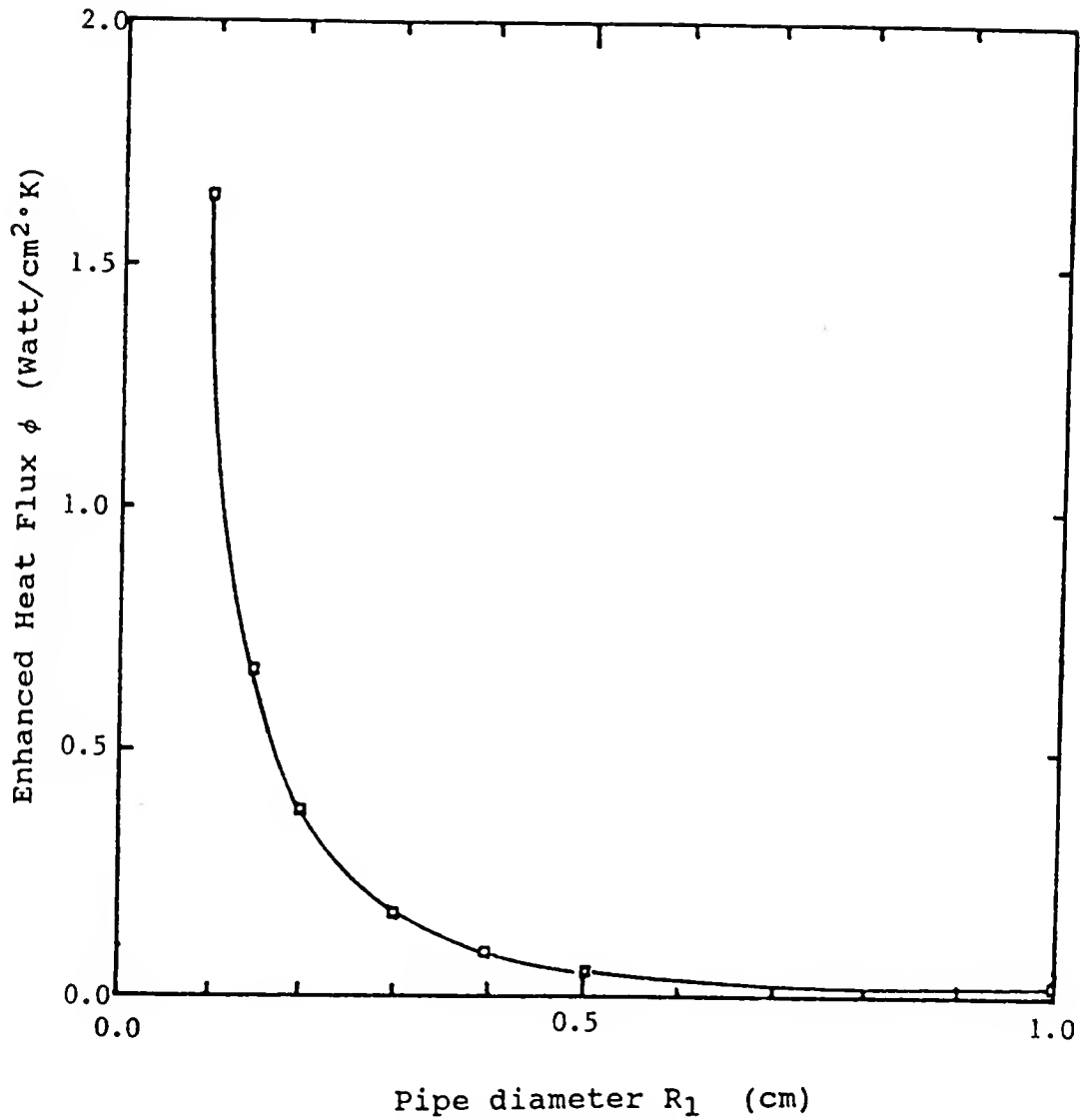
Fig 4-32   Influence of Pipe Diameter on Heat flux for Fixed
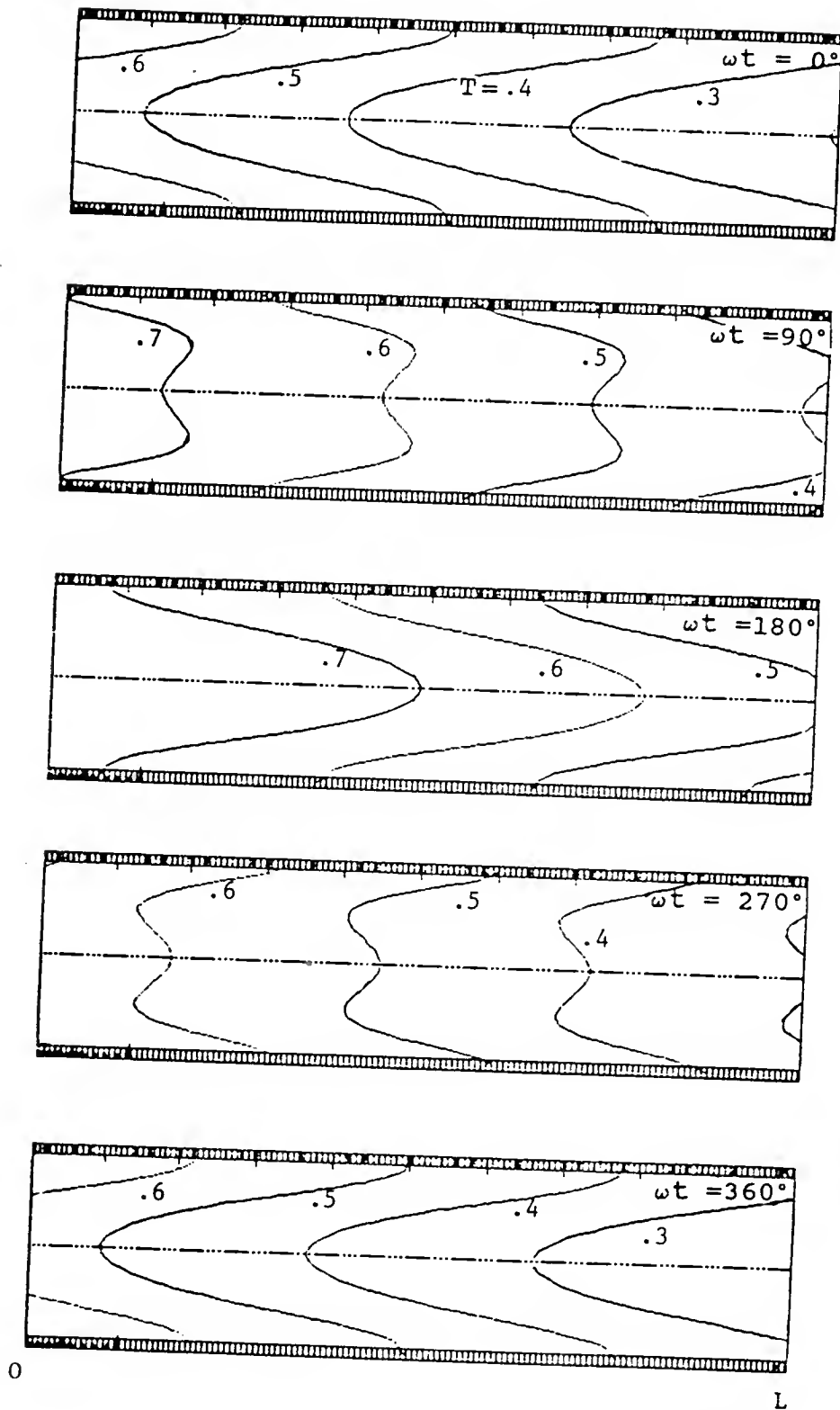   Frequency (Model 3, Water-glass, $\alpha = 3$, $\Delta x = 10$cm)

Fig 4-33   Typical Iso-Temperature Contour
              in Oscillating Pipe Flow
       (Model 3, α = 3, Δx = 10cm, R_1=0.1cm, R_2=0.5cm)

It will be noted that the ϕ versus R_1 curve does not show a decrease in enhanced axial heat flux as the radius becomes very small. It is expected from the early analytic work that there exists an upper limit of the enhanced axial heat flux as the inner pipe diameter becomes extremely small. This is because that when the pipe cross-section area is further decreased such that the central slug flow volume which transports heat back and forth axially becomes very small, the heat transfer mechanism of the thermal pumping technique is destroyed since large radial temperature gradients are no longer possible.

Fig. 4-33 shows iso-temperature contours for a pipe diameter equal to 0.5 cm. The iso-temperature contours show a periodic temperature pattern within an oscillation period. It is noted that the contours at phase angles $\omega t = 0°$ and 180° or 90° and 270° are not precisely anti-symmetric.

Variation of Axial Temperature Gradient in Model 3

In order to overcome the numerical instabilities observed near the pipe ends in Model 1 and to examine the effect of no convective heat exchange at the pipe ends, Model 3 which is shown in Fig. 2-4, was developed and studied.

The first numerical study carried out with this later model was to examine the variation of the time-averaged axial temperature gradient within the central pipe section as the tidal displacement was increased. This time-averaged
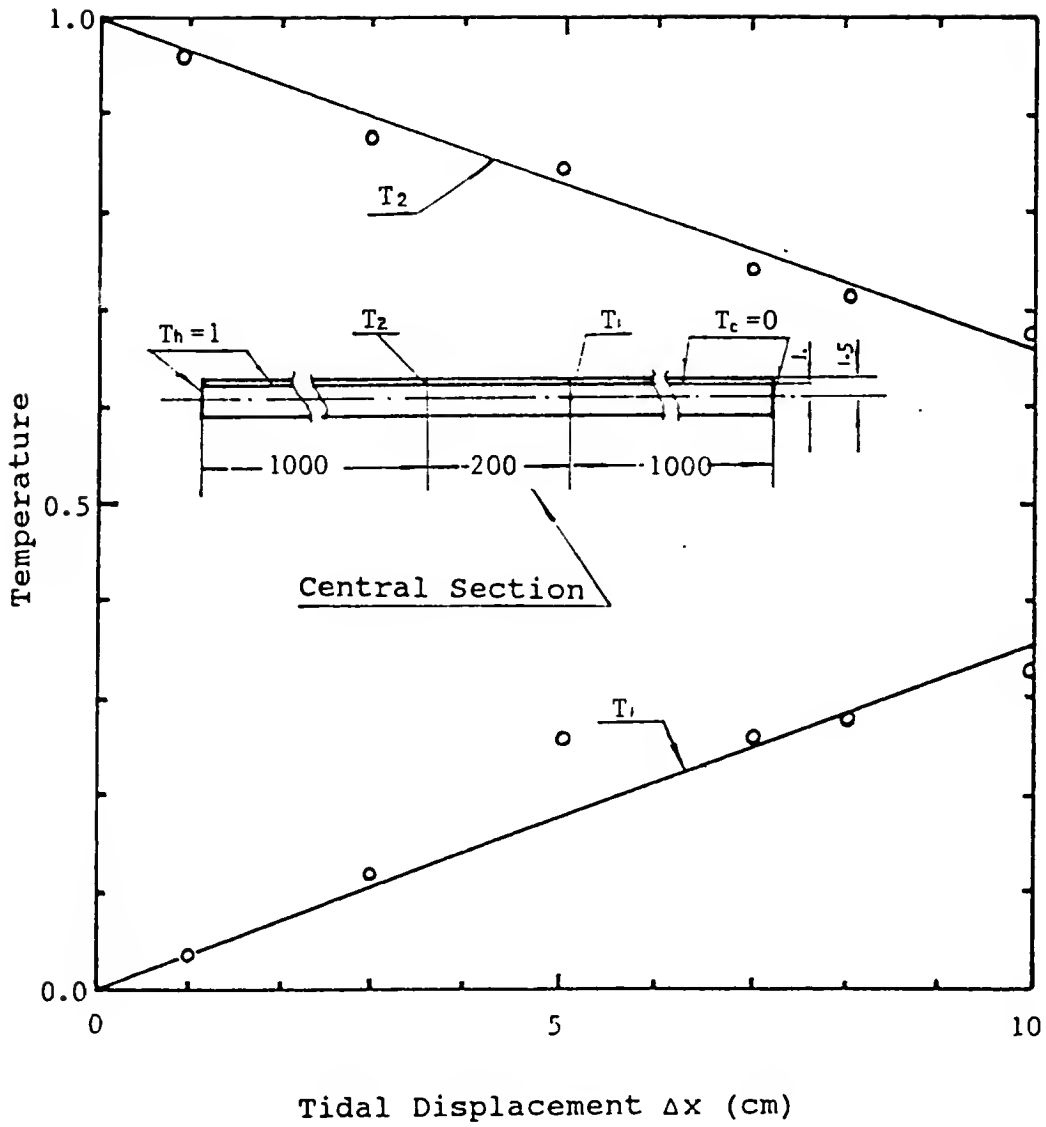
Fig 4-34   Variation of Temperature T_1 and T_2 versus Δx
(Model 3, Water-Glass, $\alpha = 3$)

axial temperature gradient variation can be calculated by measuring the time-averaged temperatures at the joint points (x = 5L, and 6L, see Fig. 2-4). The computed results are shown in Fig. 4-34. In the calculation, the Wormersley number was chosen as α = 1 and the working medium is water within a glass pipe. In the figure, T_2 is the time-averaged temperature computed at the left joint (x = 5L) which is close to the hot source, while T_1, at right joint, is close to the cold source. It is clearly seen that T_2 decreases, while T_1 increases as the tidal displacements increase. It seems that both T_1 and T_2 tend to the dimensionless mean value (i.e., 0.5) if the tidal displacement is greatly increased. This implies that the time-averaged axial temperature gradient in the central section will decrease and that the enhanced axial heat flux will be weakened

Table 4-8 Variation of the Axial Temperature Gradient versus Wormersley Number (Water-Glass, Δx = 10 cm) (T_1, T_2.... are dimensionless Temperatures)

α	At Periods	T_2	T_1	$\Delta T=T_2-T_1$
1	29	0.622	0.387	0.235
4	39	0.705	0.295	0.411
10	38	0.788	0.213	0.575
20	38	0.853	0.149	0.704

although still increasing with increasing Δx. However, the numerical results show that such a weakening of the axial temperature gradient can be improved at higher oscillating frequency (Table 4-8). This is because at higher ω the pipe flow develops a much thinner boundary layer in the vicinity of the wall and hence a larger radial temperature gradient which increases the capability of heat supply and removal from the extended sections. In fact, the numerical results also show that only very narrow areas of the extended section are involved in supplying and removing heat when the oscillating frequency is large (Fig. 4-25).

Comparison of Enhanced Oscillatory Heat Transfer
and Heat Conduction

Fig. 4-35 shows the enhanced axial heat flux computed in the central pipe section in Model 3 and the axial molecular conduction heat flux both in the fluid and in the wall versus tidal displacement. The Wormersley number in the test case is chosen as $\alpha = 3$, the working medium is water, and the solid wall material is glass. Curve ϕ represents the variation of enhanced axial heat flux versus the tidal displacement. This is seen to be smaller than the heat flux due to pure molecular conduction either in the wall (curve ϕ_w) or in the fluid (curve ϕ_f) when the tidal displacement is very small (Δx less than 1 cm in this case), however, ϕ increases dramatically when the tidal displacement becomes larger. In contrast, the pure axial molecular conduction declines slightly due a weakening of
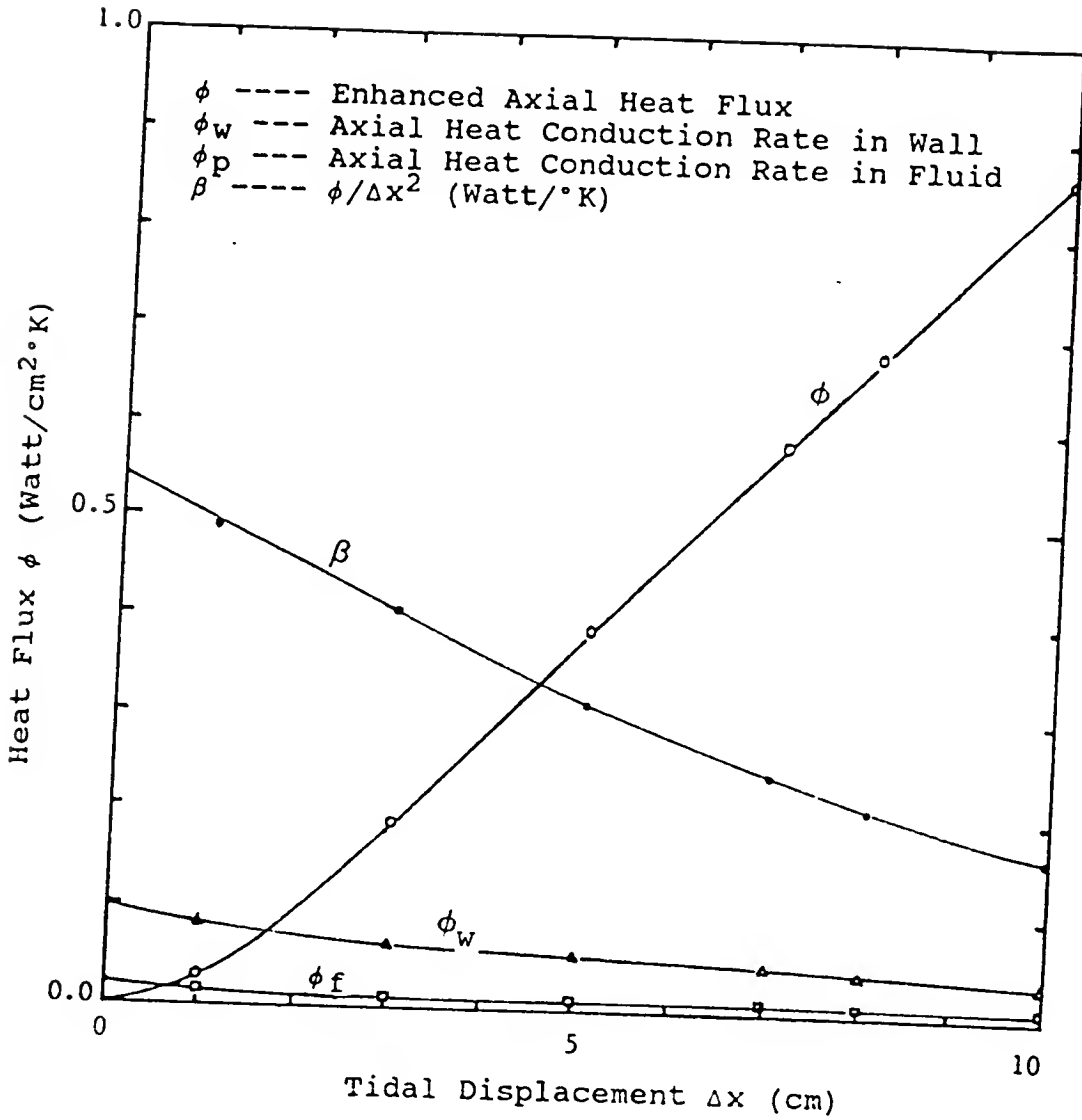
Fig 4-35   Comparison of Enhanced Heat Transfer and Heat
Conduction in Oscillating Pipe Flow
(Model 3, Water-Glass, α = 3)

the axial temperature gradient in the central pipe section at large Δx as discussed in the last section.

The ratio of the enhanced heat flux to the square of the tidal displacement is also shown in the same figure (curve β). It indicates a declining value of β as the tidal displacement increases. This indicates that the 2nd power relationship between the enhanced axial heat flux ϕ and tidal displacement Δx has also been weakened (i.e., lower k_ϕ) if large tidal displacements are used.

Enhanced Heat Flux as a Function of Wormersley Number

To study the influence of oscillating frequency on the enhanced axial heat transfer, a series of numerical tests were performed with Model 3 for various combinations of water-steel and mercury-steel cases. Fig. 4-36 shows the enhanced axial heat flux and the heat flux by pure molecular heat conduction both in the fluid and in the wall as a function of Wormersley number (i.e., a function of oscillating frequency ω, for fixed pipe radius and working fluid).

The solid curves show the computed results in the water-glass wall case, while the dashed curves represent the numerical solution obtained with the mercury-steel wall combination. The tidal displacement Δx used in these calculations is fixed and equals 10 cm. The subscripts have the same meaning as those used in Fig. 4-35.
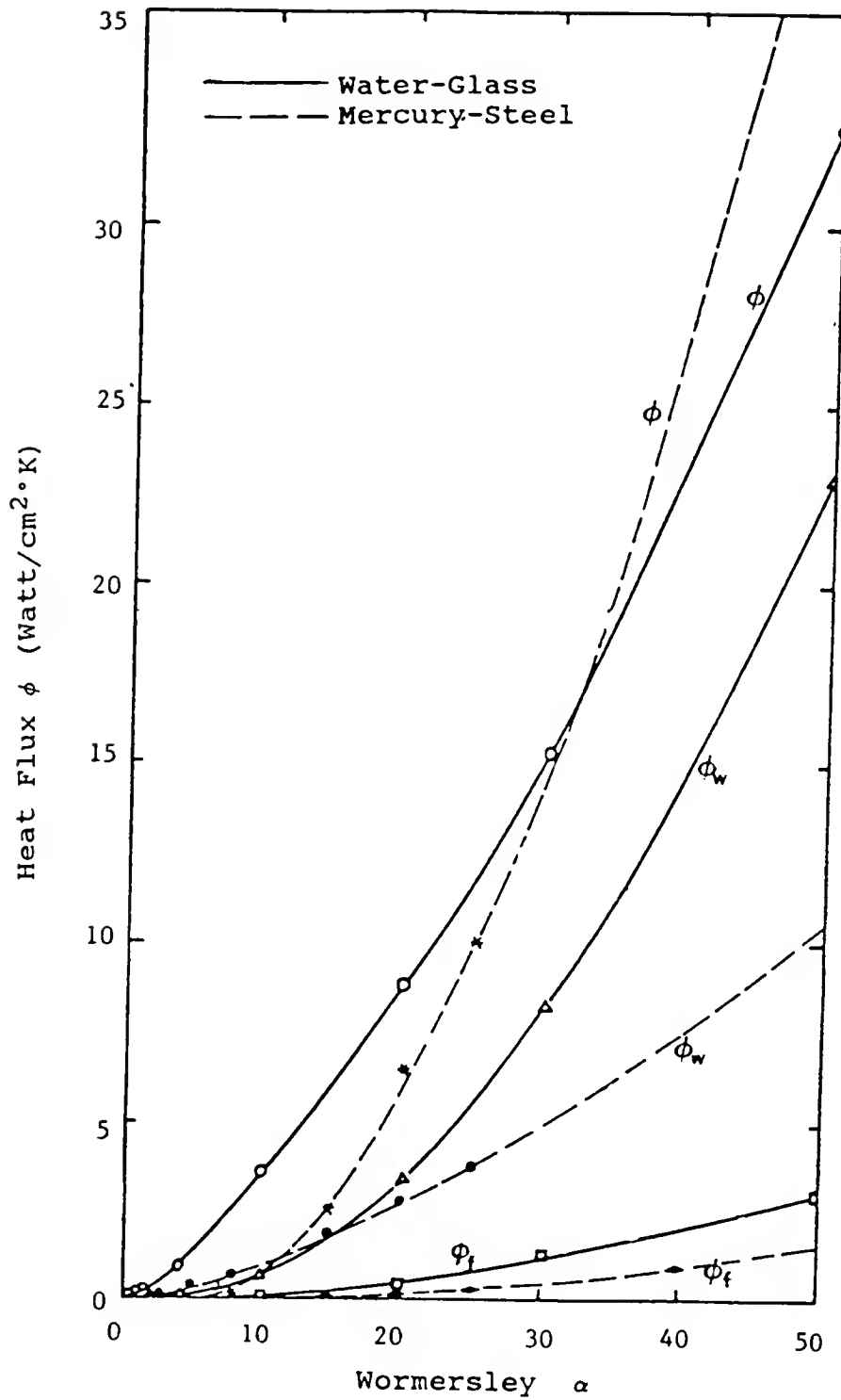
Fig 4-36   Variation of Axial Heat Flux Versus Wormersley
Number (Model 3, Δx = 10cm)

It can be seen from Fig. 4-36 that both the enhanced axial heat flux ϕ and axial heat flux due to pure molecular conduction in either the wall (ϕ_w) or in the fluid (ϕ_f) increase as the oscillating frequency gets larger. It is assumed that this is partially due to the recovery of the axial temperature gradient when the oscillating frequency increases as discussed in the previous section. It can been also seen that the enhanced axial heat flux is larger than the axial heat flow by pure molecular conduction in either case. The difference between the enhanced axial heat flux and the axial heat flux due to pure molecular conduction in the water-steel wall case is smaller than that in the mercury-steel case. This implies that the water-steel combination does not take optimum advantage of the enhanced thermal pumping process. The axial heat flux due to pure molecular heat conduction in the fluid, in general is very much smaller than the enhanced axial heat flux and hence is indeed negligible as assumed in the theoretical analysis of this problem.

Note that if the dimensional enhanced heat flux is divided by the corresponding oscillating frequency, we will obtain the tuning curves which will be discussed below.

Tuning Curves

In Fig. 4-37, the left curve shows the variation of the ratio of the enhanced axial heat flux ϕ to the oscillating frequency ω in the water-glass wall case, while
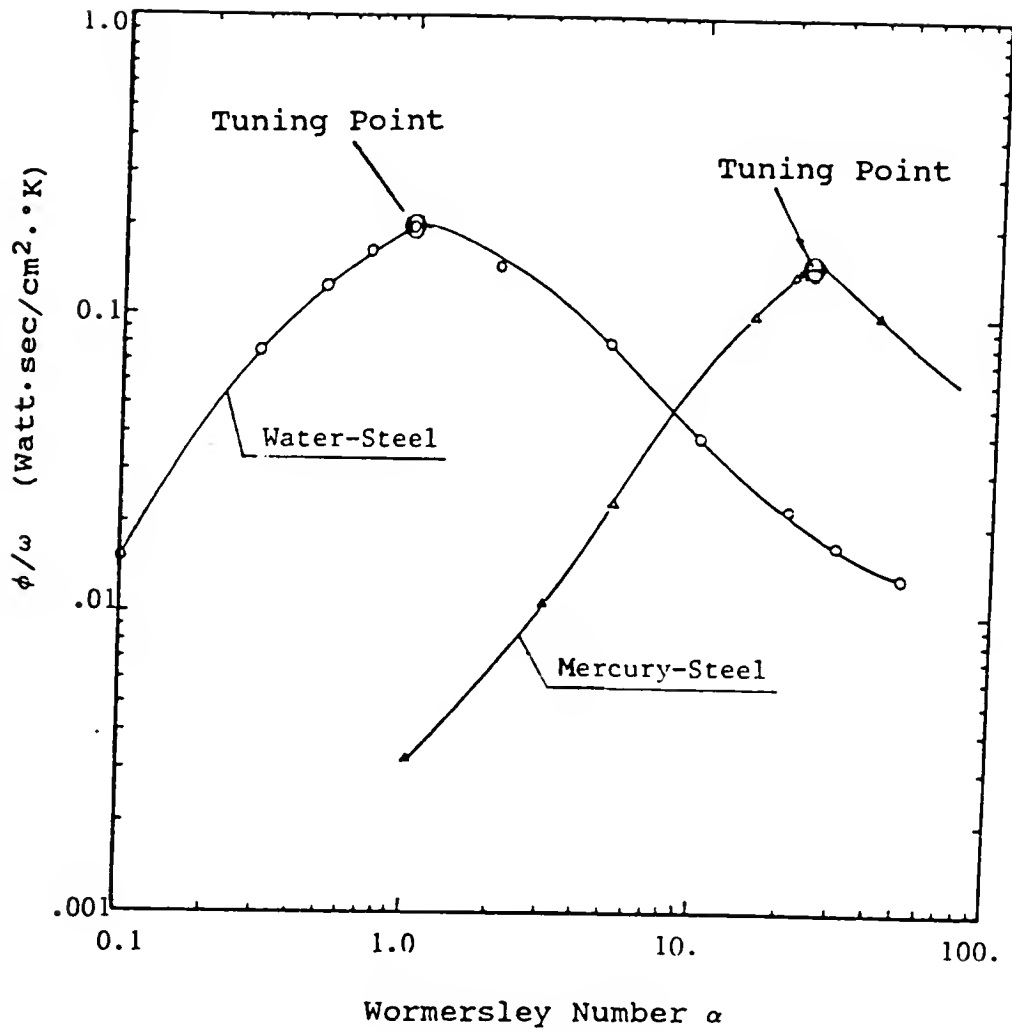
138

Fig 4-37   Computed Tuning Curves
(Model 3, H$_2$O-Steel and Hg-steel, Δx = 10cm)

the right curve represents the mercury-glass wall case as marked in the diagram. It can be seen that both curves show the existence of the so-called tuning effect. The optimum value of R_1 for the water-glass case (Pr = 7.03, ω = 1/sec) is found equal to 0.1 cm, and the corresponding Wormersley number is about 1.

Fig. 4-38 shows some analytical results obtained in reference [20, 21], There the optimum value of α for a Prandtl number Pr = 10 is close to 1. The slight difference in tuning peak is due to the use of a flat plate channel geometry and different thermal wall boundary conditions in the analytic investigation.

It is to be emphasized that the correct tuning condition under various combinations of working fluid and solid wall material is a crucial point in the design of practical devices using the enhanced thermal pumping technique. This is because the enhanced axial heat flux which is usually orders of magnitude higher than the axial heat flow produced by pure molecular conduction occurs only near the tuning point and hence at a fixed radius for a fixed value of ω. Once the tuning point has been found, one can select the appropriate pipe diameter to optimize the heat transfer process.

We will demonstrate the above points in another way. Fig. 4-39 shows the ratio of the axial heat flux by pure molecular heat conduction in either the oscillating fluid or
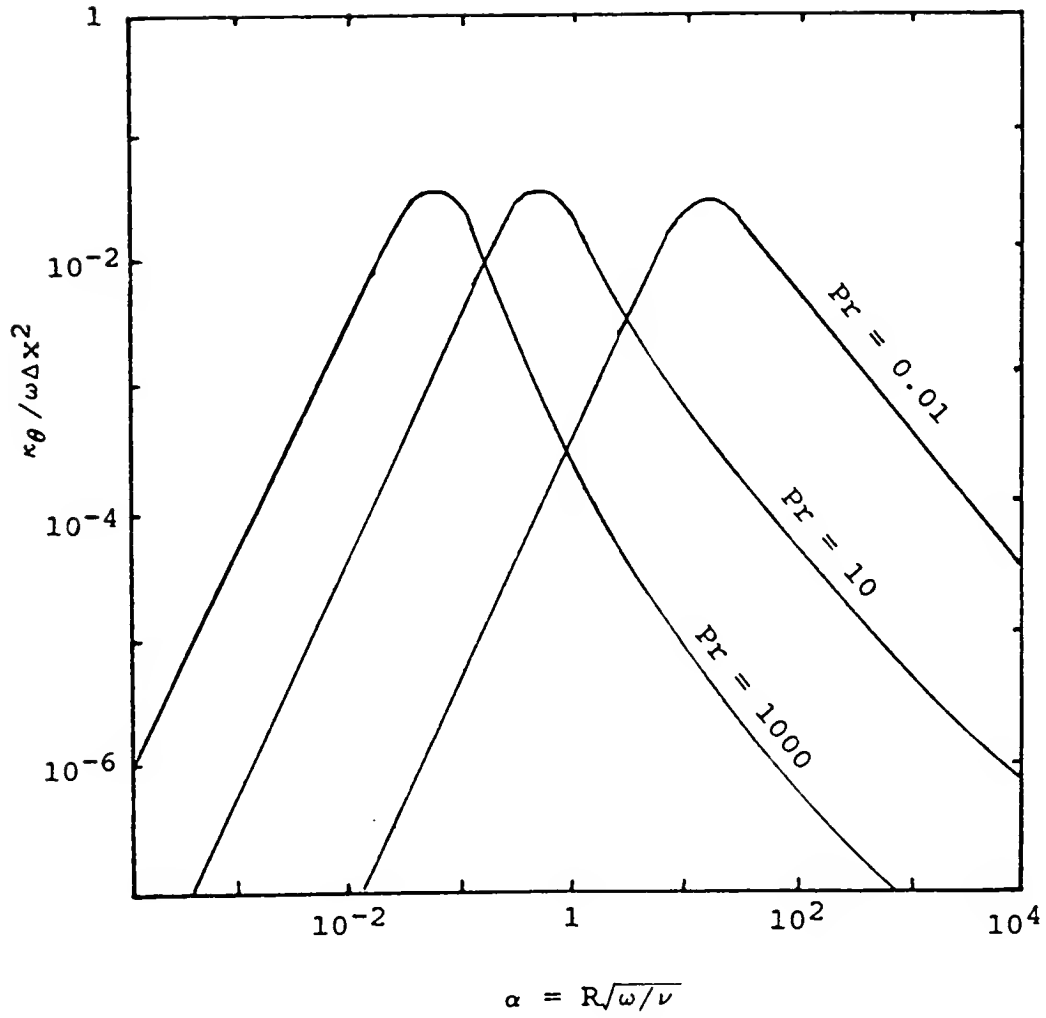
Fig 4-38   Tuning Curve versus Wormersley Number
(after Kurzweg, [16])
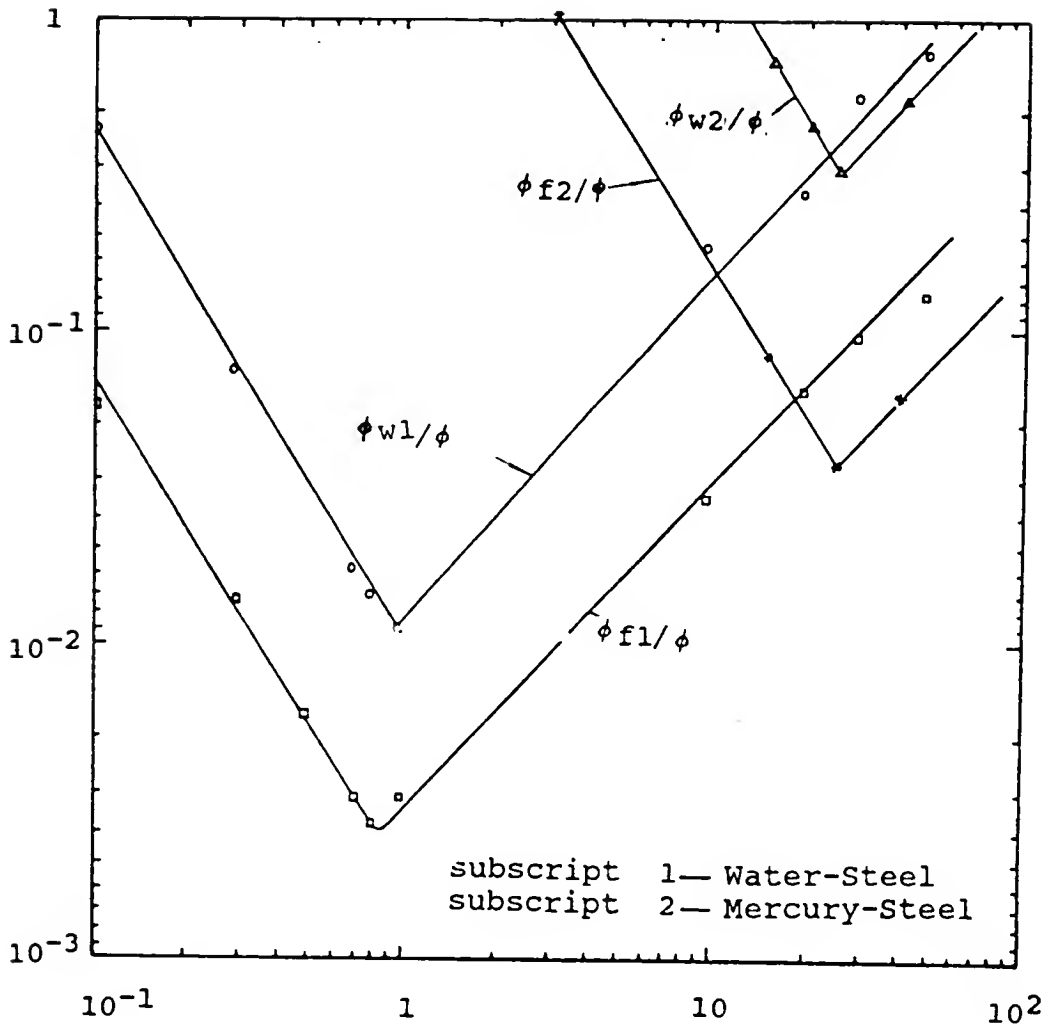
Wormersley Number $\alpha = R\sqrt{\omega/\nu}$

Fig 4-39   Ratio of Heat Conduction to Enhanced Heat Flux
Versus Wormersley Number
(Model 3, H_2O-Steel, Hg-Steel, $\Delta x = 10cm$)

in the solid wall to the enhanced axial heat flux for both the water-glass and mercury-steel combinations. These curves look like up-side-down tuning curves. They clearly show that only at or near the tuning points the axial heat flux generated by the pure molecular heat conduction either in fluid or the conducting wall is quite small compared to the enhanced heat flux and hence negligible (about $5 \; 10^{-3}$ for the water-steel wall case, and about $5 \; 10^{-2}$ for the mercury-steel wall case). However, if one departs from the tuning point this ratio grows quickly and eventually may be greater than 1. The tube radii corresponding to the tuning points ($\alpha = 1$ for water-steel, $\alpha = 15$ for mercury-steel) at $w = 25$ rad/sec, correspond to $R_1 = 0.02$ cm for water-steel and $R_1 = 0.1$ cm for mercury-steel.

CHAPTER V
CONCLUDING REMARKS

We have attempted to present a systematic numerical investigation of enhanced axial heat transfer in oscillating pipe flow for both insulating wall and conducting wall cases. As has been shown in Fig. 1-1, the pipes which connect both reservoirs are the most important elements in such enhanced thermal pumping devices and the performance of the oscillating fluid within the pipes will determine to a large extent if such devices are practical for a given application such as cooling of micro-circuits or the removal of heat from nuclear reactors without associated convective mass exchange.

The governing differential equations derived in chapter II are based on the assumption that viscous dissipative terms in the energy equation are negligible compared to the convective term UT, and that the final oscillating flow can be well approximated by a 1-D laminar oscillating flow with constant thermodynamic properties.

The numerical calculations presented in this dissertation obtain solutions by breaking up the governing equations into their finite difference form and solving the momentum equation with the Crank-Nicolson technique, and the

energy equations with a time dependent Alternating Direction Implicit method (ADI). A computer code named ETP (Enhanced Thermal Pumping) was developed to implement the calculations. It is documented in the appendix.

The physical mechanism for the enhanced thermal pumping technique in oscillating pipe flow is an interchange of heat between the core slug flow and the boundary layer and the bounding conducting wall. In fact, the process acts very much as an enhanced molecular diffusion process in which the tidal displacement Δx plays a role similar to the phonon mean free path in the molecular conduction and the existence of large radial temperature gradients, orders of magnitude higher than those existing axially, allow very large radial conductive fluxes. Since the macroscopic distance Δx is orders of magnitude larger than the molecular mean free path, it is not surprising that axial heat flows orders of magnitude larger than those possible by conduction in the absence of oscillations become possible.

This enhanced thermal pumping technique is especially suited for those problems where it is desirable to transport large amounts of heat without an accompanying convective mass exchange. The removal of heat from radioactive fluids would appear to be ideally suited for a heat transfer device based on this enhanced heat exchange technique.

Three Models of different configuration were examined numerically in detail. Model 1 was employed to simulate

constant pipe end temperature conditions as widely used in theoretical studies. The performance of oscillating pipe flow with this model has been examined numerically and the computations well justify the existing analytical approximations used. It is now clearer that the tuning condition and a large maintained axial temperature gradient between pipe ends is crucial for an optimal functioning thermal pump. It was found that the enhanced axial heat flux achievable with this model is indeed very large and can exceed by orders of magnitude the heat flux possible by pure heat conduction between the pipe ends. The enhanced axial heat flux for this geometry is proportional to the second power of the tidal displacement for both the conducting wall and insulating wall case and with either water or mercury as the working medium (Figs. 4-29, and 4-30). The proportionality coefficients between ϕ and Δx^2 have been found for the above mentioned test cases. Unfortunately, with the present second order numerical method, the numerical solutions were distorted primarily by dispersion error at both pipe ends where a discontinuity of the physical properties occurs as Wormersley Number and/or tidal displacement become large.

Model 2 was designed to examine the properties of an alternative thermal pump design of potential use in micro-circuit cooling. Such a configuration was successful in transferring large quantities of heat between the iso-

thermal side wall sections and the fluid when small tidal displacements were used. However, a limit on the increase of axial heat flux with increase in tidal displacement exists in both the oscillating and steady flow cases in this model and the quadratic relationship no longer holds when the tidal displacement becomes large because of an incompatibility of large time-dependent axial heat transfer in the thermal pumping process and the capability of the thermal sources to supply and remove sufficient heat by thermal conduction. Nevertheless, it made us pay more attention to a study of the heat exchange problem at the end points of the pipes where they connect to fluid reservoirs. Since an effective enhanced thermal pump produced by oscillating pipe flow requires rapid heat supply and removal at both pipe ends any configuration unable to do this will not allow one to take full advantage of the process.

To investigate the influence of the heat supply and removal at the pipe ends, Model 3 was constructed by adding very long conductive extensions at both ends of the central pipe section. This model simulates the situation of oscillating pipe flow for which no convective heat exchange occurs in the end reservoirs but large areas for conduction heat transfer are made available. Numerical results show that the effective enhanced axial heat transfer is greatly weakened over that achievable by good convective mixing at the pipe ends. The reason is again that, even with an

enlarged heat source size (pipe extension) it is still not able to match the very fast enhanced axial heat transfer possible in the connecting pipe. It is found that constant end temperature (at x = 5L and 6L) can not be maintained and the quadratic relationship between the enhanced heat flux and the tidal displacement will no longer hold (Fig. 4-35). However, even with this model, the numerical results show the tuning point concept exists. For water, this tuned value occurs at about Wormersley number $\alpha = 1$. It is also shown that, under tuned conditions, the enhanced axial heat transfer is orders of magnitude larger than that possible by pure molecular conduction. However, any deviation from the tuning condition will greatly decrease the effectiveness of the enhanced thermal pumping.

A study on the influence of wall thickness and pipe diameter on enhanced heat transfer was performed. The numerical predictions show that for water, small pipe diameter will be beneficial and the optimum wall thickness should be about 20 percent of the pipe inner radius for the case considered (i.e., for inner pipe radius of $R_1 = 0.1cm$ the best outer pipe radius should be chosen as $R_2 = 0.12cm$). The influence of the variation of thermal and viscous properties of working fluid on the axial heat flux has also been studied. The numerical solutions show that even in the relatively narrow temperature range from 0°C to 100°C, the axial heat flux varies more than 150 percent.

Extensions of the numerical studies considered here should include: 1) developing a 3-D or at least an axisymmetric 2-D model which is able to best approximate the entire system including both reservoirs so that one may more accurately study the effect of heat exchange within the reservoirs; 2) the role of turbulence in such oscillating flows at high frequency ω and tidal displacement Δx should receive special attention as well as the inertia forces that are known to become large at higher oscillating frequency. In fact, a turbulent modelling is necessary especially if the study includes heat source and heat sink reservoirs; 3) a consideration of the variation of the thermodynamic properties of working fluid with temperature and hence spatial position should also be included in any extension of this research on enhanced heat transfer by oscillations of viscous fluids in pipes.

APPENDIX
ETP COMPUTER CODE

An axisymmetric code with designation ETP has been developed for computing the time-dependent Enhanced Thermal Pumping problem with either oscillating flow (pipe or flat plate) or steady flow. The grid is generated with a clustering in those regions where high velocity and temperature gradients are expected. Both Model 1 and Model 3 geometry are programed in the current code. Another separate code (MIXPIP) is also available for the Model 2 geometry which is not discussed in this appendix.

Description of Input Variables

The following statements are used in the ETP code:

```
        READ (5,10) NMAX,KMAX,JMAX,ICLUS,IPIPE,IPRES
        READ (5,10) KMID,IREAD,JPER,ICH
        READ (5,20) DS,RMUK,ROU,CP,RKS,CKS
        READ (5,20) ALFA,PR,RL,T01,T02,AMP
        READ (5,20) RAD, RAD1,RLEND,UEPS,TEPS
        READ (5,10) (IH(I),I=1,ICH)

10      FORMAT (8I10)
20      FORMAT (8F10.5)
```

where:

NMAX .... total time steps within one period

KMAX .... total nodal points on radius

JMAX .... total nodal points on axis

ICLUS = 0 .. grid with clustering

    = 1 .. uniform Grid

IPIPE = 0 .. Pipe geometry

    = 1 .. 2-D Flat plate geometry

IPRES = 0 .. sinusoidal pressure gradient

    = 1 .. constant pressure gradient

KMID .... node index at interface along radius

        KMID = KMAX......insulating wall

            < KMAX......conducting wall

IREAD = 0 .. start a new job

    =-2 .. start flow part only

    = 2 .. start heat part only

       (based on existing flow variables)

    = 1 .. restart both flow & heat field calculation

    = 5 .. restart flow field calculation only

JPER.........number of period in the current run

ICH = 1 .... Model 1

   = 4 .... Model 3

DS .... distance of grid next to wall

RMUK .... kinematic Viscosity of fluid

ROU .... density of fluid

CP .... specific heat of fluid

RKS .... thermal diffusivity of solid wall

CKS .... heat conductivity of wall

ALFA .... Wormersley number

PR .... Prandtl number

RL .... Length L of pipe or flat plate

TO1 .... Temperature in the hot reservoir

TO2 .... Temperature in the cold reservoir

AMP .... The amplitude of axial pressure gradient

$$AMP = -(1./ROU)*DP/DX$$

RAD .... inner radius of pipe

RAD1 .... outer radius of pipe

RLEND ...... each extension portion length

UEPS........the allowance velocity residual

TEPS........the allowance temperature residual

IH(I) ...... node index of separating segments in Model 3

Note:

to run and restart a job with this code, one of the procedures has to be followed:

    1) IREAD = 0 ..... start both flow & heat field

         = 1 ..... restart both flow & heat field

    or

    2) IREAD =-2 ..... start flow field only

         = 2 ..... start heat & restart flow field

         = 1 ..... restart both flow & heat fields

A Sample Input Data and Batch Command File

The following sample input was used in the computation with Model 3 (water-glass)

1001	15	101	0	0	0
15	0	2	4		
0.40000	0.01006	0.99820	4.18181	0.20260	0.73000
10.00000	7.02000	20.00000	1.00000	0.00000	29270.600
0.10000	0.15000	100.00000	0.00500	0.00500	
1	21	81	101		

The following Command file was used to start the run of a new case:

```
$ ASSIGN SAMPL0.INP FOR005
$ ASSIGN SAMPL0.DAT FOR006
$ ASSIGN FILE7.DAT FOR007
$ ASSIGN FILE8.DAT FOR008
$ ASSIGN FILE11.DAT FOR011
$ R EPT
```

To restart the previous run, the following command file was used:

```
$ RENAME FILE7.DAT FILE9.DAT
$ RENAME FILE8.DAT FILE10.DAT
$ RENAME FILE11.DAT FILE12.DAT
$ ASSIGN SAMPL1.INP FOR005
$ ASSIGN SAMPL1.DAT FOR006
$ ASSIGN FILE7.DAT FOR007
$ ASSIGN FILE8.DAT FOR008
$ ASSIGN FILE9.DAT FOR009
$ ASSIGN FILE10.DAT FOR010
$ ASSIGN FILE11.DAT FOR011
$ ASSIGN FILE12.DAT FOR012
$ R EPT
```

Note, the name of the data files could be changed according user's taste.

Function of Subroutine in ETP Code

In the ETP code, the Program MAIN controls the main loop in the computation, including the input and output data control, restart control. Also it sets up the initial condition according to the purpose of investigation. The ETP code includes 22 subroutines. The function of each subroutine is listed below:

Subroutine COMMENT

This subroutine gives the description of the input and output variables listed in previous section.

Subroutine GRID

This subroutine is used to generate either a uniform or a clustered grid system in the physical domain for Model 1 or Model 3; it calls the subroutine CLUS to cluster the grid lines in the vicinity of wall and the central part of pipe (Model 3). It also calls subroutine METPIP, METWAL to compute the derivatives terms in the transformation.

Subroutine CLUS (ICLUS,K2)

This subroutine is called by GRID to compute the clustering grid distribution with equation (3-52).

Subroutine METPIP

This subroutine is called to compute the derivatives of the coordinate transformation in the inner pipe area. Such as $\partial x/\partial \xi$, $\partial x/\partial \eta$ ..... used in equations from (3-6) to (3-16) as well as in the boundary condition.

Subroutine METWAL

Similarly, subroutine METWAL is called with the same equations to compute the derivatives in transformation in the solid wall, if a conducting wall is assumed.

Subroutine FLOW (N)

This subroutine is called to compute the velocity in the flow field at each time step with the Crank-Nicolson Method. Equation (3-20) or the matrix form (3-28) will be solved in this subroutine.

Subroutine TIDAL

This subroutine is called to Compute the Lagrangian

displacement (2-33), tidal displacement(2-32) and the phase lags which are relative to the exciting pressure gradient phase.

Subroutine COFLOW

This subroutine is called to compute the coefficients in the momentum equation at each time step, i.e., computing equations (3-7) and (3-8).

Subroutine RHSFLO (N)

The subroutine RHSFLO (N) is called to compute the update right hand side terms in the momentum equation at each time step, i.e., equations from (3-21) to (3-25).

Subroutine TRID

A subroutine TRID (borrowed from [2]) is to solve the tridiagonal system algebra equations, it is widely used to compute the update velocity and temperature.

Subroutine EPSIL

Function EPSIL (borrowed from code "GRIDGEN") to find the ϵ value used in equation (3-52) with Newton-Raphson root-finding technique.

Subroutine ADISU3

This subroutine is called using ADI method to compute the temperature distribution in oscillating pipe flow in Model 3. The insulating wall boundary condition is assumed in the central pipe (5L < x < 6L) with fixed temperature at the far ends of both extension pipe. Equations from (3-29), (3-35), or the matrix from (3-33), (3-39) are solved.

<u>Subroutine COTPIP</u>

This subroutine is called by ADISU3 to calculate the coefficients in the energy equation of pipe flow (3-41) at each time step, which are coupled by the update velocity.

<u>Subroutine RHSINT (N,II,LINE)</u>

This subroutine is called by ADISU3 to compute the update right hand side terms in the energy equation of pipe flow with the insulating wall case, namely, solving (3-31), (3-37).

<u>Subroutine FLUXT (NN)</u>

Subroutine FLUXT (NN) is called to compute the dimensionless enhanced axial heat flux as well as the heat flux by pure molecular conduction either in the wall or the pipe fluid, namely, equations (2-34) to (2-37).

<u>Subroutine OUT (NTID)</u>

The subroutine OUT (NTID) is called to compute and output the dimensional heat flux, tidal displacement, and the average temperature (dimensionless).

<u>Subroutine ADICO3</u>

Subroutine ADICO3 is similar to ADISU3, but for the conducting wall case.

<u>Subroutine COTWAL</u>

This subroutine is called to calculate the coefficients in the wall conduction equation at each time step by using equation (3-42).

Subroutine RHSCOT (N,II,LINE)

Subroutine RHSCOT is similar to RHSINT, but for the conducting wall case.

Subroutine RHSWAL (N,II,LINE)

Subroutine RHSWAL (N,II,LINE) is called to compute the right-hand-side terms in the wall conduction equation with (3-32) and (3-38).

Subroutine ADISU1 (N)

Subroutine ADISU1 is similar to ADISU3, but for the case of Model 1.

Subroutine ADICO1 (N)

Subroutine ADICO1 is similar to ADISU1, but for the conducting wall.

REFERENCES

1. Abramowitz, M., and Stegun, I. A.(editors), "Handbook of Mathematics Functions with Formulas, Graphys, and Mathematical Tables", Dover Publications, Inc., New York (1972).

2. Ames, W. F., "Numerical Method For Partial Differential Equations," Academic Press, INC.

3. Anderson, D. A., Tannehill, J. C., and Pletcher, R. H., "Computational Fluid Mechanics and Heat Transfer," McGraw-Hill, New York (1984).

4. Aris, R., "The Dispersion of Solute in Pulsating Flow Through a Tube," Proceedings of Royal Society, London, A 259, pp.370-376 (1960).

5. Arpaci V., and Larsen P., "Convective Heat Transfer," Prentice Hall, Englewood Cliffs, NJ (1984).

6. Baldwin B. S., and Lomax, H., "Thin Layer Approximation and Algebraic Model for Separated Turbulent Flow," AIAA 16th Aerospace Sciences Meeting (Jan., 1978) pp.78-257

7. Bohn, D. J., Miyasaka, K., Marchak, B. E., Thompson, W. K., Froese, A. B., and Bryan, A. C., "Ventilation by High-Frequency Oscillation," Journal of Appl. Phys., Vol. 48, pp.710-716 (1980).

8. Bowden, K. F., "Horizontal Mixing in the Sea Due to Shearing Current," Journal of Fluid Mech., Vol. 21, p.84 (1965).

9. Chapman, A. J., "Heat Transfer," Macmillan Publishing Co., New York (1984).

10. Chatwin, P. C., "On the Longitudinal Dispersion of Passive Contaminant in Oscillatory Flow in Tubes". Journal of Fluid Mech., Vol. 71, part 3, pp.513-527 (1975).

11. Eckert, E. R. G., "Analysis of Heat and Mass Transfer," McGraw-Hill, New York (1972).

12. Jaeger, M. J., and Kurzweg, U. H., "Determination of the Longitudinal Dispersion Coefficient in Flows Subjected to High-Frequency Oscillations," Phys. Fluid, Vol. 26 No. 6, pp.1380-1382 (1983).

13. Joshi, C. H., Kamm, R. D., Drazen, J. M., and Slutsley, A. S., "An Experimental Study of Gas Exchange in Laminar Oscillating Flows," Journal of Fluid Mech., Vol. 133, pp.245-254 (1983).

14. Kaviany, M., "Some Aspects of Heat Diffusion in Fluids by Oscillation," International Journal Heat Mass Transfer, Vol. 29, pp.2002-2006 (1986).

15. Kurzweg, U. H., "Enhanced Heat Conduction in Fluids Subjected to Sinusoidal Oscillations," Journal of Heat Transfer, Vol. 107, pp.459-462 (1985).

16. Kurzweg, U. H., "Enhanced Heat Conduction in Oscillating Viscous Flows Within Parallel-Plate Channels," Journal of Fluid Mech., Vol. 156, pp.291-300 (1985).

17. Kurzweg, U. H., "Temporal and Spatial Distribution of Heat Flux in Oscillating Flow Subjected to an Axial Temperature Gradient," International Journal Heat Mass Transfer, Vol. 29, No. 12, pp.1969-1977 (1986).

18. Kurzweg, U. H., "Enhanced Diffusional Separation in Liquids by Sinusoidal Oscillations," to appear in Separation Sciences and Technology, in press.

19. Kurzweg, U. H., and Jaeger, M. J., "Diffusional Separation of Gases by Sinusoidal Oscillations," Phys. Fluids, Vol. 30, pp.1023-1026 (1987).

20. Kurzweg, U. H., and Jaeger, M. J., "Tuning Effect in Gas Dispersion under Oscillatory Conditions," Phys. Fluids Vol. 29, pp.1324-1326 (1986).

21. Kurzweg, U. H. and Lindgren, E. R. "Enhanced Heat Conduction By Oscillatory Motion of Fluids in Conduits," A Research Proposal to the Fluid Dynamics and Heat Transfer Program, The National Science Foundation, under Contract Number CBT-8611254 (1986).

22. Kurzweg, U. H., and Zhao, L. D., "Heat Transfer by High-Frequency Oscillations: A New Hydrodynamic Technique for Achieving Large Effective Thermal Conductivities," Phys. Fluids, Vol. 27, pp.2624-2627 (1984).

23. Li, C. P., "A Finite Difference Method for Solving Unsteady Viscous Flow Problems," AIAA Journal, Vol. 23, No.5 (1985).

24. MacCormack, R. W., "Current Status of Numerical Solutions of the Navier-Stokes Equations," AIAA 23rd Aerospace Sciences Meeting, Reno, Nevada, AIAA-85-0032 Jan. (1985)

25. Mastin, C. W., "Error Induced by Coordinate System," in J. F. Thomson (editor), Numerical Grid Generation, North-Holland, New York, pp.31-40 (1982).

26. Merkli, P., and Thomann, H., "Transition to Turbulence in Oscillating Pipe Flow," Journal of Fluid Mech., Vol. 68, pp.567-575 (1975).

27. Ommi, M., Iguchi, M., and Urahata, I., "Flow Patterns and Frictional Losses in An Oscillating Pipe Flow," Bulletin of the JSME, Vol. 25, No. 202. April (1982).

28. Pulliam, T. H., "Efficient Solution Methods for the Navier-Stokes Equations" Lecture Notes for the Von Karman Institute (Jan., 1986).

29. Schlichting, H., "Boundary Layer Theory" McGraw-Hill, New York (1972).

30. Shah, V. L., "COMMIX-1B: A Three-Dimensional Transient Single-Phase Computer Program for Thermal Hydraulic Analysis of Single and Multicomponent Systems," Vol. 1: Equations and Numerics, Available from Superintendent of Documents U. S. Government Printing Office, P. O. Box 37082, Washington, D.C.20013-7982, Sep., (1985).

31. Shih, T. M., "Numerical Heat Transfer," Hemisphere Publishing Corp., Washington (1984).

32. Taylor, F. R. S., "Dispersion of Soluble Matter in Solvent Flowing Slowly Through a Tube," Proc. Roy. Soc., pp.186-203 (1953).

33. Thompson, J. F., "Grid Generation Technique in Computational Fluid Dynamics", AIAA Journal, Vol. 22 Nov.11, pp.1506-1519, (1984).

34. Thompson, J. F., Thames, F. C. and Mastin, C. W., "Automatic Numerical Generation of Body-Fitted Curvilinear Coordinate System for Field Containing Any Number of Arbitrary Two-Dimensional Bodies," Journal of Computational Physics., Vol. 15, pp.299-319 (1974).
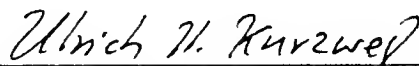
35. Thompson, J. F., Warsi, Z. U. A., and Mastin, C. W.,
    "Boundary-Fitted Coordinate Systems for Numerical
    Solution of Partial Differential Equations----A Review",
    Journal of Computational Physics., Vol 47., pp.1-108
    (1982).

36. Uchida, S., "The Pulsating Viscous Flow Superposed on
    the Steady Laminar Motion of Incompressible Fluid in a
    Circular Pipe," ZAMP, Vol. VII, pp.402-421 (1956).

37. Warming, R. F., and Beam, R. M., "On the Construction
    and Application of Implicit Factored Schemes for
    Conservation Laws," SIAM-AMS Proceedings, Vol 11,
    pp.85-129 (1978).

38. Watson, E. J., "Diffusion in the Oscillation Pipe Flow,"
    Journal of Fluid Mech., Vol. 133, pp.233-244 (1983).

BIOGRAPHICAL SKETCH

Guo-Jie Zhang was born on June 26, 1941, in Beijing, China, and spent his childhood and youth in that beautiful capital city. After graduating from Beijing 21th High School in 1960 he entered the University of Science and Technology of China, Beijing, China. After 5 years of college education in the Department of Mechanics, he graduated in July, 1965. Since then he, as an aircraft structure strength analysis engineer, has been engaged at the Aircraft Research and Development Institute, Nanchang Manufacturing Aircraft Company, China. until the spring of 1981. During that period he participated in the research on and development of several aircraft with his main contributions being in the area of the studies with finite element methods. In May, 1981, he was selected to study abroad by the Ministry of Aviation Industry of China and after one year's English language training at Nanjing Aeronautical Institute, he was sent to study in the Department of Aerospace Engineering, Mechanics, and Engineering Science, University of Florida as a visiting scholar, and later, in May, 1983, transferred to graduate student status. He received his Master of Engineering degree in April, 1986, and expects to receive the degree of

161

Doctor of Philosophy in the spring of 1988. He is married to Chun-hua Shi and has two children, Yan Zhang and Wei Zhang. Mr. Guo-jie Zhang is a member of the Aeronautics Society of China.
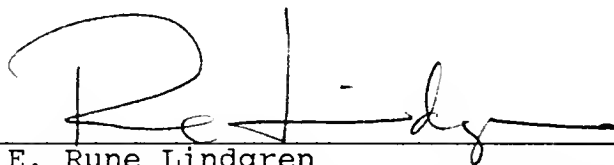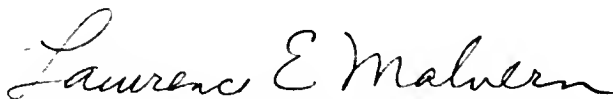
I certify that I have read this study and that in my opinion it conforms to acceptable standards of scholarly presentation and is fully adequate, in scope and quality, as a dissertation for the degree of Doctor of Philosophy.

Ulrich H. Kurzweg, Chairman
Professor of Aerospace Engineering,
Mechanics, and Engineering Science

I certify that I have read this study and that in my opinion it conforms to acceptable standards of scholarly presentation and is fully adequate, in scope and quality, as a dissertation for the degree of Doctor of Philosophy.
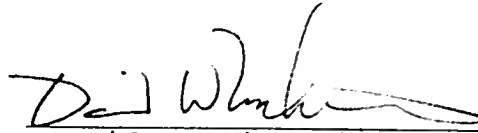
E. Rune Lindgren
Professor of Aerospace Engineering,
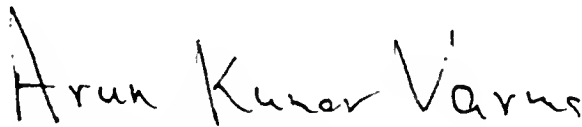Mechanics, and Engineering Science

I certify that I have read this study and that in my opinion it conforms to acceptable standards of scholarly presentation and is fully adequate, in scope and quality, as a dissertation for the degree of Doctor of Philosophy.

Lawrence E. Malvern
Professor of Aerospace Engineering,
Mechanics, and Engineering Science

I certify that I have read this study and that in my opinion it conforms to acceptable standards of scholarly presentation and is fully adequate, in scope and quality, as a dissertation for the degree of Doctor of Philosophy.

David W. Mikolaitis
Assistant Professor of Aerospace
Engineering, Mechanics, and
Engineering Science

I certify that I have read this study and that in my opinion it conforms to acceptable standards of scholarly presentation and is fully adequate, in scope and quality, as a dissertation for the degree of Doctor of Philosophy.
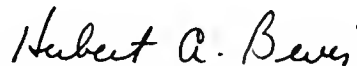
Arun K. Varma
Professor of Mathematics

This dissertation was submitted to the Graduate Faculty of the College of Engineering and to the Graduate School and was accepted as partial fulfillment of the requirements for the degree of Doctor of Philosophy.

April 1988

Dean, College of Engineering

Dean, Graduate School